Title
Effects of Wavelength-Shifting Plates on the Light Collection and Vertex Reconstruction in a Large-Volume Water-Cherenkov Detector

Author
Mullen, Austin

Publication Date
2022

Peer reviewed|Thesis/dissertation

Effects of Wavelength-Shifting Plates on the Light Collection and Vertex Reconstruction in a Large-Volume Water-Cherenkov Detector

By

Austin Mullen

A dissertation submitted in partial satisfaction of the

requirements for the degree of

Doctor of Philosophy

in

Engineering - Nuclear Engineering

in the

Graduate Division

of the

University of California, Berkeley

Committee in Charge:

Professor Jasmina Vujic, Chair
Professor Kai Vetter
Professor Michael Nacht
Dr. Adam Bernstein

Fall 2022

Abstract

Effects of Wavelength-Shifting Plates on the Light Collection and Vertex Reconstruction in a Large-Volume Water-Cherenkov Detector

by

Austin Mullen

Doctor of Philosophy in Engineering - Nuclear Engineering

University of California, Berkeley

Professor Jasmina Vujic, Chair

Antineutrino detectors may be able to fill an important role in the global nuclear nonproliferation regime by discovering an undeclared nuclear reactor or monitoring a known reactor tens of kilometers away. However, such detectors are large capital investments, and a substantial portion of their cost is the photomultiplier tubes that collect the light from antineutrino interactions in the detector volume and convert it into a usable electronic signal. As such, maximizing the light collection efficiency, and thus performance, of each photomultiplier tube is paramount. Wavelength-shifting plates may be able to aid in this goal. Wavelength-shifting plates increase the amount of light collected by each photomultiplier tube, which translates into a greater energy resolution of the detector. At the same time, however, the wavelength-shifting plates smear out the collection of this light in time, as light captured by the plates is delayed for different amounts of time before reaching a photomultiplier tube. This reduces the ability of post-processing algorithms to successfully reconstruct the location at which an event occurred in the detector. This is expected to have a countervailing effect to the improved energy resolution provided by the wavelength-shifting plates. This work explores the trade-off between these two effects, utilizing Monte Carlo simulations validated against experiments in air and in a water-Cherenkov detector to predict the effects that wavelength-shifting plates will have on large-volume water-Cherenkov detector performance. It was found that wavelength shifting plates improve the overall signal-to-background ratio of a 16 meter diameter, 16 meter height cylindrical detector by 13%, allowing a 3000 MWth undeclared nuclear reactor to be discovered 22% faster, in 16 days rather than 20.4 days when a detector without wavelength-shifting plates is utilized. This improvement is significant as it demonstrates that the improvement wavelength-shifting plates provide to light collection outweighs their effects on timing, so that wavelength-shifting plates may be a cost-effective way to improve the overall performance of large-volume water-Cherenkov antineutrino detectors intended for nuclear nonproliferation missions.

ACKNOWLEDGMENTS AND DISCLAIMERS

This work was performed under the auspices of the U.S. Department of Energy by Lawrence Livermore National Laboratory (LLNL). Lawrence Livermore National Laboratory is operated by Lawrence Livermore National Security, LLC, for the U.S. Department of Energy, National Nuclear Security Administration under Contract DE-AC52-07NA27344. This document has the release number LLNL-TH-842619. This material is based upon work supported by the Department of Energy National Nuclear Security Administration through the Nuclear Science and Security Consortium under Award Number(s) DE-NA0003996 and/or DE-NA0003180, and subaward number B653597. This report was prepared as an account of work sponsored by an agency of the United States Government. Neither the United States Government nor any agency thereof, nor any of their employees, makes any warranty, express or limited, or assumes any legal liability or responsibility for the accuracy, completeness, or usefulness of any information, apparatus, product, or process disclosed, or represents that its use would not infringe privately owned rights. Reference herein to any specific commercial product, process, or service by trade name, trademark, manufacturer, or otherwise does not necessarily constitute or imply its endorsement, recommendation, or favoring by the United States Government or any agency thereof. The views and opinions of authors expressed herein do not necessarily state or reflect those of the United States Government or any agency thereof.

Special thanks to the WATCHMAN Collaboration and Dr. Adam Bernstein (P.I.) for supporting this work, and Dr. Tomi Akindele, Dr. Marc Bergevin, and Dr. Steven Dazeley for their help and guidance with this project.

TABLE OF CONTENTS

LIST OF TABLES

LIST OF FIGURES

Chapter One
Introduction

1.1 Overview and Motivation

In 1953, then United States President Dwight D. Eisenhower laid out his plan to overcome the "fearful atomic dilemma:" the boon of atomic science and technology should be available for peaceful use by all states, while the bane of the military applications of atomic energy must be restricted [1]. President Eisenhower sought to achieve this balance through the establishment of an international monitoring agency, tasked with both ensuring equal access of all states to the peaceful benefits of nuclear energy, while preventing those same states from developing their own nuclear weapons. This international agency was codified as the International Atomic Energy Agency, or IAEA, and has diligently carried out both of its tasks to the present day. As the peaceful applications of nuclear technology have advanced and spread over time, there has been a constant quest to update and advance the technology safeguarding those uses.

One such technology that has the potential to be both a novel and valuable asset to the international nuclear non-proliferation regime is large-scale, long-baseline antineutrino detection. These detectors may aid international nuclear nonproliferation efforts by allowing for the discovery or monitoring of nuclear reactors from tens of kilometers away or more. Wavelength-shifting (WLS) plastic plates may be able to cost-effectively increase the performance of such detectors or to reduce the detector's overall cost. The wavelength-shifting plates increase the light collection of the detector's photomultiplier tubes, or PMTs, which convert light in the detector into electronic signals. This, in turn, increases the overall energy resolution of the detector and improves its performance or allows the detector to maintain its performance with fewer PMTs, and thus at a reduced cost. At the same time, however, the plates make it more difficult to accurately reconstruct where events occur in the detector volume. Algorithms use the timing profile of light arriving at the PMTs to reconstruct this position, and light that is captured by the plate is delayed by a factor of 2-5 compared to light that strikes the PMT directly. This degradation in position reconstruction can make it more difficult to discriminate signal events in the detector from backgrounds, and thus serves as a countervailing force to the improved performance

from the increased energy resolution of the detector. This work seeks to evaluate this trade-off and determine the overall benefit to detector signal-to-background and other relevant measures that wavelength-shifting plates may provide to a large-scale water-Cherenkov antineutrino detector.

This chapter will proceed in two parts. The first will give an overview of the antineutrino, its behavior, and the techniques used to detect it, including descriptions of some of the subsystems of a detector relevant for the performance of a wavelength-shifting plate. Then, the discussion will return to the potential applications antineutrino detectors may have in the nuclear non-proliferation regime and how wavelength-shifting plates may assist in those use-cases.

1.2 The Ghost Particle: The Behavior of an Antineutrino

The antineutrino was first theorized in 1930 by theoretical physicist Wolfgang Pauli, who proposed it as a solution to the puzzling behavior of nuclear beta decay [2]. As understood at the time, an unstable nucleus would decay by the emission of a single electron to reach a more stable isotope. This reaction indicates that, by conservation of momentum, the electron should always be emitted at a single, discrete energy. Observations, however, ran contrary to this fact, showing that the electron was emitted along a distribution of energies. Pauli proposed that momentum could be conserved if a second, uncharged and nearly undetectable particle was also emitted in the decay, which he dubbed the "neutron." Pauli's "neutron" was later renamed by Enrico Fermi to the "neutrino," or "little neutral one," after James Chadwick named his own, experimentally proven neutral particle the "neutron."

The elusive neutrino, by its uncharged, nearly undetectable nature, evaded experimental detection until 1953 when Fredrick Reines and Clyde Cowan made the first discovery of an antineutrino, a neutrino's very similar antimatter counterpart, in Project Poltergeist [3]. The detector used a cadmium-loaded liquid scintillator solution to detect the antineutrinos emitted from an operating nuclear reactor at Hanford, Washington. Their discovery was confirmed three years later in another experiment performed again by Reines and Cowan using a similar detector at the Savannah River Plant [4].

Antineutrino detection has since developed, primarily in the realm of basic science and physics, as scientists have probed the behavior of antineutrinos to explore the edges of the standard model and the mysteries of the Weak Fundamental Force. Since its discovery, interest has also grown in utilizing the technology to monitor nuclear reactors. One of the first practical detectors deployed that demonstrated this potential was SONGS1, which was deployed at the San Onofre Nuclear Generating Station in California, with results first published in 2007 [5]. The technology has continued to mature as different detector experiments have demonstrated different capabilities.

The CHOOZ detector, which was deployed in France, allowed for the initial direction of travel of the antineutrino to be reconstructed [6]. The KanLAND experiment demonstrated the ability to successfully detect antineutrinos from nuclear reactors at a long average baseline (at approximately 180 kilometer-scale power-weighted average standoff) [7]. Looking forward, the technology will continue to develop. The WATCHMAN Collaboration has proposed a demonstration of reactor monitoring at 10s of kilometers distance using a large-volume antineutrino detector [8]. Additionally, the SANDD detector seeks to demonstrate the ability of plastic scintillators to monitor detectors at short-range with minimal shielding, increasing the flexibility with which such detectors can be deployed [9]. This further allows for the development of mobile antineutrino detectors, such as the PANDA and NuLat detectors, with much more flexible deployment possibilities, which are currently under development by several groups [10, 11].

1.2.1 Neutrino Mass and Flavor Eigenstates

Several properties of the antineutrino are germane to their detection. First, there are three different types of neutrinos and antineutrinos, one to match with each of the leptons, called their "flavor eigenstates": electron antineutrinos, muon antineutrinos, and tau antineutrinos [12]. Each flavor eigenstate of an antineutrino has a preferred mass eigenstate, simply labeled as mass eigenstate one, two, and three. The electron antineutrino most closely demonstrates mass eigenstate one, while the muon antineutrino demonstrates mass eigenstate two, and the tau antineutrino three. This is, however, a simplification as each flavor state is a superposition of the three mass states, though a complete discussion of this behavior is beyond the scope of this work. Throughout this work, all particles referred to as antineutrinos are electron antineutrinos, as those are the only flavor state of the three that are emitted from fission reactions and the only one detectable by the antineutrino detectors presented here. This fact will be important for the discussion of neutrino oscillations at the end of this section.

1.2.2 Neutrino Emissions from Nuclear Reactors

One neutrino is emitted per nuclear beta decay (neglecting the possibility of neutrinoless double beta decays for the sake of this discussion). In the case of a beta minus decay, an antineutrino is emitted to preserve lepton number, while in the case of a beta plus decay, a neutrino is emitted. This (anti)neutrino is emitted along a spectrum of energies in order to satisfy the conservation of momentum with the emitted electron or positron and the recoiling daughter nucleus. The energy spectrum itself, neglecting the kinetic energy of the recoiling daughter nucleus, is a complement to the emitted electron's energy spectrum, as seen in Figure 1.1. This makes the expected neutrino energy spectrum a known quantity given knowledge of the beta

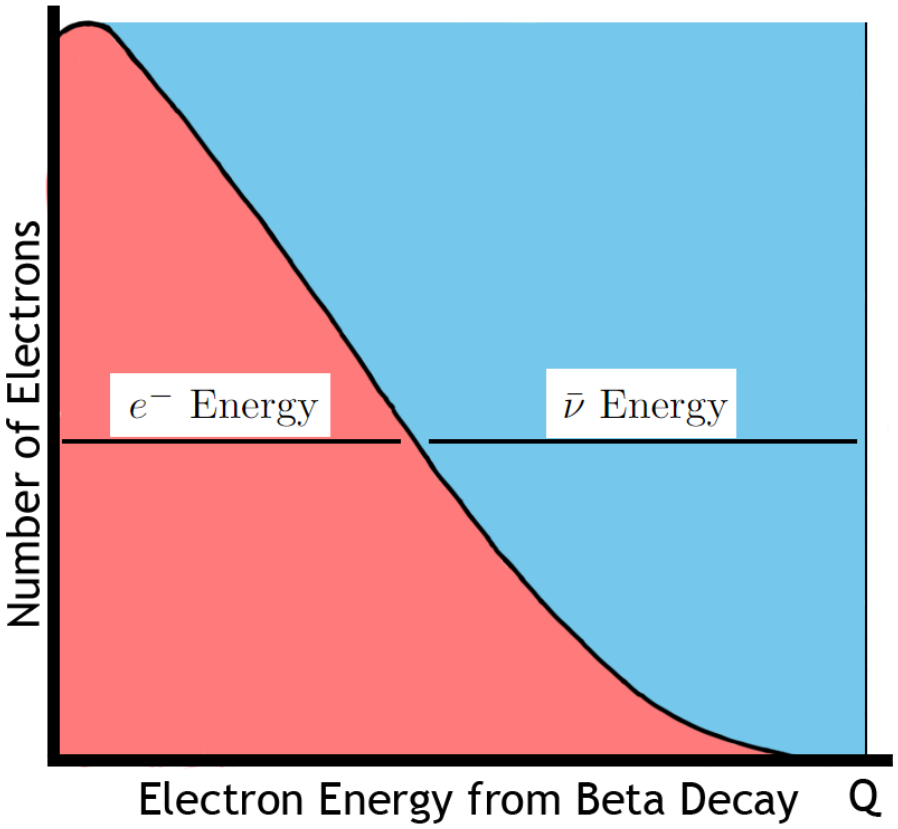

Figure 1.1 The electron/antineutrino energy spectrum for an arbitrary beta decay. The energy of the emitted antineutrino (in blue) is the Q value of the decay, minus the energy of the emitted electron (in red).

decay's energy spectrum.

As one antineutrino is emitted per nuclear beta minus decay, it is a corollary that multiple antineutrinos will be emitted by every fission event, as the fissioning of uranium, plutonium, or any isotope of interest will almost invariably result in a number of beta minus decays as the neutron-rich fission fragments rapidly try to reach more stable states [13]. In practice, each fission results in approximately six antineutrinos being emitted, though the exact amount will vary from fission to fission. It is clearly shown, therefore, that an operating nuclear reactor emits an enormous quantity of antineutrinos at any given time. Take a fifty-megawatt thermal nuclear reactor, for example, with $1.56 * 10^{18}$ fissions per second. This reactor core thus produces, at six antineutrinos per fission, $9.36 * 10^{18}$ antineutrinos per second, emitted in all directions from the reactor core.

1.2.3 Neutrino Interactions with Matter

These antineutrinos, however, would not be seen by a detector if they were rapidly absorbed by the shielding surrounding the reactor. Fortunately (for this issue, at least), antineutrinos are very non-interactive. As uncharged leptons, they are unaffected by both the Strong and the Electromagnetic Fundamental Forces, leaving the Weak Force as an antineutrino's only way to interact with its surroundings, as gravity will not sufficiently affect an antineutrino in any case considered here. The Weak Force is eponymously weak, leading to extremely low antineutrino interaction cross sections and extremely long mean free paths in almost all media. As an example, the cross section for an antineutrino interacting with a free proton through an inverse beta decay reaction is on order 10^{-20} barns [14]. This translates to a lightyear-scale mean free path of interaction of an antineutrino through water. While there are additional methods other than inverse beta decay for an antineutrino to interact by and be removed from a flux, this calculation illustrates that no practical amount of shielding will be consequential in reducing the overall antineutrino flux from a nuclear reactor core.

We can now turn our discussion to the method of interaction referenced so far: an inverse beta decay, or IBD reaction. This interaction is mediated by the Weak Force and proceeds according to the Feynman diagram depicted in Figure 1.2. To begin the interaction, an antineutrino impinges on a free proton (for our purposes, any hydrogen atom is considered a "free proton" as the energy of chemical bonds is negligible on the energy scale considered here). The antineutrino and the proton then exchange a W^- boson, whereby the antineutrino is transformed into a positron and one of the up quarks in the proton is flipped into a down quark, converting the proton into a neutron [15]. This reaction has an energy threshold of 1.8 MeV, and due to the large mass difference between the neutron and the positron, the energy of the outgoing positron is approximately $T_{e^+} = T_{\bar{\nu}} - 1.8MeV$.

In a water-Cherenkov detector, which will be discussed in more detail in a subsequent section, both the positron and the neutron from the IBD reaction produce light and contribute to the antineutrino signal. The positron will immediately produce Cherenkov light in the water as it is created at a velocity greater than the speed of light in the medium. The neutron will, after a short delay, be captured on hydrogen or a neutron capture agent (such as the Cadmium used in the original Project Poltergeist experiment), which will de-excite by the emission of gamma rays, which produce Compton electrons in water, which in-turn produce Cherenkov light. This characteristic double signal from IBD reactions has made it one of the most reliable for detecting antineutrinos.

1.2.4 Neutrino Oscillations

A final behavior of antineutrinos that will be discussed in this section is the principle of antineutrino oscillation. This is one of the most active areas of study for

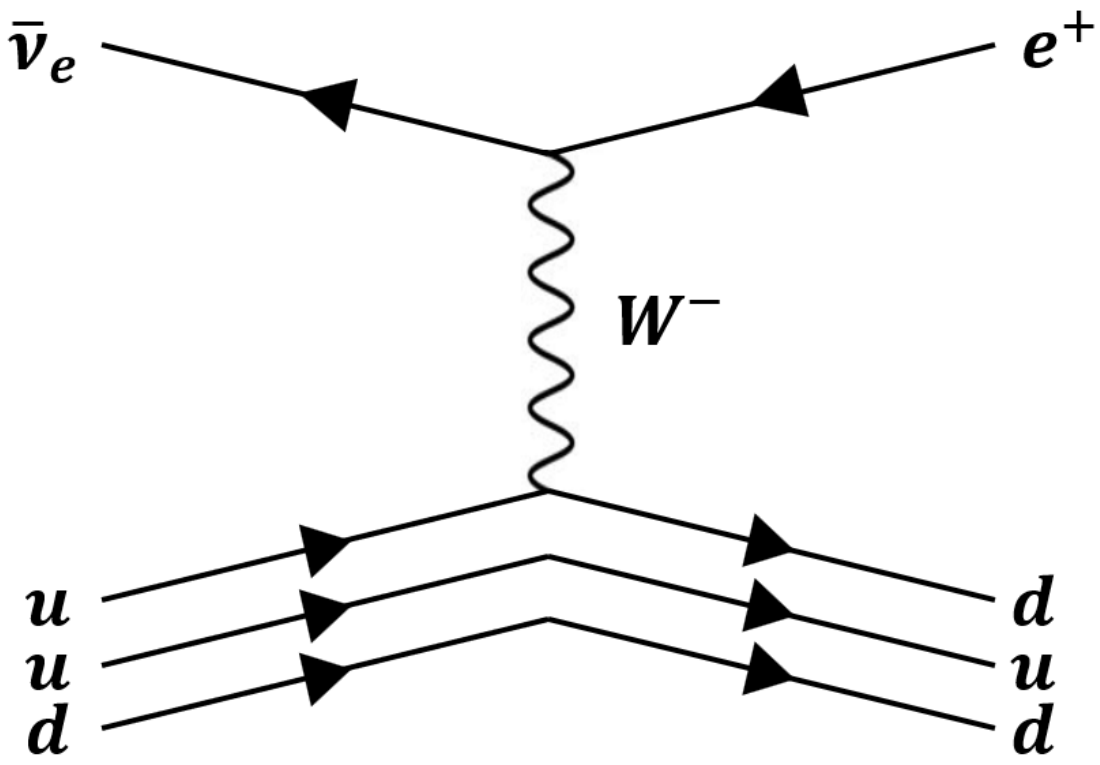

Figure 1.2 A Feynman diagram of an inverse beta decay reaction, moderated by a W^- boson, by which an antineutrino is converted into a positron and a proton (uud) is converted into a neutron (dud).

modern neutrino physics, with a number of experiments proposed, designed, and carried out to probe the neutrino's behavior at both near and far baseline and determine the mass hierarchy and mixing angles that drive this oscillation [16–21]. To discuss the phenomenon of antineutrino oscillation, consider a beam that originally consists entirely of electron antineutrinos. As that beam travels through space, some of the electron antineutrinos will spontaneously transform, or oscillate, into the other flavor states, primarily into muon antineutrinos. Those muon antineutrinos will in turn oscillate back to electron antineutrinos (or further into tau antineutrinos) as the beam propagates. This oscillation behavior has both a short and a long component, as seen in Figure 1.3, where the short component is relevant only over short (meter-to-kilometer-scale) baselines and the long component is only relevant over long (tens-of-kilometer-scale) baselines. This behavior must be accounted for when calculating the antineutrino flux at a detector location, as only electron antineutrinos will interact in the detector volume in a way that can be seen and recorded. The behavior of the oscillations depend on both the mixing angle between the electron, muon, and tau flavors of the neutrino and the mass differences between mass eigenstates 1, 2, and 3, though a more complete description of this phenomenon is beyond the scope of this work and available elsewhere [22].

This neutrino oscillation behavior is important to consider when developing large-scale antineutrino detectors for nuclear non-proliferation purposes. As can be seen from Figure 1.3, the survival probability of electron antineutrinos at 60 km is only around 30%. In practice, this means that detectors placed 60 km from a nuclear reactor core will see a greatly reduced signal rate from what would be expected if neutrino oscillation was not considered. In order to maximize the signal rate, one must account for the neutrino oscillation survival probability at different stand-off distances.

1.3 Techniques for Detecting Antineutrinos

Antineutrino detectors, in order to detect the antineutrinos from a distant nuclear reactor core, must be made very large to maximize their interaction rate. Such a large detector, on order of kilotons of detector media, must generally utilize a water-based detector fill, as traditional scintillator has too short of an attenuation length to be viable at such sizes [24]. Pure water, often doped with a neutron capture agent, is currently the most commonly utilized fill for large-scale detector experiments, but antineutrino interactions in water produce very little light and thus can be difficult to positively identify and gather information from. One approach to overcome this limitation is the development of water-based liquid scintillator, which seeks to combine the favorable attenuation lengths of water with the higher light output of liquid scintillator [25]. Another approach is to increase the collection of the limited light at the photodetectors themselves, and it is this area that wavelength-shifting plates may be useful. This approach has been considered for other large-volume detectors,

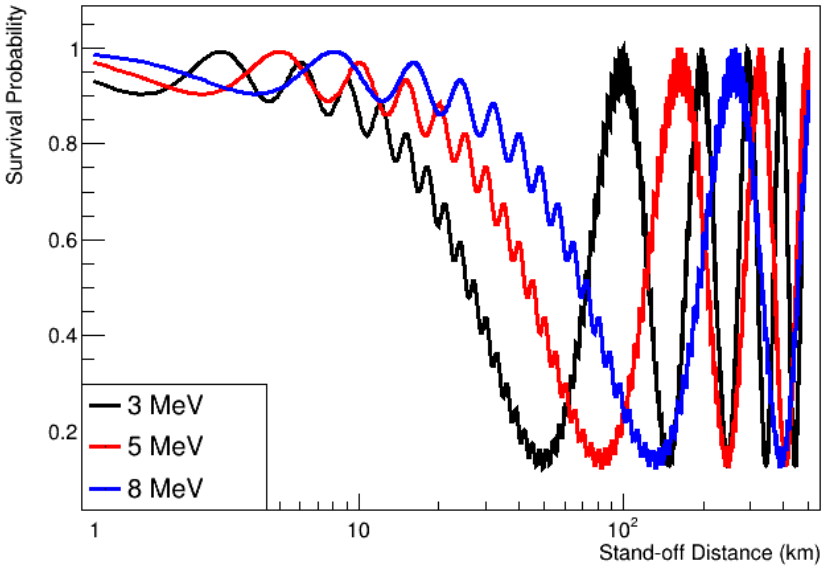

(a) Survival Probability for Discrete Energies

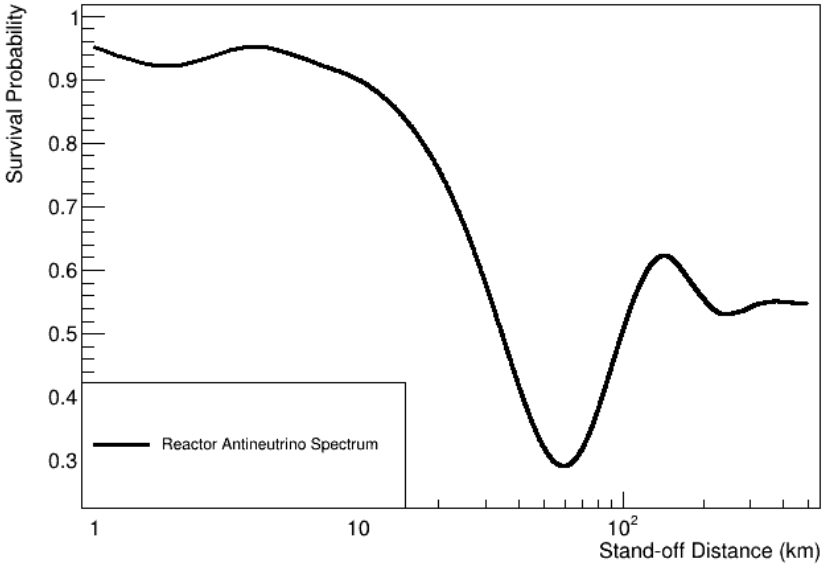

(b) Survival Probability for Reactor Antineutrinos

Figure 1.3 The probability of electron neutrinos of (a.) various discrete energies and (b.) reactor antineutrino energy spectrum surviving as they propagate. The survival probability of electron neutrinos at different baselines is important to consider when determining the location of an antineutrino detector. Figure generated using a modified WATCHMAKERS analysis code [23].

such as the Long Baseline Neutrino Experiment Far Detector and has been actually implemented in the IMB-3 detector [26, 27]. For the IMB-3 detector, it was found that coupling 5 inch photomultiplier tubes to 24 inch square wavelength-shifting plates doubled their light collection [28]. The effects of wavelength-shifting plates on the performance, energy resolution, and position reconstruction capabilities of a large-scale detector utilizing large surface area PMTs, however, merit additional study.

In water, IBD reactions create light through the Cherenkov effect, where a particle traveling faster than the local speed of light in a medium emits ultraviolet to visible blue light. This process, however, creates very few photons, making a water Cherenkov detector a light-starved environment. Wavelength-shifting plates can can more efficiently utilize all of the light produced by capturing and redirecting photons that would have otherwise missed the detector's photomultiplier tubes, or PMTs, which convert photons into a readable electronic signal. Therefore, wavelength-shifting plates may be able to increase the overall efficiency of an existing large-scale water Cherenkov detector using the same number of PMTs.

In both water and scintillator based detectors, the general process for detecting and identifying an antineutrino interaction remains the same and has remained largely unchanged since the first discovery of the neutrino [3]. First, an antineutrino interacts with a free proton in the detector volume through an inverse beta decay, as previously described. An alternate interaction mechanism, elastic scattering between the antineutrino and an electron in the detector, is also possible, though this interaction produces a single, low-energy event and is not used for antineutrino detection in a water-Cherenkov detector [29]. The IBD reaction produces both a positron and a neutron. The positron immediately deposits energy in the detector, producing light either through the Cherenkov effect, for a water-based detector, or scintillation, in a scintillator-based detector. The process of both these light production mechanisms will be described subsequently.

While the positron immediately begins to produce light in the detector volume, the neutron first must be captured. In many detectors, the fill volume is doped with a neutrino capture agent such as gadolinium (or in the case of the original Project Poltergeist, cadmium) in order to maximize the energy released from a neutron capture. A neutron is generally captured by such an agent, if it is present, after a delay of approximately 30 microseconds, and on hydrogen, if a capture agent is not present, after approximately 200 microseconds [30]. The nucleus that captured the neutron will then de-excite through the emission of gamma rays. In the case of gadolinium, this takes the form of a gamma cascade totalling around 8 MeV worth of energy, while for hydrogen, it only totals 2.2 MeV of energy. These gamma rays then have Compton scattering interactions with the electrons in the detector, thereby transferring some of their energy to the charged electrons, which in turn produce Cherenkov or scintillation light in the detector volume. A single antineutrino interaction therefore produces a two-stage event: first, the light produced by the positron, and second, after a delay of tens of microseconds, the light produced by the neutron. This double-event is useful

for discriminating against various sources of background, which will generally only produce a single flash of light in the detector, though some sources of background are able to recreate or mimic these coincidence events.

1.3.1 Sources of Background for Antineutrino Detectors

As will be discussed later in this chapter, the goal of a large-scale antineutrino detector is to monitor or discover a single nuclear facility. There are three primary sources of background when performing such a measurement that will be considered here: geoneutrinos, antineutrinos from the global nuclear reactors, and accidental backgrounds. Each will be described briefly in turn, before subdominant backgrounds not considered in this work are discussed.

The earth's crust naturally contains three long-lived radioactive decay chains that produce beta emitters: uranium-235, uranium-238, and thorium-232. Each of these atoms heads a decay chain along which lie several beta emitters. These beta emitters, primarily in the decay chains of uranium-238 and thorium-232, create antineutrinos which, due to their long mean-free path, escape from the earth's crust and can potentially interact in an antineutrino detector. These geoneutrinos are difficult to distinguish from the signal events of interest in most cases, but a few factors exist that can differentiate them in sufficiently sensitive detectors. First, geoneutrinos will be produced at a generally lower energy than reactor-origin antineutrinos, meaning that a detector with a good energy resolution (likely a liquid scintillator detector) may be able to distinguish some geoneutrinos from the antineutrinos of interest. Second, because antineutrino detectors have, in the grand scale of the earth, relatively little of the earth's crust above them, geoneutrinos will generally arrive at the detector from below. A detector that can reconstruct the arrival direction of antineutrinos may be able to use this fact to discriminate against many geoneutrinos.

At the time of this writing, there are 437 operating nuclear power reactors worldwide, in addition to a number of research reactors [31]. While an antineutrino detector for non-proliferation purposes is only interested in one of them, or possibly an undeclared reactor, the rest will continue to produce antineutrinos in large quantities. Because the antineutrino flux from each reactor will fall off with the distance from the reactor squared, those reactors closest to the detector will be the largest contributors to this background. In places with large concentrations of nuclear reactors, such as Europe, this can be expected to be a large source of background events in the detector, while in places with fewer nuclear reactors, like South America, it can be expected to be a less significant source. Because the antineutrinos from the global set of reactors have largely the same energies as those emitted from the nuclear reactor of interest, the only way to potentially discriminate against this background is by reconstructing the incoming direction of antineutrinos that interact in the detector – events that do not originate from the direction of the nuclear reactor of interest can be discarded. Otherwise, this is a largely irreducible background identical to the signal events.

The components of an antineutrino detector are selected for their radiopurity – that is, having low levels of radioactive contaminants. Despite this, all components of a detector system will still have radioactive impurities. Notably, the PMTs and their support structures both contain radioactive impurities and are very close to the active detector volume. Because of this, beta and gamma rays will nearly constantly interact in the detector volume, producing light and potentially being mis-reconstructed as true antineutrino events. Several cuts on the data are made to reduce this background. First, as described, antineutrino events will always occur in a correlated pair, with positron creating light immediately followed by the neutron. Beta and gamma interactions, on the other hand, will generally only produce a single flash of light. In order to be mistaken for an antineutrino event, two beta/gamma interactions must occur in the detector in coincidence in both time and space, thus creating an "accidental" coincidence event. If the time and space coincidence requirements are sufficiently tight, this is a relatively unlikely occurrence, meaning that this cut is effective at excluding a vast majority of this source background events. For events that survive this cut, two further cuts are made. First, positrons and neutrons, in general, deposit more energy into the detector than beta and gamma interactions, so an energy cut is applied. Second, because beta and gamma events generally originate from the edges of the detector, near the PMTs and their support structures, a fiducial cut is applied, whereby only events that are reconstructed to the center volume of the detector are accepted as potential signal events. With coincidence, energy, and spatial cuts, this source of background can be greatly reduced but never eliminated, meaning that the use of radiopure detector components is vital to detector performance.

Finally, there are several subdominant sources of background that will not be considered in the analysis here. First, muons that pass through or nearby the detector may produce radionuclides or fast neutrons that can create background events in the detector. To try to prevent this, the active detector volume is surrounded by an active veto region, usually a water-Cherenkov detector. The purpose of this region is to detect when a muon passes through or immediately nearby the detector and "veto," or toss out, any events that occur in the detector immediately after the muon passes through as backgrounds. The efficiency of this veto detector at detecting muons is very high, so this veto technique is effective at removing many potential background events. Some of the radionuclides that are produced by the muons, however, such as carbon-16, have sufficiently long half-lives to survive the veto time (which is only a couple of microseconds to minimize detector dead time) before decaying through beta-delayed neutron emission. When these isotopes decay, they produce both a neutron and a beta particle, mimicking the products of an inverse beta decay reaction. As such, these decays can produce false coincident events difficult to distinguish from true signal events. Muons that miss the detector but pass through the rock surrounding it may also produce fast neutrons. These neutrons, because they are uncharged and have high energy, can potentially pass through the detector's active veto region without interacting and reach the inner detector. These fast neutrons can

then elastically recoil off of a hydrogen atom in the detector, producing an immediate flash of Cherenkov light, before thermalizing and being captured, producing a second flash of light. As such, these fast neutrons also produce events similar in appearance to inverse beta decay reactions and, because neither they nor the muons that created them interact in the detector's veto region, can create background events in the detector. Both muogenic fast neutrons and radionuclides, however, are expected to be subdominant to the other sources of background described above, and are thus not treated in this analysis. Additionally, as this work compares the relative performance of a detector with and without wavelength-shifting plates, the presence or exclusion of these additional sources of background in the analysis is not expected to significantly affect the conclusions drawn.

1.3.2 Light Production through the Cherenkov Effect

The Cherenkov effect is most commonly known as the phenomenon that produces the characteristic blue glow around high-energy beta emitters, for example in a spent nuclear fuel pool or a pool nuclear reactor. It occurs any time that a particle travels faster than the local speed of light in a medium (while the true speed of light, c is an immutable constant, the speed of light as it travels through any medium with index of refraction n is affected according to the relationship $v_c = c/n$).

Take an arbitrary particle traveling with a velocity of v_p in a medium with an index of refraction of n, where $v_p > c/n$. In an arbitrary amount of time t, the particle will travel a distance of $x_p = v_p t$. An emitted electromagnetic wave, however, is constrained to only travel $x_c = v_c t = (c/n)t$ in that same time period. Because the electromagnetic wave cannot travel the same distance in the same amount of time, it is instead emitted at an angle, as seen in Figure 1.4. The value of this angle is determined by $\cos(\theta) = \frac{ct/n}{v_p t} = \frac{1}{(v_p/c)n}$, which can be simplified by defining $\beta = v_p/c$ to:

$$\cos(\theta) = \frac{1}{\beta n} \tag{1.1}$$

As can be seen from Equation 1.1, Cherenkov light is always emitted (from a particle of constant energy and thus velocity) at a single angle. In practice, this means that the photons are emitted in a cone leading the particle. For a sufficiently large detector, this cone of light is projected against the detector wall as a ring, a useful spectral feature used in some analyses to discriminate Cherenkov light from other sources and to better characterize the event that took place [32].

The frequency distribution of the photons emitted in the Cherenkov effect is given by the Frank-Tamm formula:

$$\frac{d^2E}{dxd\omega} = \frac{q^2}{4\pi}\mu(\omega)\omega\left(1 - \frac{c^2}{v_p^2 n^2(\omega)}\right) \tag{1.2}$$

which is a double differential of the total energy deposited by the Cherenkov effect in distance traveled and wavelength [33]. In the formula, q is the charge of the traveling

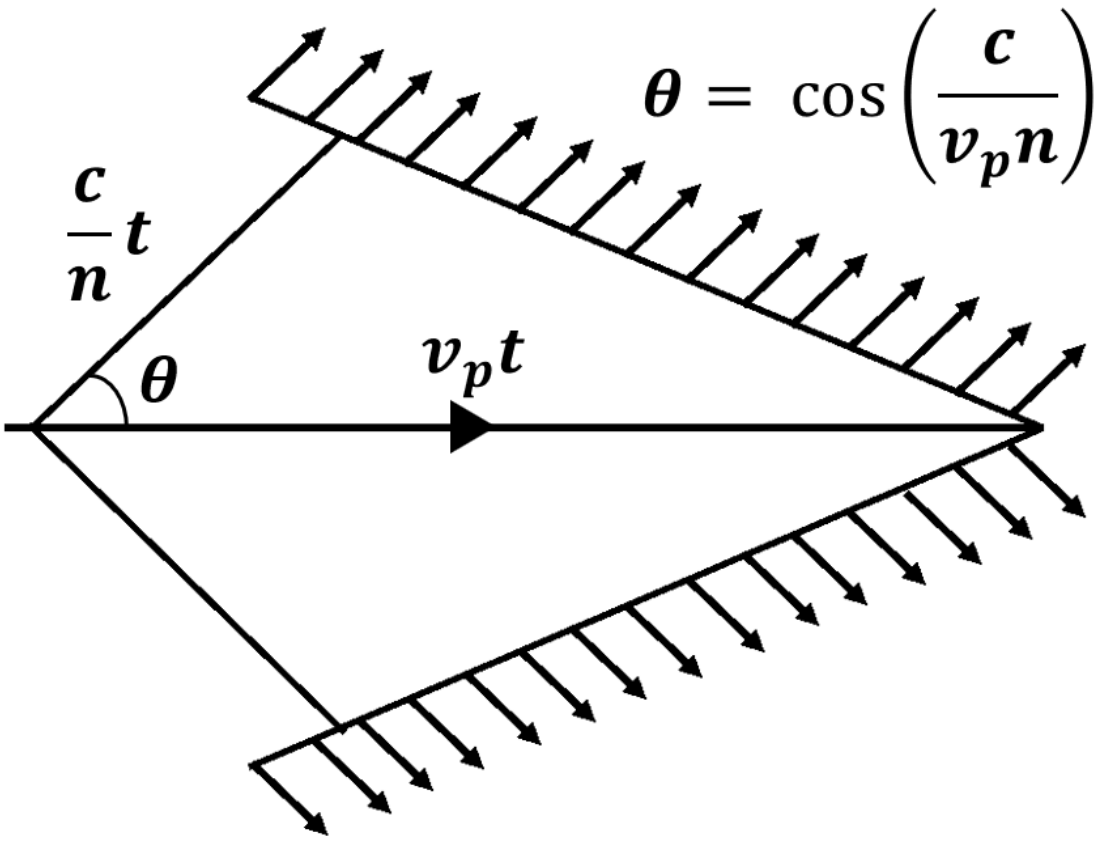

Figure 1.4 A graphical representation of the Cherenkov effect. A particle is travelling right at a velocity of v_p causing radiation to be emitted at an angle of θ.

particle, ω is its frequency, and μ and n are the permeability and index of refraction of the media, respectively, both dependent on the frequency of the photon. Cherenkov light has no spectral peaks; instead, it is a continuous distribution favoring shorter wavelengths and thus higher energy photons. This means that most of the Cherenkov photons created in a water-Cherenkov detector are in the ultraviolet or visible blue spectrum.

A final feature of the Cherenkov effect that can be seen from the formula is that very few photons are actually produced per energy deposited. Let us take an example interaction to demonstrate. Consider a 2 MeV electron travelling through water, with an index of refraction of 1.333 and a permeability of $1.256627 * 10^{-6}\ H/m$. Plugging values into the Equation 1.2:

$$\frac{d^2E}{dxd\omega} = \frac{(1.602 * 10^{-19}C)^2}{4\pi}(1.256627 * 10^{-6}H/m)\omega\left(1 - \frac{1}{(0.959)^2(1.33)^2}\right)$$
$$\frac{d^2E}{dxd\omega} = 2.5664591 * 10^{-45}J * s^2/m\omega(0.3853)$$
$$\frac{d^2E}{dxd\omega} = 6.172 * 10^{-27}\ eV * s^2/m\omega$$

Performing an integration over a range of wavelengths:

$$\frac{dE}{dx} = 6.172 * 10^{-27}\ eV * s^2/m \int_{10^{14}Hz}^{10^{16}Hz} \omega d\omega$$
$$\frac{dE}{dx} = 6.172 * 10^{-27}\ eV * s^2/m * 0.5\omega^2\Big|_{10^{14}Hz}^{10^{16}Hz}$$
$$\frac{dE}{dx} = 3.086 * 10^5\ eV/m$$

Considering the electron as it travels for one millimeter:

$$E = 0.001m * 3.086 * 10^5\ eV/m$$
$$E = 308.6\ eV$$

This can then be converted into a number of photons (assuming that 1 photon has an energy of approximately 4.13 eV, the average energy for a photon in the range we previously integrated over):

$$E = 308.6\ eV/(4.13\ eV/photon)$$
$$E = 74.72\ \text{ photons}$$

Over that range, the positron will lose approximately 0.185 MeV, according to the ESTAR database, meaning that the Cherenkov effect will produce on order 400 photons per MeV deposited in the detector [34]. This exercise, while simplified and approximated in several areas, does provide a good demonstration of the light-starved environment created when using Cherenkov light as the basis for detection, particularly

when compared to using scintillation, which can produce on order 10,000 photons per MeV deposited, as seen in the subsequent section.

1.3.3 Light Production through Scintillation

Organic scintillators, due to their relatively low cost and versatility, are ubiquitous among many radiation detection applications, including antineutrino detectors. While constructing a large-scale detector using kilotons of liquid scintillator solution is infeasible, many smaller-scale detectors use organic liquid or even plastic scintillators to detect antineutrinos, as previously discussed.

The production of scintillation light has no substantial threshold for occurring, and the light is emitted isotropically instead of in the characteristic cone discussed previously for Cherenkov light. Additionally, the number of photons produced from scintillation is much greater than that of Cherenkov light. Considering again the example 2 MeV electron investigated in the Cherenkov section, instead of producing on order several hundred photons via the Cherenkov effect as it traveled, it would produce on order 20,000 photons if it deposits all of its energy in a liquid scintillator medium, using a standard example of Eljen Technology EJ200 [35].

The mechanics of scintillation in an organic medium is as follows. First, a passing charged particle transfers some of its energy to a nearby organic molecule, or fluor. The fluor is excited up from its resting ground state to one of many excited states, also known as singlet states, as shown in Figure 1.5. From there, the fluor de-excites back down to its first excited state through non-radiative processes, or processes that do not result in the creation of a scintillation photon (in practice this is generally through vibration and heat). Once it occupies the first singlet state, the fluor has three paths for de-excitation. First, it can de-excite back down to one of its low-lying singlet states (those states just above the ground state in Figure 1.5) with the emission of a fluorescent photon. This process takes on the order of a couple nanoseconds. Second, it could instead convert itself from a singlet state to a triplet state before de-exciting through the emission of a phosphorescent photon. This process takes much longer: tens or even hundreds of nanoseconds. The difference in decay times between fluorescence and phosphorescence is the basis for the pulse shape discrimination of electrons and protons in organic scintillators, as more massive particles like the proton preferentially create long-lived triplet states. Third, the fluor can decay through non-radiative means through a process collectively called "quenching". Quenching prevents all of the energy absorbed by the scintillator from cleanly being converted into light [36].

It would be desirable to fill a large-scale antineutrino detector with liquid scintillator due to its much higher light output than the Cherenkov effect in water. This, however, is infeasible as liquid scintillator has relatively short attenuation lengths compared to water, meaning that light produced in the center of the detector would be re-absorbed before reaching the PMTs on the outside of the detector. Because of

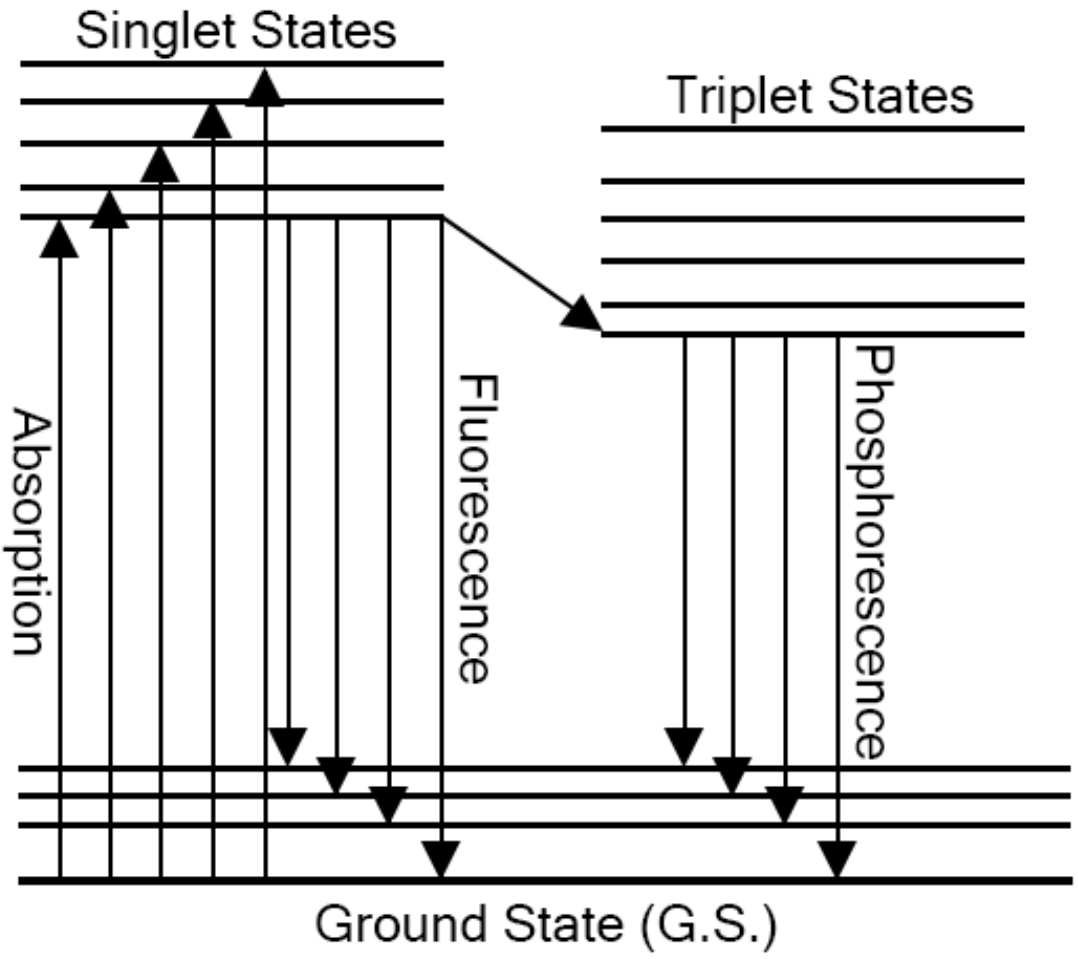

Figure 1.5 A representation of the energy levels that enable organic scintillation. Energy deposited in the organic medium can excite molecules to elevated singlet states, which may rapidly fluoresce as they de-excite to the ground state or may be converted into triplet states, which produce phosphorescent light after a longer delay.

this, water is used as the fill medium despite its reduced light output. It is beneficial, then, to better utilize the limited light produced by the Cherenkov effect in the detector; wavelength-shifting plates are one technology that seeks to improve this light collection.

1.4 Basis for Wavelength-Shifting Plate Behavior

The principles by which wavelength-shifting plates function are remarkably similar to those of an organic scintillator. In fact, wavelength-shifting plastics often have similar compositions to some plastic scintillator compounds, with additional ingredients added to suppress any scintillation light. In a wavelength-shifting plastic, an incoming photon is absorbed in the organic fluor molecule, exciting it up to one of its excited states. The fluor then de-excites down to its first excited state, again through non-radiative processes, before de-exciting the rest of the way back down to one of its low-lying singlet states through the emission of a fluorescent photon. This process generally takes on the order of a nanosecond, which is often referred to as a plastic's "decay constant" [36].

The wavelengths of absorption and emission in a wavelength-shifting plastic vary depending on the type of plastic and fluor used, but always express a Stokes shift: the absorption spectrum is always at a shorter wavelength than the emission spectrum, and there is generally not a significant overlap between the two spectra [37]. The principle of the stokes shift can be expressed in two ways. First, and most simply, it can be considered an application of conservation of energy. By conservation of energy, it is impossible for the fluor to emit more energy than it absorbs, so it naturally follows that the emitted photon will always have a lower energy than the absorbed photon and the stokes shift should be evident. A more nuanced look returns to Figure 1.5, where one can see that for much of the absorption spectrum, the fluor is not excited directly to its first excited state, but instead occupies one of the many states above the first excited state. The non-radiative de-excitation from this state down to the first excited state is thus energy "lost," contributing to the shift. When the fluor decays back down to ground state, a de-excitation to the first ground state can be relatively unlikely. Oftentimes, it will decay to one of the other, slightly more energetic "ground states", and the non-radiative de-excitation from this state to the true ground state furthers this Stokes shift. Taking losses from both the excitation and de-excitation into account, it becomes evident why there should be little overlap between the wavelength-shifting plate's absorption and emission spectra.

This process of absorbing and re-emiting photons is not perfectly efficient. Sometimes, after absorbing a photon, a fluor will de-excite through non-radiative means, similar to quenching in an organic scintillator. The efficiency of converting an absorbed photon into an emitted photon is called the quantum efficiency of the wavelength-shifting plastic. This efficiency can be quite high, around 90%, but will never be perfect, so some absorbed light will always be lost.

An advantage of a wavelength-shifting plastic is that the emitted light effectively "forgets" the trajectory of the absorbed photon and is emitted isotropically. This thus allows for light to be redirected in ways favorable for its detection, such as a photon being emitted perpendicular to its original direction of travel. This is generally used with total internal reflection (or TIR) to allow light to enter the wavelength-shifting plastic but not leave until it reaches a point of the designer's choosing [27]. A more complete description of TIR is given in the next chapter.

1.5 Principles of Operations of Photomultiplier Tubes

Photons produced in a detector must be converted into an electronic signal that can be read and recorded by the data acquisition system. This is the role of the photomultiplier tube, or PMT. There are a large number of PMTs available from a number of manufacturers, but all operate on the same basic principles.

1.5.1 The Photocathode and Quantum Efficiency

Before a photon can be converted into an electronic signal, it must first reach the photosensitive part of a PMT: the photocathode. To do this, the photon must pass through the PMT bulb, or envelope, designed to shield the photocathode and other PMT components from the surrounding environment. This bulb is typically made from borosilicate glass or some similar material, and, for sufficiently short-wavelength light, may actually be opaque and prevent photons from reaching the photocathode.

Those photons that do penetrate the glass envelope must be converted into photoelectrons at the photocathode. To do this, the photocathode is constructed of a low work-function material, where the "work-function" is the energy required to liberate an electron from an atom or molecule. The visible photon thus captures photoelectrically on the low-work-function electron and frees it. The electron then migrates through the photocathode under the influence of an electric field in order to reach the rest of the photomultiplier tube. This process, however, is not perfectly efficient, and the conversion rate between incoming photons and outgoing photoelectrons at the photocathode is described by the quantum efficiency of the PMT. This value depends on the material used for the photocathode and on the wavelength of the incoming photon, with each material having a different range over which it is efficient. For large photomultiplier tubes, the exact quantum efficiency of the PMT will vary over the bulb's surface and especially fall off towards the edges of the PMT where the electric field is weakest and liberated electrons are more likely to be recaptured in the photocathode material. The maximum quantum efficiencies for photomultiplier tubes generally fall in the range of 10-40%.

1.5.2 Gain

Once a photoelectron successfully escapes the photocathode, it must then be multiplied to produce a readable electronic signal. This is done through multiplication on the PMT's dynodes. The dynodes are also constructed of a low work-function material, so that a maximum number of electrons will be liberated for a given input energy. To achieve multiplication, the original photoelectron is accelerated through a vacuum towards the first dynode by an electric field. The electron, now imparted with energy from the electric field, slams against the dynode and transfers its energy to the dynode's material. Due to the low work-function of the dynode material, this liberates a number of new electrons, which are then picked up and accelerated by another electric field towards the second dynode. This process then repeats itself, with each electron causing the release of several other electrons, on each dynode in the PMT. A PMT will generally have eight to twelve dynode stages. At the end of the dynode chain, all of the multiplied electrons are collected on the PMT anode and converted to a current pulse which is propagated down the signal wire to the rest of the data acquisition system. The exact multiplication achieved is called the gain of the PMT, and varies between different models and depending on the applied voltage, though it is often around 10^8 for a nominally operating PMT.

1.5.3 Dark Noise

A final principle to discuss with photomultiplier tubes is dark noise or current. Occasionally, in the absence of any photons, a PMT will still produce an electronic pulse, collectively known as dark noise (or, if integrating the noise over time, dark current). There are several potential sources of dark noise that can never be completely eliminated. The most prominent is thermionic emission from the dynodes and photocathode. Because low work-function materials need to be selected for these applications, stochastic thermal vibrations in the medium will sometimes impart enough energy to an electron to liberate it. The electron is then carried, identical to a photoelectron, through the dynode chain and multiplied, creating a current pulse that can be identical to a legitimate signal pulse.

A second, generally less prevalent source of dark noise in properly-functioning PMTs, is leakage current, where electronic signals and noise from one part of the PMT system (generally the high voltage components) "leaks" to the output signal. This is particularly noticeable when operating the PMT at a low voltage (and thus low gain). On the other end of the spectrum, if the PMT is operated at too high of a voltage, field emission will begin to occur, where the electric field becomes too great and electrons are ripped from the dynode by the force of the field alone. This should not occur in a properly functioning PMT and will rapidly degrade PMT performance if it does.

A final source of dark noise is from ion feedback. The inside of a PMT is nominally kept at vacuum to allow for electrons to travel unimpeded, but in reality no perfect

vacuum is possible. Occasionally a passing electron will ionize a stray gas molecule in the PMT volume. This now-charged molecule will then be accelerated in the opposite direction as the electron towards the previous dynode. Due to its large mass, this process takes a longer amount of time than it takes the electrons to continue through the avalanche and produce a signal. When it does strike the previous dynode, it too will liberate a number of electrons, which will subsequently be accelerated and cause a second multiplication avalanche. Thus, this source of dark noise generally appears as afterpulsing, where a second pulse is seen after some delay from the larger, legitimate signal pulse. Depending on the settings of the data aquisition system, and the exact length of the delay, these pulses can be misinterpreted as a new signal pulse or incorrectly integrated as part of the original signal pulse. A second source of afterpulsing is from electrons elastically scattering on the dynodes, though this process creates pulses after a very short delay [38].

The dark noise is significant in a large-scale water-Cherenkov detector application due to the large number of PMTs present in such detectors. Imagine, as an example, a detector incorporating 3,600 PMTs, each of which has a dark rate of 4,000 Hz (roughly the expected dark rate for a Hamamatsu 10-inch PMT). This means that each PMT in the detector will fire approximately every 250 microseconds. Modeling the dark noise according to an exponential distribution indicates that the probability, P of a PMT firing in a timing window of t is:

$$P = 1 - e^{-Rt} \tag{1.3}$$

where R is the dark rate of the PMT in Hertz. In any given 1 microsecond window, then, one can expect 14 out of the 3600 PMTs to falsely output a signal pulse. In a much more stringent window of 9 nanoseconds, which is often used to reconstruct attributes of an an antineutrino event, one can expect 0.13 PMTs to output a signal, or one PMT every 8 timing windows. This indicates that, while the dark noise of the PMTs alone are unlikely to falsely produce candidate antineutrino events, it may cause PMTs to fire in an event even if the PMT is not struck by a photon, degrading the ability of reconstruction algorithms to accurately determine the location or energy of an event. Increasing the number of PMTs present in a detector will further drive this effect.

1.6 Antineutrino Detector Applications to Nuclear Non-Proliferation

Now that we have established the behavior of the antineutrino and how it may be practically detected, it is worthwhile to return the discussion to the potential end-use application that is the focus of this work: using antineutrinos to aid the global nuclear non-proliferation regime. The global desire to limit the spread of nuclear weapons was codified in 1968 when the Treaty on the Non-Proliferation of Nuclear Weapons

(NPT) was opened for signature [39]. Today, all states except five have signed the treaty, with India, Israel, Pakistan, and South Sudan never signing the treaty and the Democratic People's Republic of Korea (DPRK) withdrawing from the treaty in 2003 [40]. The NPT established five states, the United States, Soviet Union, China, United Kingdom, and France, as nuclear weapons states while all other signatories agreed to be non-nuclear weapons states. These non-nuclear weapons states agreed to not pursue or acquire nuclear weapons and, in exchange, the nuclear weapons states would assist them with the peaceful uses of nuclear technology. This created the global nuclear nonproliferation regime, whose mission has been primarily, though not exclusively, carried out by the International Atomic Energy Agency, or IAEA. This section will first give a brief overview of the IAEA's safeguards efforts, followed by non-proliferation efforts outside of the IAEA safeguards regime, and finally by the benefits that antineutrino detectors may have on both.

The IAEA has worked since its founding to both allow states access to the peaceful benefits of nuclear technology and prevent those same states from developing their own nuclear weapons [41]. It has done the latter of these goals through the process of the international safeguards regime. The IAEA uses two main tools as part of its safeguards regime. First is nuclear material accountancy, or NMA, and second is containment and surveillance, or C/S. NMA is, at its most simple, a form of counting exercise; a state declares how much nuclear material it has in its possession, and the IAEA seeks to verify this declaration [42]. Any material declared but not found by inspectors or material discovered but not declared is considered "material unaccounted for," or MUF, which may have been diverted to a nuclear weapons program.

While this NMA process sounds simple in practice, it is made practically challenging by the large amount of time and effort required to inspect and verify every piece of nuclear material in a state. Measuring the amount of nuclear material in, for example, freshly spent nuclear fuel or the fuel currently in a reactor, can be difficult, if not impossible. Therefore, the NMA process is complemented by C/S [43]. C/S's goal is not to prevent a state from accessing its nuclear material, but merely to detect whether a state *has* accessed its nuclear material since the last inspection. This is done using a series of cameras and seals, collectively known as tamper indicating devices (TIDs) [44]. These TIDs can be deployed on a canister of spent fuel, for example, so that an inspector only needs to verify the integrity of the seal used rather than take inventory of the entire canister; if the the state has not accessed the canister since the last inspection, the amount of material inside should be the same.

NMA and C/S are focused on verifying the existence and quantity of material already declared by a state to the IAEA. There is, however, an additional duty of the IAEA, codified in the Additional Protocols, to ensure that a State's declarations are complete [45]. That is, the IAEA must ensure that there do not exist nuclear materials kept secret from the agency and completely apart from the safeguards regime. The need for this additional verification was made clear in the aftermath of the Gulf War, where it was revealed that, while Iraq's *declared* nuclear material and facilities were

properly accounted for under safeguards, it also had a large amount of *undeclared* material and facilities that were not formally declared to the IAEA and thus not included in the safeguards regime, which it was using to perform nuclear weapons research [46].

Not all nuclear non-proliferation actions are carried out through the IAEA and its safeguards regimes. Treaties and agreements exist outside of this framework that seek to constrain or prevent a state's development of nuclear weapons. While these treaties often involve the IAEA (generally to determine States' compliance with the treaty terms) they are not part of the specifically-defined international safeguards regime. One now defunct example of such a treaty is the Agreed Framework between the United States and DPRK, a bilateral treaty which sought (ultimately unsuccessfully) to prevent the DPRK from using their nuclear reactors to produce material for a nuclear weapon [47]. A more recent example is the Joint Comprehensive Plan of Action, colloquially known as the Iran Nuclear Deal, a multilateral deal between Iran, the countries of the European Union, and the United States which sought to prevent Iran's ability to produce and stockpile enriched Uranium for constructing a nuclear weapon [48]. While both agreements involved the IAEA in their implementation, they were separate bilateral or multilateral agreements between States and thus existed outside of and in addition to the IAEA's normal safeguards regime.

Antineutrino detection has the capability to augment the nuclear non-proliferation regime either through assisting the IAEA in its nuclear safeguards mission or serving to monitor treaty compliance and build confidence in other nuclear non-proliferation agreements or treaties. Antineutrino detectors may assist in both verifying the *correctness* and the *completeness* of a State's safeguards declarations or declarations made in other agreements for any state that may seek to use a nuclear reactor to produce special nuclear material for a weapons program [49]. First, smaller-scale antineutrino detectors deployed at a meter-scale distance from a nuclear reactor core can be used for reactor monitoring [50]. Such a detector could verify the operations of the reactor in near-real time and, if sufficiently sensitive, can monitor the power, burn-up, and fissile content of the core. All this information would be available in-between, or in the absence of, in-person inspections, allowing the IAEA or treaty State parties to maintain a positive continuity of knowledge over the material in the reactor core at all times. This would be a powerful tool for verifying a state's declarations about how much uranium and plutonium it has present in a nuclear reactor.

Large-scale antineutrino detectors deployed at a kilometer to tens-of-kilometers scale distance from the reactor core have the capability to assist the IAEA or other party in a nuclear non-proliferation treaty in both the discovery and monitoring of nuclear reactors [51]. One possible application would be as a cooperative confidence building measure between two states, which would be a measure short of a treaty, to ensure that undeclared nuclear material is not being generated [52]. To monitor an operating reactor, a large-scale detector would behave in principle the same as the small-scale detector described above, albeit at a much greater distance from the

reactor core (kilometers instead of meters). This increased distance does come with a trade-off, however; not only must the detector be larger (and thus more expensive), but it also would likely lose the ability to monitor the burn-up or fissile content of the core, as constructing a large detector sensitive enough and with enough energy resolution to measure those quantities is cost prohibitive. The detector would instead be able to only monitor the operational status and reactor power at a distance. In the most simple case, such a detector would monitor the reactor for unplanned shutdowns, when nuclear fuel may covertly be removed from the reactor. The detector, then, must be able to reject the null hypothesis that the nuclear reactor is operating at power and thus the antineutrino output is non-zero (or is equal to some predetermined rate).

In addition to the reactor monitoring case described above, a large-scale detector would also be able to detect, or exclude the existence of, an operating nuclear reactor in a large (tens or even hundreds of kilometers scale) radius around it. This would be a useful capability for verifying the completeness of a State's safeguards declarations, its compliance to a non-proliferation treaty, or as a confidence building measure by ensuring that an undeclared nuclear reactor is not being used to create illicit special nuclear material for a nuclear weapons program. In this case, the detector must be able to reject the null hypothesis that there is no nuclear reactor operating in the specified range and thus the antineutrino output of that hypothetical reactor is zero (or, put another way, that the antineutrino rate detected is equal to the background rate). In order to maximize the area that the detector can successfully exclude or monitor, however, detector volume must be maximized, creating a more expensive detector.

Other emerging and existing technologies, such as satellite imaging paired with artificial intelligence algorithms, may also be able to discover or monitor nuclear reactors without the need to construct a large-scale detector [53]. Such methods provide indirect information on the operations of the nuclear reactor – such as by monitoring the number of trucks entering and exiting the facility in a day, or observing steam being emitted from a cooling tower – and could, in principle, be thwarted by deception and camouflage. An antineutrino detector can complement these other technologies by providing a direct measurement of the nuclear reactor core, and the reactor's antineutrino output is impossible to shield from the detector. Further, it would be nearly impossible to spoof the signal from a nuclear reactor, as no other source of antineutrinos can produce them in the same quantity and with the same energy spectrum. Other techniques, such as environmental monitoring for traces of uranium or plutonium, can also be used to discover an undeclared nuclear reactor. These techniques require samples to physically be collected within the reactor's vicinity and provide little information on the operation of the reactor itself [54]. Antineutrino detectors could similarly be used in synergy with these methods.

Large-scale antineutrino detectors require a large capital investment. While this is likely infeasible for the IAEA alone to implement within its safeguards regime, it is more likely that an interested State party, such as the United States, would

be willing to finance such a detector for the sake of monitoring compliance with some future nuclear non-proliferation treaty or as a confidence building measure with some other State. In this role, the antineutrino detector would operate the same as described above, either by monitoring a known nuclear reactor or verifying the absence of unknown nuclear reactors pursuant to the treaty being enforced or the terms of the confidence building measure. It is these detectors that the inclusion of wavelength-shifting plates may benefit, as they may be able to reduce the cost or improve the performance of the detector compared to a detector that does not include wavelength-shifting plates.

1.7 Benefits of Wavelength-Shifting Plates to Non-Proliferation Applications

Antineutrino detectors, especially large-scale antineutrino detectors, can be very expensive tools. For even a small-scale detector, the fill material (if it uses scintillator instead of water) and the photomultiplier tubes can create a rather formidable capital cost that complicates implementation into any realistic non-proliferation application. This problem is only exacerbated with large-scale detectors. For these detectors, not only must the detector itself be built, but it also must be located beneath a large amount of earth to act as shielding from cosmic radiation, particularly muons, that can drown out any antineutrino events that occur in its volume [55]. Constructing a large, underground experiment hall to house the detector is a large capital cost investment in addition to producing the detector components themselves. Of these components, one of the largest costs are the PMTs used, due to both their high individual cost due to tight constraints on quantum efficiency, mechanical requirements, and intrinsic radioactivity, and also the large number in which they are employed, generally in the thousands. It is paramount, then, to maximize the performance of each individual PMT.

This is the goal of incorporating wavelength-shifting plates in the detector. Compared to PMTs wavelength-shifting plastic is very cheap, and so mating each PMT in the detector to a wavelength-shifting plastic plate may be a more cost-efficient way to improve detector performance compared to adding additional PMTs. The increased light collected by the wavelength-shifting plates can translate to increased energy resolution, as the light that would have otherwise been lost can be used to more accurately reconstruct the original energy of the positron created in the detector. The increased light collection may also be able to increase the overall efficiency of the detector as events that may have otherwise not been detected or properly identified due to a lack of light may now be seen by the detector.

There are a number of other alternative technologies that may be able to increase the amount of light collected in a large-scale water-Cherenkov detector. Some, such as dichroicons and Winston-style light cones, may also be able to increase the light

collection of individual PMTs [56]. These cones may be effective at increasing an individual PMT's light collection efficiency and, in the case of dichroicons, allow for separation of the light based on its wavelength; however, they are also generally more expensive and difficult to scale to larger areas compared to wavelength-shifting plates, and do not shift Cherenkov-spectrum light to a more favorable wavelength for detection. Additionally, dichroicons are a novel technology and thus their use in a large-scale detector would create technological risk. Other technologies, such as water-based liquid scintillator, can increase the light produced by antineutrino interactions in the detector, achieving the same overall goal as wavelength-shifting plates [25]. However, like dichroicons, this technology is still under development and the capability to fill a large-scale detector with such a water-based liquid scintillator must still be demonstrated. The choice between these different technological options can thus be represented as a choice between expediency and risk. Wavelength-shifting plates are a proven technology and their inclusion in a water-Cherenkov detector entails little technological risk; however they also do not provide as much benefit as other technologies could, such as the wavelength-separation capability of dichroicons or the greatly improved light output of water-based liquid scintillator. The choice of a best technology for a given application depends on the level of technological risk the designer is willing to assume.

The greater performance at a low margin of cost provided by wavelength-shifting plates is beneficial for the potential use of large-volume antineutrino detectors as part of a nuclear nonproliferation regime. The implementation of wavelength-shifting plates into such detectors may improve their ability to detect or exclude the presence of an undeclared nuclear reactor within a certain range, or to monitor a declared nuclear reactor. The extra light collected by the wavelength-shifting plates may be able to increase the range over which a detector may operate, or decrease the amount of dwell time required for measurements, all at a relatively small increase in cost.

Wavelength-shifting plates may also be able to reduce the cost of a large-scale antineutrino detector. As discussed, a large part of the cost of a large detector is its numerous photomultiplier tubes. The extra light collected by the wavelength-shifting plates may be able to compensate for a reduction in the overall number of these tubes. This could allow the detector to retain the same performance using fewer photomultiplier tubes, and thus at a reduced cost. This reduction in cost would serve to make the detector more attractive to budget-conscious treaty member States and thus more likely to be included in a future agreement.

As previously discussed, however, wavelength-shifting plates will likely degrade one's ability to accurately reconstruct the location of events that occur in the detector volume. This would serve to counteract, in part, the benefit gained from increased energy resolution by making it more difficult to discriminate signal events and background events by the location they occur at in the detector. For wavelength-shifting plates to improve detector performance, and thus aid the nuclear non-proliferation mission, the benefit gained from increased energy resolution and light collection effi-

ciency must outweigh the degradation the wavelength-shifting plates cause to position reconstruction. The rest of this work focuses on determining the magnitude of this trade-off: analytically, experimentally, and through simulations.

Chapter Two

A Theoretical Basis for Light Behavior in a Wavelength-shifting Plate

2.1 Overview

The overall light collection of a wavelength-shifting plate is instrumental in determining its utility in a large-scale water-Cherenkov detector. The goal of this chapter, then, is to explore the behavior of light in a wavelength-shifting plate in order to arrive at a theoretical model of the plate's light collection behavior. The results of this simple model can be used to better understand the experimental and Monte Carlo results presented in subsequent chapters.

2.2 Behavior of Light in a Wavelength-Shifting Plate

Once light is absorbed in a wavelength-shifting plastic plate, it will be re-emitted isotropically with a wavelength determined by the wavelength-shifting plate's emission spectrum and a delay determined by the decay constant of the plastic (typically on the order of a nanosecond). Once the photon is emitted, it may be trapped in the plate by total internal reflection, or TIR.

2.2.1 Total Internal Reflection

Total internal reflection refers to the phenomenon whereby light (or any wave) that reaches an interface going from a high index of refraction material to a low index of refraction material at a sufficiently oblique angle is reflected from the boundary totally rather than refracted or partially reflected. This is because the conditions for the light to refract into the new medium are no longer possible to fulfill, making reflection the only viable behavior at the boundary.

Consider a beam of light traveling towards an interface between two materials; one, in which the light beam begins, has an index of refraction of n_1, and the other,

towards which the light is traveling, has an index of refraction of n_2. The materials are defined so that $n_1 > n_2$. As the beam crosses from one material into the other, it will be refracted according to Snell's Law:

$$n_1 \sin(\theta_1) = n_2 \sin(\theta_2) \tag{2.1}$$

We now re-arrange the equation to find the angle at which the light beam is refracted in the new medium, θ_2:

$$\begin{aligned} \sin(\theta_2) &= \frac{n_1}{n_2} \sin(\theta_1) \\ \theta_2 &= \arcsin\left(\frac{n_1}{n_2} \sin(\theta_1)\right) \end{aligned} \tag{2.2}$$

It is shown from Equation 2.2 that there exists some angle where θ_2 goes to 90 degrees and past that ceases to exist:

$$\begin{aligned} 90\,\text{deg} &= \arcsin\left(\frac{n_1}{n_2} \sin(\theta_1)\right) \\ 1 &= \frac{n_1}{n_2} \sin(\theta_1) \\ \theta_1 &= \arcsin\left(\frac{n_2}{n_1}\right) \end{aligned}$$

We define this angle as the "critical angle," or θ_c:

$$\theta_c = \arcsin\left(\frac{n_2}{n_1}\right) \tag{2.3}$$

Therefore, if the beam of light approaches the boundary at this critical angle or greater, the light cannot be refracted into the second medium according to Snell's Law and thus must be totally reflected. This phenomenon is depicted in Figure 2.1.

For a wavelength sifting plastic plate with an index of refraction of 1.58 and water with an index of refraction of 1.33, this critical angle becomes 57.33 deg. Thus any light that is emitted in a horizontal plate between -32.67 deg and $+32.67$ deg relative to the horizontal will reflect from the boundary rather than escape from the plate. Additionally, if we assume that the reflection is perfectly specular (i.e. the surface roughness of the plate is ignored) and the two faces of the plate are perfectly parallel, once reflected the light will never be able to escape from either of the two surfaces. In an infinitely long plate, this means that the light will be trapped forever, while for a finite plate the light will instead be trapped until it reaches a different surface (such as the perpendicular edges of the plate). If the plate is placed in air ($n = 1.0003$) instead of water, the critical angle changes to 39.41 deg. In air, therefore, light emitted within ± 50.59 deg of the horizontal will be captured by TIR.

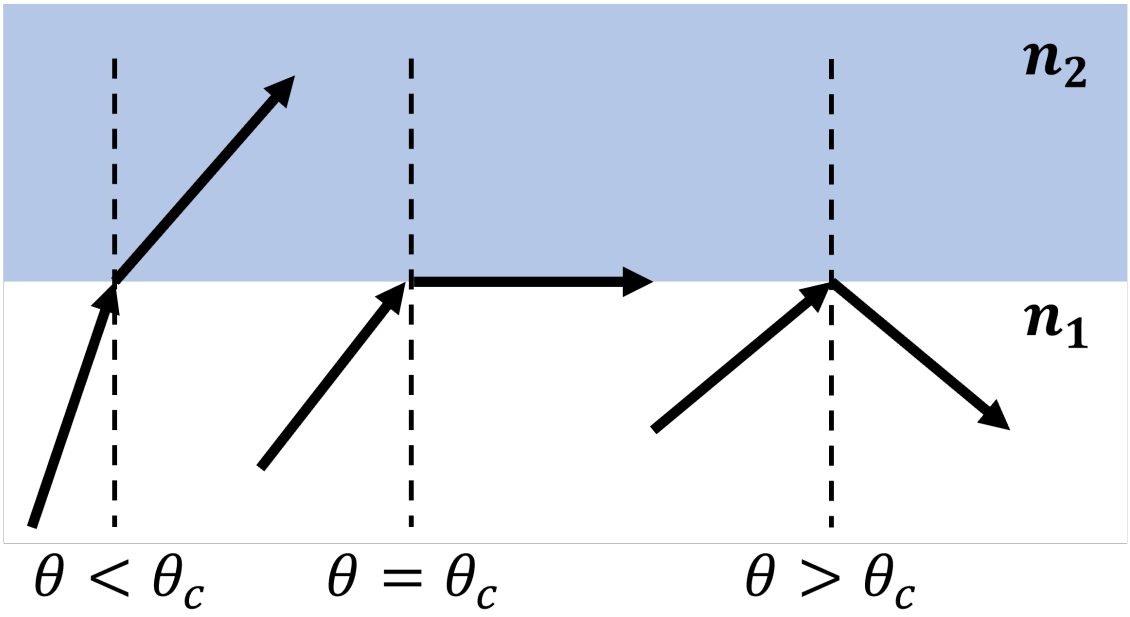

Figure 2.1 Light that approaches a boundary between two mediums with different indices of refraction at an angle greater than the critical angle will always be reflected, as Snell's Law forbids light to be refracted into the second medium. This effect can serve to retain light in a wavelength-shifting plate and guide it to a photomultiplier tube for detection.

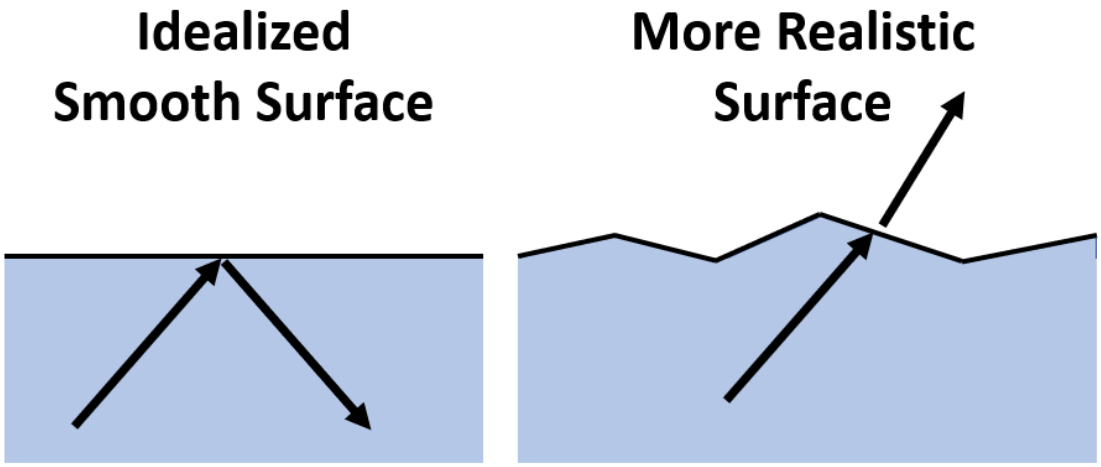

Figure 2.2 A graphical comparison of a wavelength-shifting plate surface between an idealized "smooth" case and an exaggerated case with surface roughness. Such roughness may allow for light that would be trapped by TIR under idealized conditions to escape, as the local angle at any given point on the surface may differ from the idealized angle of incidence.

As light is emitted in the wavelength-shifting plate isotropically, this means that there is a: $65.34/180 = 36.3\%$ chance of any emitted photon being captured in water, and a 56.2% chance of it being captured in air. This immediately makes evident one of the difficulties of achieving a high light collection efficiency using a wavelength-shifting plate: in a water detector, approximately 63.7% of the light absorbed in the plate will immediately be lost through one of the plate's surfaces.

An additional compounding factor is that no surface is truly "smooth". Instead, at any point on a surface, there will be present many small facets that may exist at different angles from the macro surface, as seen in Figure 2.2 [57]. If a previously captured photon strikes one of these surfaces, there is a chance that it could escape directly as it approaches at an angle less than the critical angle, or that it could be reflected from the surface at an angle that causes it to escape from the opposite face of the plate. The exact contributions of this effect on the light collection of the plate, however, is difficult to determine based on theory alone, particularly with limited information about the surface roughness of the plate in question.

2.2.2 Re-absorption

Due to the Stokes shift, discussed in the previous chapter, the re-absorption of emitted light in a wavelength-shifting plate is relatively unlikely. However, there is still some overlap between the absorption and the emission spectrum of the plastic, and thus

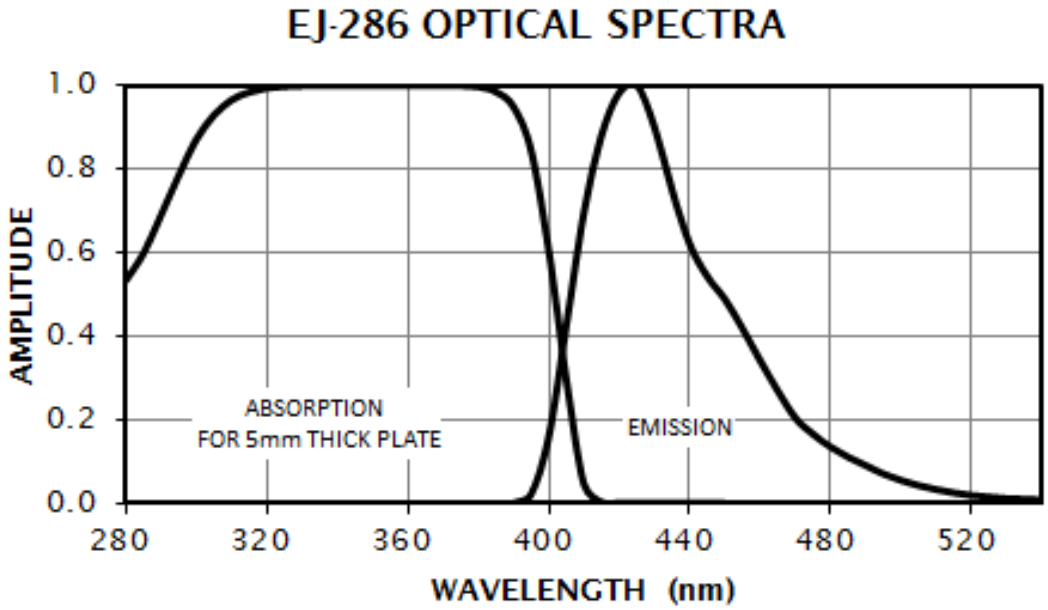

Figure 2.3 The emission and absorption spectrum of EJ-286 blue-shifting wavelength-shifting plastic plate. The overlap between the emission and absorption spectra indicate that some photons, once re-emitted, are at risk of re-absorption given a long enough path length through the material [58].

re-absorption is possible for some emitted wavelengths of light. Take, for example, the spectra of EJ-286, a commercial wavelength-shifting plastic produced by Eljen Technology, as shown in Figure 2.3. Any light that is emitted between around 380 nm and 410 nm and travels a sufficient distance through the plastic is at risk of being re-absorbed. Once re-absorbed, there is a chance for the light to be again re-emitted (this time at a wavelength that likely precludes further re-absorption) or it may be lost through nonradiative decay. The exact chances of this is defined by the quantum efficiency of the wavelength-shifting plastic (for the case of EJ-286, this is 92%). Even if the light is re-emitted, however, it will be created isotropically. This means that light that had previously been captured in the plate by TIR may instead escape into the environment after being re-emitted and be lost.

2.3 Behavior of Light at a Wavelength-Shifting Plate and PMT Interface

The geometry of the plate-PMT interface is important to define to understand how light will behave at the boundary. A "perfect" interface would be one that matches the surface of the PMT perfectly. There would be intimate contact between the plate

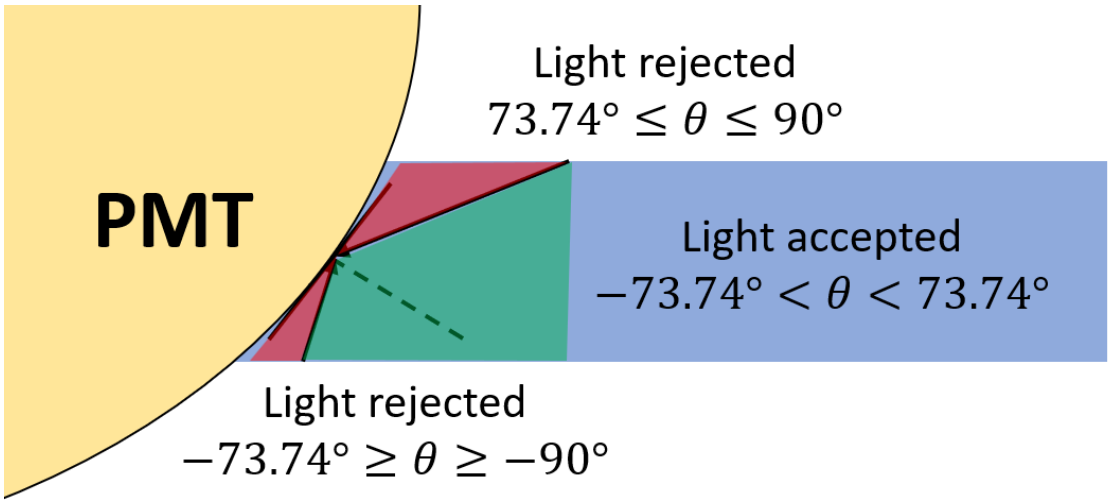

Figure 2.4 A "perfect" interface between the plate and the PMT with no gaps present between the two. Light incident on the interface in the wide range of -73.74 deg to 73.74 deg to the local surface will be transmitted; however sufficiently oblique light ($\theta > 73.74$ deg) can still be rejected from the boundary.

and the PMT at all points of the boundary. The behavior of light at such a "perfect" interface, illustrated in Figure 2.4, is relatively straightforward to consider. The index of refraction of a wavelength-shifting plastic plate is 1.58, while the index of refraction of borosilicate glass (from which the bulb of many large-area PMTs is made) is 1.5168. As the light will be traveling from a material with higher index of refraction one with a lower index of refraction, TIR can occur, albeit at the very oblique angle of 73.74 deg. However, as the PMT bulb is curved, whether or not a photon is rejected from the surface or not is dependant on both the incoming angle of the light and the exact local angle of the boundary at the point of intersection. If the photon impinges on the PMT with an angle less than 73.74 deg relative to the local interface angle, it can be assumed that the photon will be transmitted and potentially "seen" by the PMT (though in reality, effects such as partial reflection or the previously discussed surface roughness may occasionally reject the photon). Additionally, depending on the angle at which the light enters the PMT glass, it may fail to strike the PMT's photocathode, instead escaping from the PMT back into the detector medium, though this effect is expected to be minor and not further considered as a part of this theoretical analysis. While a true "perfect" interface may be somewhat difficult to construct, it may be approximated with the use of an optical epoxy or gel that has an equivalent index of refraction to both the wavelength-shifting plate itself and the borosilicate glass of the PMT.

On the opposite end of the spectrum from the "perfect" interface is a surface that is perpendicular from the flat surfaces of the wavelength-shifting plate, as seen in Figure 2.5. A gap would exist at all possible points between the end of the wavelength-shifting plate and the beginning of the PMT's glass bulb, which would be filled with the detector medium. There would not exist any points of intimate contact between the plate and the PMT. As light reaches this boundary, it would have a chance of being rejected by TIR based on the indices of refraction of the plate and the detector medium (resulting in critical angles of 39.41 deg and 57.33 deg for air and water, respectively). Considering the problem in two dimensions, as seen in Figure 2.5, shows that light trapped between two parallel surfaces by TIR will often be able to escape through a third perpendicular surface.

The range of angles by which light can strike the interface boundary is limited if one assumes that the light is previously trapped in the wavelength-shifting plate by TIR. Considering light that has reflected most recently off of the "bottom" boundary, it can be seen that light can strike the boundary only at angles between 0 deg and $90\,\text{deg} - \theta_c$ with respect to the horizontal. Similarly, light that is reflected most recently off of the "top" boundary will always strike the interface with an angle between $-90\,\text{deg} + \theta_c$ and 0 deg.

Consider a photon trapped between the two parallel surfaces with an angle of $90\,\text{deg} \geq \theta \geq \theta_c$. Such a photon will always impinge on the perpendicular surface with an angle of $90\,\text{deg} - \theta$. Thus, in order to be trapped by TIR, $90\,\text{deg} - \theta \geq \theta_c$. Considering the edge case of $\theta = \theta_c$, $90\,\text{deg} - \theta_c \geq \theta_c$ so that $\theta_c \leq 45\,\text{deg}$. Therefore, any photon that is trapped in the plate by an angle of $45\,\text{deg} \geq \theta \geq \theta_c$ will be rejected from the boundary; the rest will be transmitted. Practically speaking, this means that, in water with a critical angle of 57.33 deg, no light will be rejected from the boundary, while in air with a critical angle of 39.41 deg, light in the narrow range of $39.41\,\text{deg} \leq \theta \leq 45\,\text{deg}$ will be rejected from the interface, accounting for approximately 11% of the light trapped within the plate.

Instead of a perpendicular cutoff, the plate can be machined to have a 45 deg taper on the PMT hole, allowing for a closer-to-perfect matching between the plate and the bulb. This design allows for a single ring of intimate contact between the plate and the PMT with a small gap across the remainder of the interface. We may now consider the probability of light being rejected from this boundary as we did for a perpendicular boundary. For the sake of these optics calculations, there is assumed to be a gap across the entire plate-PMT interface, rather than any intimate points of contact. In reality, with intimate points of contact between the plate and the PMT, the transfer of light between the two will be slightly improved from the values presented below.

Similar to the previous case, light will generally impinge on the boundary between the angles of $-90\,\text{deg} + \theta_c$ and $90\,\text{deg} - \theta_c$, depending on which surface the light reflects from before reaching the boundary. There is a small exception in this case, as light traveling at an angle less than $-45\,\text{deg}$ will never impinge upon the boundary; this

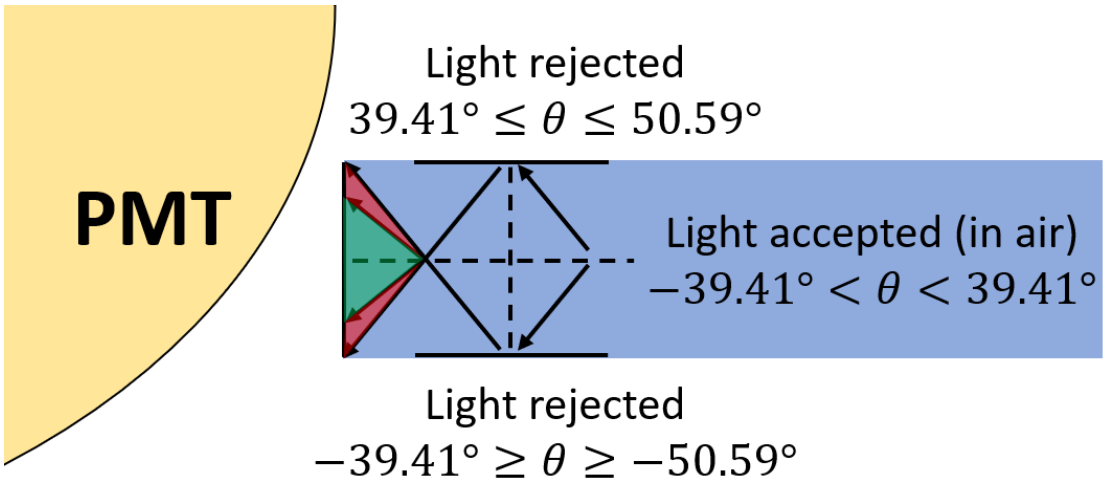

Figure 2.5 A "flat" interface between the plate and the PMT with a gap between the plate and the PMT at all points. The maximum angle (in air) that a photon can strike on the interface, assuming it is captured by TIR in the plate beforehand, is 59.59 deg. This limits the amount of light that can be rejected from the boundary to a generally narrow band between the critical angle and 90 deg minus the critical angle.

serves as a lower edge case.

In air, as seen in Figure 2.6, light that strikes the boundary at an angle between 5.59 deg and 50.59 deg (90 deg $-\theta_c$) will be transmitted. Light that strikes the boundary with an angle between 5.59 deg and -45 deg, on the other hand, will be rejected. Practically speaking, this means that all light that reflects most recently off of the "top" plate surface, which is constrained to fall within -50.59 deg and 0 deg will be rejected (between -45 deg and -50.59 deg, the light will not even hit the boundary and instead will reflect off of the bottom plate surface before striking the boundary). Most of the light that has reflected from the bottom boundary will be transmitted, other than the light at an angle between 0 deg and 5.59 deg. To convert this into a probability of light penetrating the boundary, first consider light reflecting off of the "top" surface. In this case, 89% of the light will be rejected from the boundary while the other other 11% of the light will reflect off of the "bottom" surface before hitting the boundary. This light will be constrained to now hit the boundary with an angle between 45 deg and 50.59 deg, and thus will always be transmitted.

Considering light most recently reflected off of the "bottom" surface, 89% of the light will be transmitted while the remaining 11% of the light will be rejected. Assuming light is equally likely to reflect from the "top" or "bottom" surface before impinging on the boundary means that 50% of the light will be transmitted, while the other 50% is rejected.

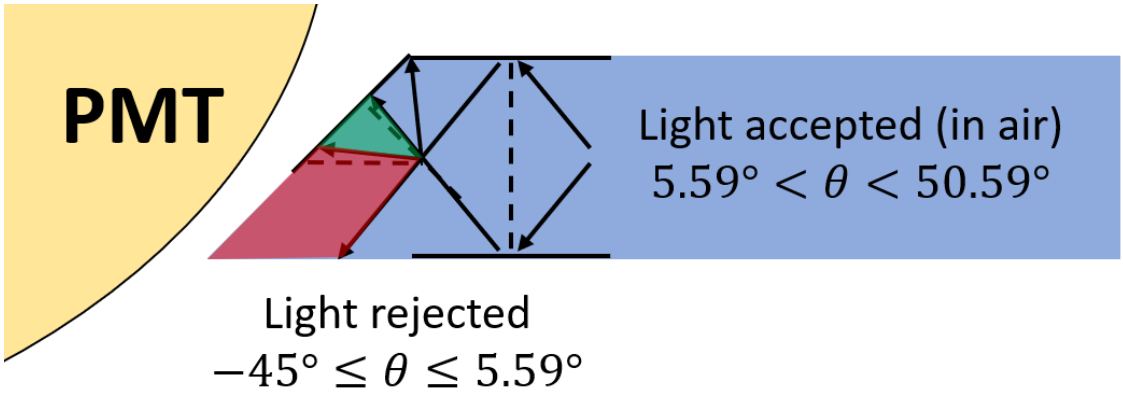

Figure 2.6 A simplified 45 deg interface between the plate and the PMT with a gap between the plate and the PMT at all points. In air, much of the light is rejected from the boundary, because light trapped in the plate by TIR is constrained to often approach the boundary at angles conductive to being rejected. This is particularly the case for light that is reflected off of the top surface, as all possible angles of approach result in the light being rejected.

This calculation can be repeated for a plate submerged in water, as seen in Figure 2.7. The math remains much the same, with 38% of the light coming from the "top" surface being transmitted and 100% of the light from the "bottom" surface being transmitted. This results in, overall, 69% of the light impinging on the boundary being transmitted, a marked improvement over the same conditions in air.

It is interesting, then, to consider how overall light collection may be affected comparing between a wavelength-shifting plate in air and one in water. For this analysis, we consider a 45 deg interface between the plate and the PMT, as described above. In air, 56.2% of light will initially be trapped in the plate by TIR while only 50% of that same light will be transmitted through the plate-PMT interface. This gives an overall efficiency of 28.1% for capturing and transmitting light in air. Performing the same calculation in water, 36.3% of light will be trapped by TIR and 69% of light will be transmitted through the interface, resulting in an overall efficiency of 25%. This indicates a remarkable level of similarity between the plate's behavior in air and in water, meaning that, overall, the plate can be expected to behave similarly in both media despite their very different indices of refraction.

This simple treatment, however, assumes a medium-gap across the entirety of the PMT-plate interface. As previously described, in reality there will be a ring of intimate contact between the plate and the PMT where nearly all light will be transmitted. Additionally, as in the previous case, this only accounts for one dimension of the light's travel. Photons can also be rejected from the boundary in the horizontal plane based on the local angle at the point of intercept and the photons direction

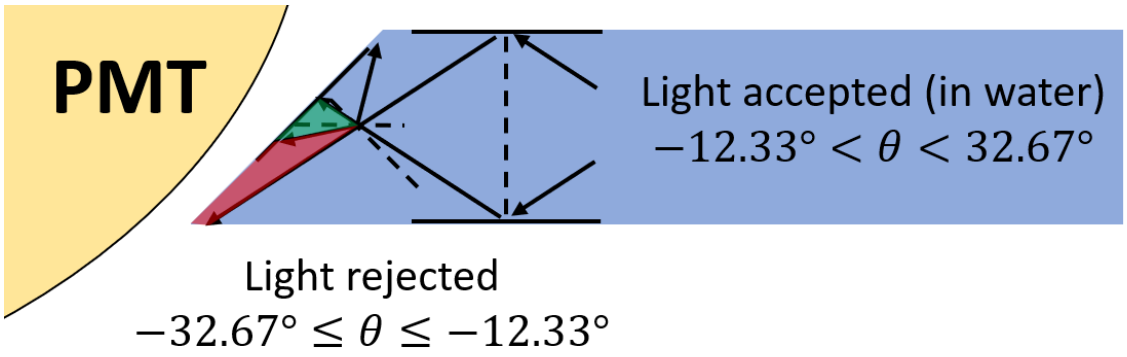

Figure 2.7 A simplified 45 deg interface between the plate and the PMT with a gap between the plate and the PMT at all points. In water, much of the light is still rejected from the boundary due to the same constraint as in air. However, in water, there is a small set of angles between 0 deg and 12.33 deg where light is able to escape after being reflected off of the top surface.

of travel. Despite this, an approximate 50% efficiency of transmitting photons is a good order-of-magnitude estimation for this type of boundary. While this boundary has a lower theoretical light transmission compared to the other types of boundaries described above, it does carry with it some practical advantages, as it is easier to manufacture than a "perfect" interface and easier to couple to a PMT than a perpendicular boundary.

2.4 Mathematical Models for Light Transport in a Wavelength-Shifting Plate Geometry

It is desirable to develop a first-principles model of light transport in a wavelength-shifting plate geometry to provide a point of comparison for both experimental results and future Monte Carlo simulations. This can be done by utilizing principles of ray tracing to determine the path length light must travel in the plate before intersecting with a PMT, which will be explored here.

First, it is necessary to mathematically describe the wavelength-shifting plate geometry. For the purposes of this exploration, it is useful to consider the lower left corner of the wavelength-shifting plate as the point $(0, 0)$, with the plate extending a distance L in the x-direction and a distance W in the y-direction. A hole of radius R is centered at the point (h_x, h_y) (so that, for a hole centered on the wavelength-shifting plate, $h_x = L/2$ and $h_y = W/2$). This geometry can be seen in Figure 2.8. Light does not however, have to travel directly from its point of creation to the hole. Instead, it may instead strike one of the outer edges of the plate. If the edge is assumed to

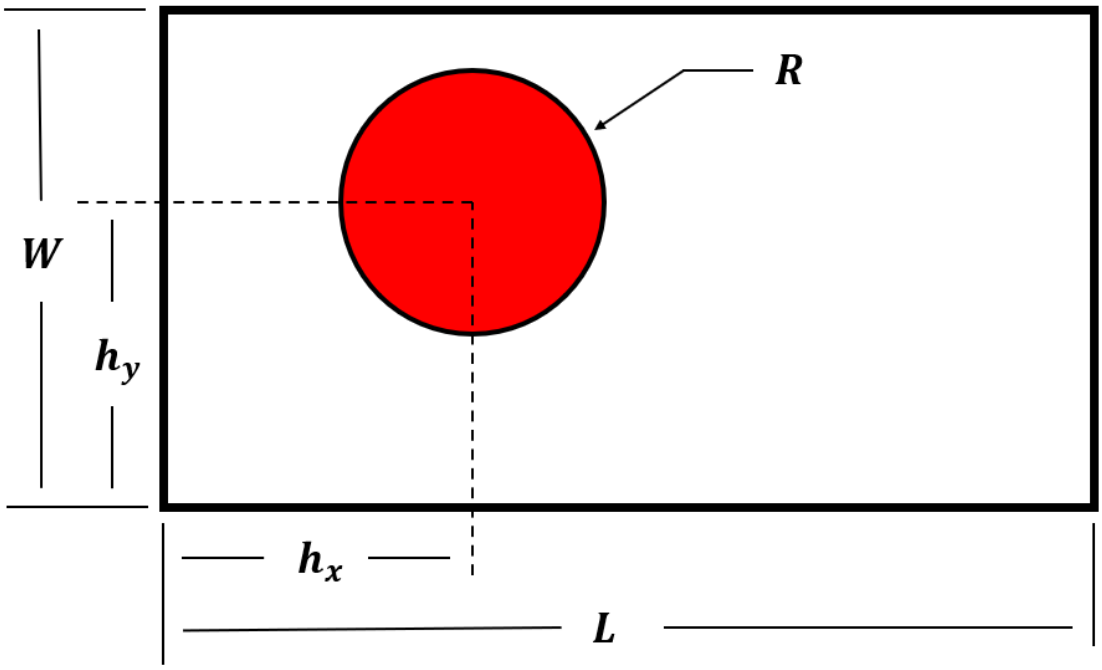

Figure 2.8 A representation of how a wavelength-shifting plate can be defined in the analytical model. The plate is defined with an arbitrarily positioned hole of arbitrary size to represent the PMT coupled to the wavelength-shifting plate.

be covered in a perfectly specular reflector, the light may reflect a number of times off of the outer edge of the plate before reaching the PMT. Rather than reflecting the light, however, it is mathematically simpler to reflect images of the PMT across the $x = 0$, $x = L$, $y = 0$, and $y = W$ lines, and again over the reflection of those lines. The end result is a series of holes of radius R centered at the points $(L(n_x + (n_x \mod 2)) + h_x(2(n_x \mod -2) + 1), W(n_y + (n_y \mod 2)) + h_y(2(n_y \mod -2) + 1)$ where n_x and n_y are integers in the set $\mathbb{Z}$ and $\mod$ is the modulo operator. This system of reflected holes can be seen in Figure 2.9.

It is convenient to use matrix mathematics to find the closest intersection between a ray cast by a photon traveling from a point $\boldsymbol{P}$ in a direction $\boldsymbol{D}$ and a circle centered on point $\boldsymbol{C}$. The intersection point between the ray and the sphere can be thus

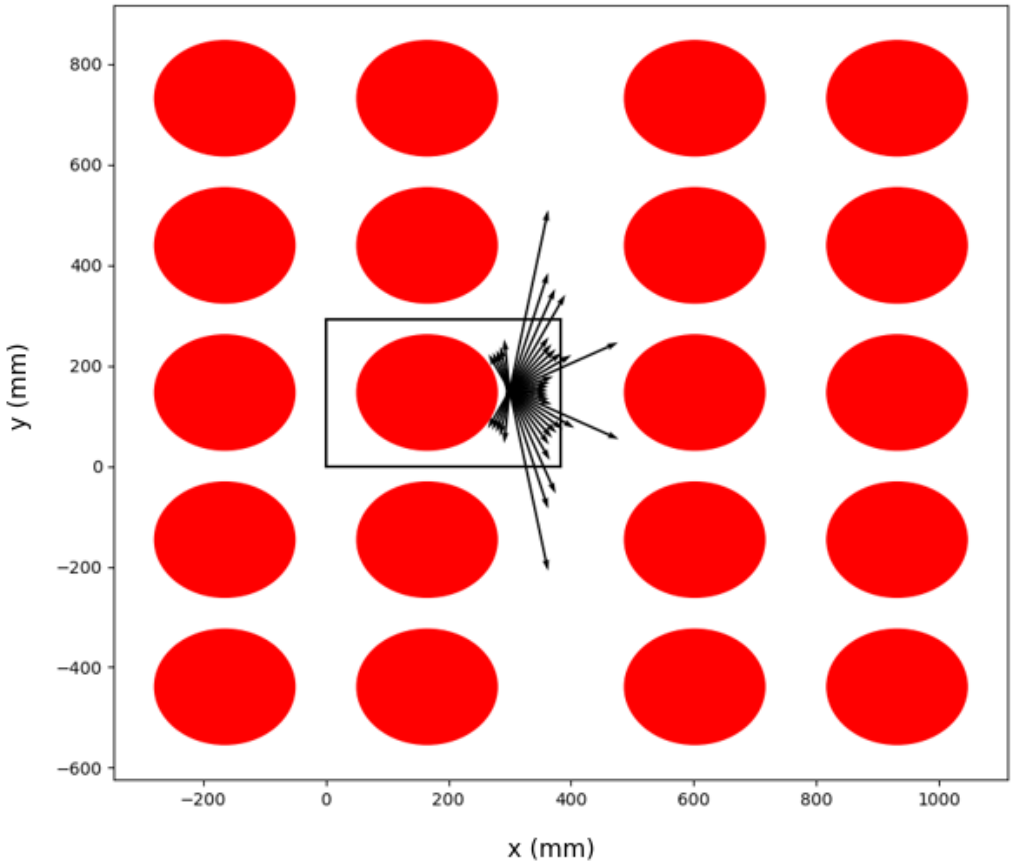

Figure 2.9 A representation of the analytical model geometry, with the boundaries of the wavelength-shifting plate outlined in black. The series of red circles are images of the target PMT reflected across those boundaries. The arrows are representative of the calculated distance from an arbitrary point in the plate to the nearest PMT image across a variety of angles.

defined:

$$\boldsymbol{X}(t) = \boldsymbol{P} + \boldsymbol{D}t \tag{2.4}$$

$$|\boldsymbol{X} - \boldsymbol{C}|^2 = R^2$$

$$t = \frac{-\boldsymbol{D} \cdot \boldsymbol{\Delta} \pm \sqrt{(\boldsymbol{D} \cdot \boldsymbol{\Delta})^2 - \boldsymbol{D}^2(\boldsymbol{\Delta}^2 - R^2)}}{\boldsymbol{D}^2} \tag{2.5}$$

where:

$$\boldsymbol{\Delta} = \boldsymbol{P} - \boldsymbol{C}$$

In these equations, if $\boldsymbol{D}$ is a unit vector, t is the distance traveled by the photon to reach the intersection point $\boldsymbol{X}$. The value of t may be positive or negative; if it is negative, the intersection point is opposite of the ray's direction of travel and should be discarded. Equation 2.5 may return 0, 1, or 2 results. In the case of zero results, there is no intersection point between the ray and the circle. For one result, the ray is perfectly tangent to the circle, and for two results, the ray passes through the circle and thus intersects at two points. In this case, only the closer point (minimum t) is important.

Equations 2.4 and 2.5 can be used to find the intersection point of a ray cast from the photon's origin point to any number of reflected circle images. To do this, the value of $\boldsymbol{C}$ must be defined as:

$$\begin{aligned}\boldsymbol{C} = [&L(n_x + (n_x \mod 2)) + h_x(2(n_x \mod -2) + 1),\\ &W(n_y + (n_y \mod 2)) + h_y(2(n_y \mod -2) + 1]\end{aligned} \tag{2.6}$$

The other matrices can also be defined for completeness:

$$\boldsymbol{P} = [x_0, y_0]$$

$$\boldsymbol{D} = [v_x, v_y]$$

It is possible that there is no valid intersection point between the ray and the circle, even if n_x and n_y are allowed to range to infinity. Such a case can be imagined for a ray cast perfectly vertically, passing between circle images without ever intersecting. As a point of practicality, for any realistic application where n_x and n_y are limited to a non-infinite set of values, there is also the possibility of no valid intersection being found for a ray even if one does exist.

Let us now consider the case of a photon created at the point $[x_0, y_0]$ and travelling in the direction $[v_x, v_y]$ through a wavelength-shifting plate. Using Equation 2.5, it is possible to calculate the nearest intersection between the photon and the PMT, as represented by the circle and its reflected images. It is of interest, then, to translate the distance to this intersection into a probability of photon survival.

There are two possible methods that we will consider here for a photon to be destroyed before it reaches the PMT. The first is re-absorption in the wavelength-shifting material. Photon attenuation in a medium is a well-understood phenomenon,

described by the exponential relationship:

$$I(t) = I_0 e^{-t/\lambda} \tag{2.7}$$

$$P(t) = e^{-t/\lambda} \tag{2.8}$$

where I is the intensity of a beam after traveling a distance t, I_0 is the initial intensity of a beam, λ is the mean free path of the photon through the medium, and P is the probability of photon survival over a distance t.

Equation 2.8 paints an incomplete picture, however, as it assumes that any photon absorbed is lost. This is not true in a wavelength-shifting material, as any photon that is absorbed has a chance to be re-emitted and continue travelling through the medium. This re-emitted photon may strike the PMT or, while less likely due to the Stokes shift, may be re-absorbed once again (which again leads to a chance of being re-emitted). Consider a photon that travels its mean free path of λ before being absorbed. The photon has a chance P_{RE} of being re-emitted and has a chance of P_{TIR} of remaining captured in the plate. It then travels its mean free path before being absorbed, and the process repeats for N emissions, until it reaches the PMT. From this process, a more accurate accounting of the probability of surviving travel through the plate can be written:

$$P(t) = e^{-t/\lambda_0} + (P_{TIR}P_{RE})^{N-1} e^{-(t-\lambda)/\lambda} \prod_{n=2}^{N-1} \left(1 - e^{-(t-(n-1)\lambda)/\lambda}\right) \tag{2.9}$$

Using Equation 2.3 and knowing that photons will be re-emitted isotropically allows P_{TIR} to be replaced with known constants:

$$P(t) = e^{-t/\lambda_0} + \left(P_{RE} \arcsin\left(\frac{n_2}{n_1}\right)/\pi\right)^{N-1} e^{-(t-\lambda)/\lambda} \prod_{n=2}^{N-1} \left(1 - e^{-(t-(n-1)\lambda)/\lambda}\right) \tag{2.10}$$

After each re-emission the photon will have a longer wavelength due to the Stokes Shift, and thus the mean free path will change with each re-emission, requiring a recalculation of λ. Additionally, Equation 2.10 does not consider the isotropic re-emission of the photon in the XY plane. That is, in a real system, the photon will be re-emitted in a different direction than its initial direction of travel. This will result in a different travel length, t, before reaching a PMT. However, due to the relatively low prevalence of photons being absorbed, re-emitted, and still retained in the plate, this assumption is adequate for this analysis.

The second method by which a photon may be destroyed is via a loss at a reflective surface. No material is perfectly reflective; there will always be some chance for a photon reaching the boundary of the wavelength-shifting plate to be absorbed in the reflector material rather than being reflected. Alternatively, if the reflector is not perfectly specular, there is a chance for the photon to reflect diffusely off of the

reflector and no longer be trapped in the plate by TIR. The probability of a photon surviving this mechanism is:

$$P(n_x, n_y) = \rho^{(n_x+n_y)} \tag{2.11}$$

where ρ is the reflectivity of the boundary material, which should, in this case, be taken to only include specular reflection.

Equations 2.10 and 2.11 can be combined to find the total probability of a photon surviving until it reaches the plate-PMT interface:

$$P(t, n_x, n_y) = e^{-t/\lambda_0} + \left(P_{RE} \arcsin\left(\frac{n_2}{n_1}\right)/\pi\right)^{N-1} e^{-(t-\lambda)/\lambda} \prod_{n=2}^{N-1} \left(1 - e^{-(t-(n-1)\lambda)/\lambda}\right) + \rho^{(n_x+n_y)} \tag{2.12}$$

Equation 2.12 can be used to calculate the probability that a photon, generated at any point in the plate traveling in any direction, will survive until it reaches the PMT-plate interface. It is now of interest to use this equation to calculate the average of the probability that a photon generated at a point will reach the PMT-plate interface across all possible directions of travel. This can be done by performing the calculations in Equations 2.5 and 2.12 for the full set of starting directions of travel $\boldsymbol{D} = [\cos(\theta), \sin(\theta)]$ where $\theta = [0, 2\pi)$. The average can then be computed by:

$$P_{avg} = \frac{1}{2\pi} * \int_0^{2\pi} P(\cos(\theta), \sin(\theta)) d\theta \tag{2.13}$$

To calculate the average collection efficiency across a number of points on the plate contained in the set $x = [a_x, b_x]$, $y = [a_y, b_y]$, additional integrals can be computed:

$$P_{avg} = \frac{1}{b_x - a_x} \frac{1}{b_y - a_y} \frac{1}{2\pi} \int_{a_x}^{b_x} \int_{a_y}^{b_y} \int_0^{2\pi} P(x, y, \cos(\theta), \sin(\theta)) d\theta dy dx \tag{2.14}$$

2.5 Results

It is not feasible to integrate Equation 2.14 analytically; instead a program was written in Python to solve it numerically. This was done by solving Equation 2.10 at regularly spaced points across the plate's surface, for photons generated at discrete initial angles between 0 and 2π. The results at each point were averaged across all angles, yielding the average survival probability of a photon generated isotropically at that point. These calculations were performed for a 15.1 in. (383.54 mm) by 11.52 in. (292.61 mm) rectangular plate, with a 9.5 in. (241.3 mm) diameter hole offset from the center point of the plate by 1.05 in. (26.67 mm) in its longer dimension. These plate dimensions were consistent with the true dimensions of the wavelength-shifting plates

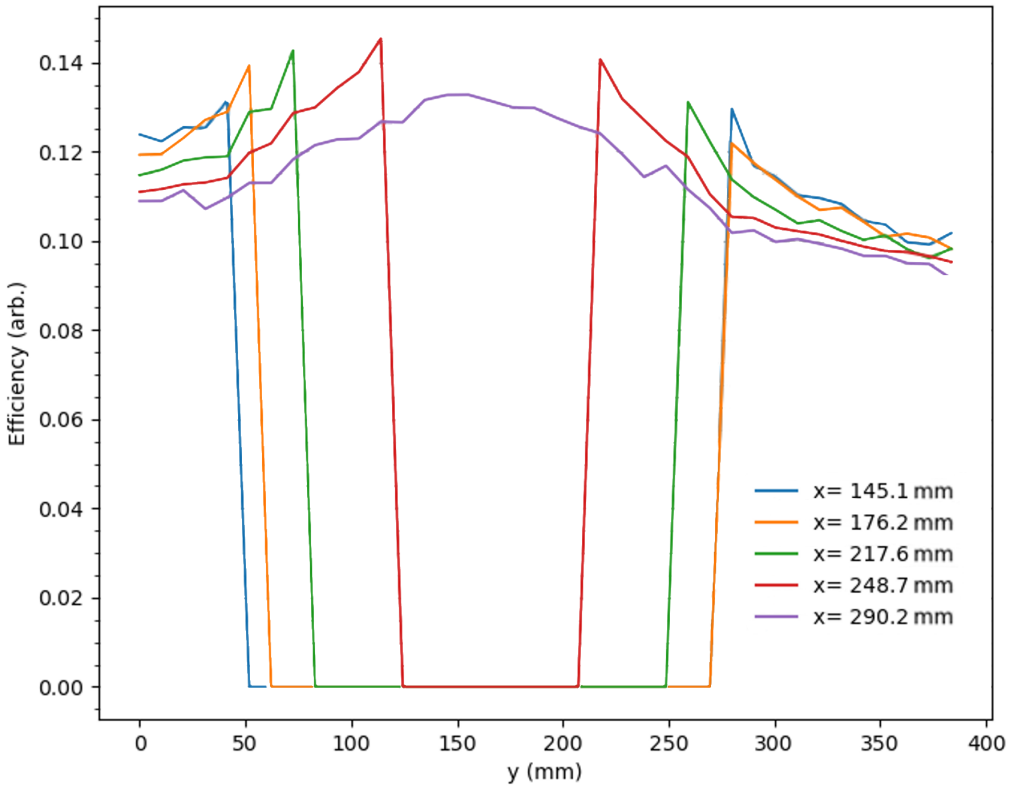

Figure 2.10 The results of the analytical model calculated across various points on the plate's surface. Points that would fall on the PMT bulb itself are excluded. The y-axis is arbitrary and can be adjusted by a scaling parameter.

used in the experiments described in Chapters 3 and 4 of this work. The results of the calculations for a plate of these dimensions can be seen in Figure 2.10.

Several factors have not yet been considered as part of the analytical model. Neither the efficiency of light being trapped in the plate by TIR nor the efficiency of the light leaving the plate and reaching the PMT bulb are represented in the model, though these both can be analytically predicted, as shown above. The efficiency of the PMT converting the light into an electronic signal, as determined by the quantum efficiency of the PMT and the emission spectrum of the wavelength-shifting plastic, is likewise a known factor that has not yet been included in the calculations. Other factors, such as light that reflects off of the PMT bulb without reaching the photocathode, are not easily accounted for analytically. In practice, as none of these factors should affect the shape of the light collection efficiency curves, they were aggregated into a single scaling parameter, S_e, which was then applied to all points equally across the plate.

Several expectations for the behavior of the wavelength-shifting plate can be drawn from the results of the analytical model. First, it can be expected that the efficiency of light collection does not vary widely across the plate's surface, except for very near the plate-PMT interface. Between 275 mm and 375 mm in Figure 2.10, for example, the light collection efficiency only drops from around 10.5% to 9.5% across all points measured. Second, some asymmetric response can be expected due to the rectangular shape of the plate and the off-center location of the hole. The points calculated between 100 mm and 125 mm, for example appear to be consistently higher than their counterparts on the opposite side of the PMT. This is due to the longer path lengths needed to be travelled by photons generated on the "long" side of the plate compared to those generated on the "short" side, resulting in a reduced survival probability.

There are shortcomings to this analytical model, however. First, the aforementioned scaling factor makes it difficult to predict the absolute light collection improvement that the plate can be expected to provide. Second, the model assumes that there are only three ways for a photon to leave the system: re-absorption, loss at a reflective boundary, or reaching the PMT. In reality, there will be other ways for a photons to leave the system, such as escaping from the plate due to surface roughness, scattering reactions within the plastic, or diffuse reflection from the outer boundaries, which are not accounted for in this model. These effects may affect the overall shape and scale of the light collection behavior of the wavelength-shifting plate and are difficult to account for analytically.

Despite these shortcomings, however, the analytical model provides valuable insight into the expected behavior of the plate. The model demonstrates that reabsorption of the plastic and loss at the reflective boundaries are expected to be the most significant factors of photon loss in the systems and predicts several features of the plate's overall light collection behavior. This information can then be used when creating a Monte Carlo simulation of the wavelength-shifting plate that does

not suffer from the same drawbacks as the analytical model.

2.6 Generating a Monte Carlo Model

To test the benefits and drawbacks of including wavelength-shifting plastics in a large-scale water-based detector, the simulation framework RAT-PAC was utilized. RAT-PAC is a wrapper for Geant4 well suited for simulating such detectors [59–61]. RAT-PAC uses Monte Carlo techniques to model the lifetime of individual particles, such as positrons, electrons, and photons, as they travel through and interact in the detector. RAT-PAC also models PMT behaviors and can convert photons that strike a PMT's photocathode into charge, measured as photoelectrons, distributed according to a user-specified PMT timing profile. Analysis for the Monte Carlo simulations was done using C++ ROOT [62].

The WATCHMAN Collaboration has already refined the RAT-PAC simulation framework for modeling large-volume water-Cherenkov antineutrino detectors. This allowed the wavelength-shifting plates to be incorporated into an already validated framework, so that only the behavior of the plates within the framework need be experimentally validated. The material and optical properties for the wavelength-shifting plates were provided by the manufacturer, Eljen Technology, to most closely model the plastic in the code before the behavior of the plates can be validated experimentally [63]. These properties included values for the index of refraction across wavelengths, the absorption and re-emission spectra, the fluor decay time, and the wavelength-shifter's quantum efficiency (defined as the percentage of absorbed light that is re-emitted). The Monte Carlo model will be presented in Chapters 3 and 5.

Before the behavior of wavelength-shifting plates in a large-scale water Cherenkov detector can be explored, the properties and behavior of such plates in the simulation framework must be experimentally validated. To do this, two experiments were carried out. First, the plate was scanned using a UV LED in a dark box in order to calculate the light collection efficiency of a single wavelength-shifting plate across its surface. Then, four plates were implemented into a one-ton water Cherenkov detector to test their behavior in a real detector environment when exposed to Cherenkov light generated by cosmogenic muons. These two experiments will be the subjects of the next two chapters.

Chapter Three

Scans of the Wavelength-Shifting Plate in Air

3.1 Overview

The light collection properties of a wavelength-shifting plate must be experimentally determined in order to develop and validate any Monte Carlo model including such plates. Therefore, the response of a PMT-Plate unit was experimentally probed utilizing the light from a collimated LED system. These results were then used to develop the Monte Carlo model used to predict plate behavior in a kiloton-scale water-Cherenkov detector experiment.[1]

3.2 Experimental Design

The testing rig developed for this experiment can be seen in Figures 3.1 and 3.2. A computer aided drawing of the rig, showing how the wavelength-shifting plate and PMT are coupled, is given in Figure 3.3. A Hamamatsu R7081 253 mm diameter PMT is suspended in the air [65]. This PMT was chosen as it is designed for use in large volume water-Cherenkov detectors, has a large surface area, and is currently the main candidate for use in the detector designs being considered by the WATCHMAN collaboration. The high voltage of the PMT was applied using a CAEN DT830X series desktop high voltage unit. The output of the PMT was sent to a CAEN V1720 series digitizer to be converted directly into a digital pulse. The PMT is coupled onto an Eljen Technology EJ-286 blue-emitting wavelength-shifting plastic plate. The PMT/plate coupling is provided by gravity with intimate points of contact along the PMT-plate interface. The experiment was performed with and without optical grease (EJ-550) to improve the coupling between the plate and the PMT [66]. While optical grease would not be able to be used in a real neutrino detector application (as the PMT and plate will be submerged under water), experimental measurements with

[1] This chapter is largely based on work previously published by the author [64].

the optical grease were helpful to tune the behavior of the PMT-plate interface in simulations.

The plate, as depicted in Figure 3.3, is 15.1 in. (383.54 mm) in length and 11.52 in. (292.61 mm) in width, with a hole offset from the center point of the plate by 1.05 in. (26.67 mm) in its longer dimension. The wall of the hole is angled at 45 degrees, its smaller diameter being 8.5 in. (215.9 mm) and its larger diameter being 9.5 in. (241.3 mm). The plate is 0.5 in. (12.7 mm) thick. The rectangular, asymmetric shape of the wavelength-shifting plate was chosen to allow for its inclusion in a one-ton water-Cherenkov detector described in the subsequent chapter.

A collimated LED, also depicted in Figure 3.3 was placed on a movable rail system 2.5 in. (63.5 mm) beneath the surface of the wavelength-shifting plate. It was placed at this distance to ensure that the collimator did not collide with the bulb of the PMT during testing. The LED produced a spot with a diameter of 10 mm at the plate's surface, and measurements were taken at 40 mm intervals along the short side of the plate and 10 mm intervals along the long side of the plate. The LED housing permits for the LED to be changed between experiments, allowing data to be taken with both a 365 nm UV LED and a 569 nm green LED. This green LED was chosen as a control, since green light is largely not absorbed in the wavelength-shifting plate. The entire rig was constructed in a dark box painted with non-reflective black paint to minimize the amount of reflected light from the box's surfaces.

The collection efficiency of a wavelength-shifting plate can be affected by the presence and the choice of material used as a reflector around the outer edge of the plate [67]. Light that is retained in the plate by TIR can still escape through the perpendicular surfaces at the edges of the plate, so placing a reflector along those surfaces to redirect the light back towards the PMT is beneficial. In this experiment, wavelength-shifting plates were tested with both no reflector applied and with an aluminized mylar tape applied to the plate edges. The tape is highly reflective (with a reflectivity of around 95%) and specular, as seen by the reflected beam from a handheld laser pointer in Figure 3.4.

3.3 Results

The data collected in the experiment allows one to measure the change in light collection efficiency across different points on the plate. Graphs of the light collection efficiency over the surface of the plate, both with and without a reflector, are provided in Figure 3.5. Neither of these measurements used optical grease to couple the plate to the PMT. Note that this is not the absolute light collection efficiency of the plate, but instead the efficiency relative to that at the center of the PMT bulb. The light collection efficiency, except very near the PMT-plate interface where LED spot size begins to have a significant effect, is roughly constant over the plate's surface. This is an encouraging result for the scalability of such a plate to cover larger surface areas, as the light collection efficiency should not drop off rapidly as the plate becomes

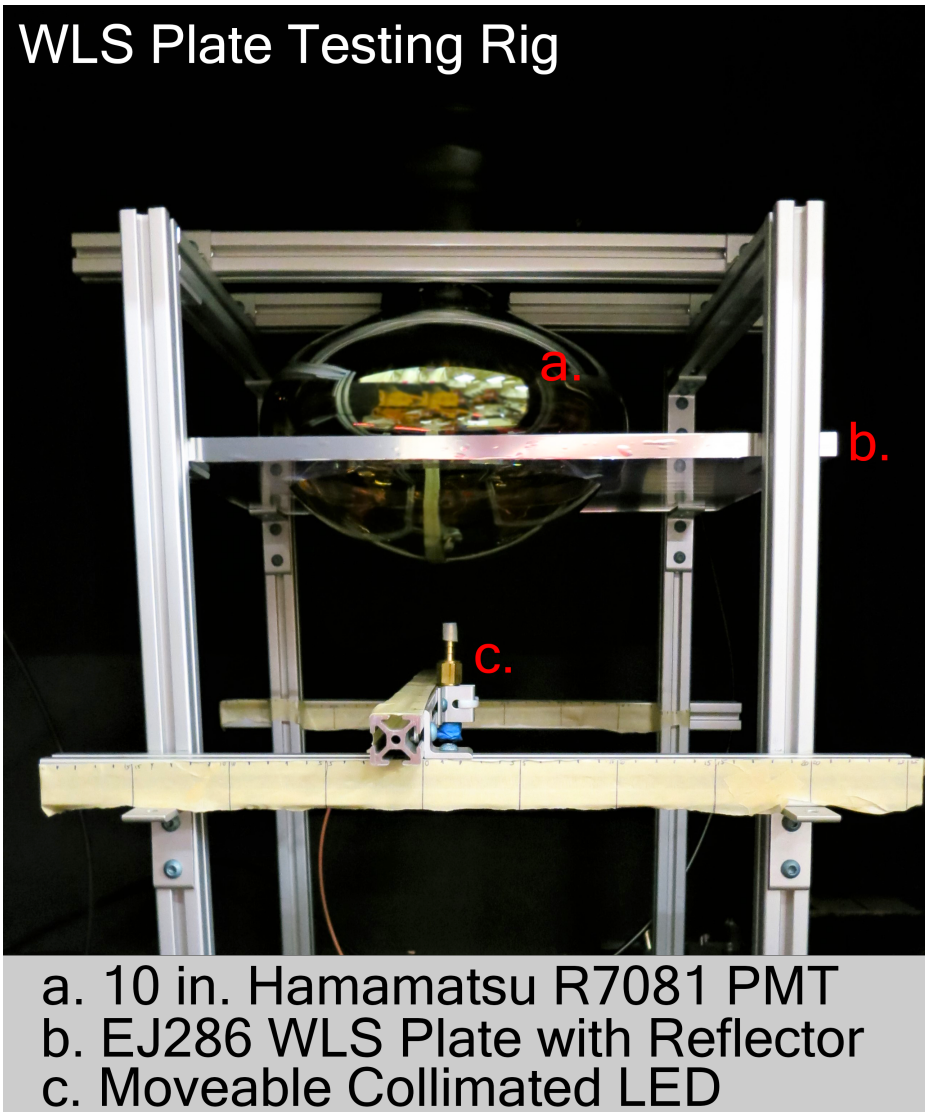

Figure 3.1 The light collection efficiency testing rig emplaced in a dark box, as seen from the side. The PMT is coupled by gravity to the wavelength-shifting plate, which is wrapped in an aluminized mylar tape reflector. The plate is an asymmetric rectangle to accommodate its use in a one-ton detector experiment.

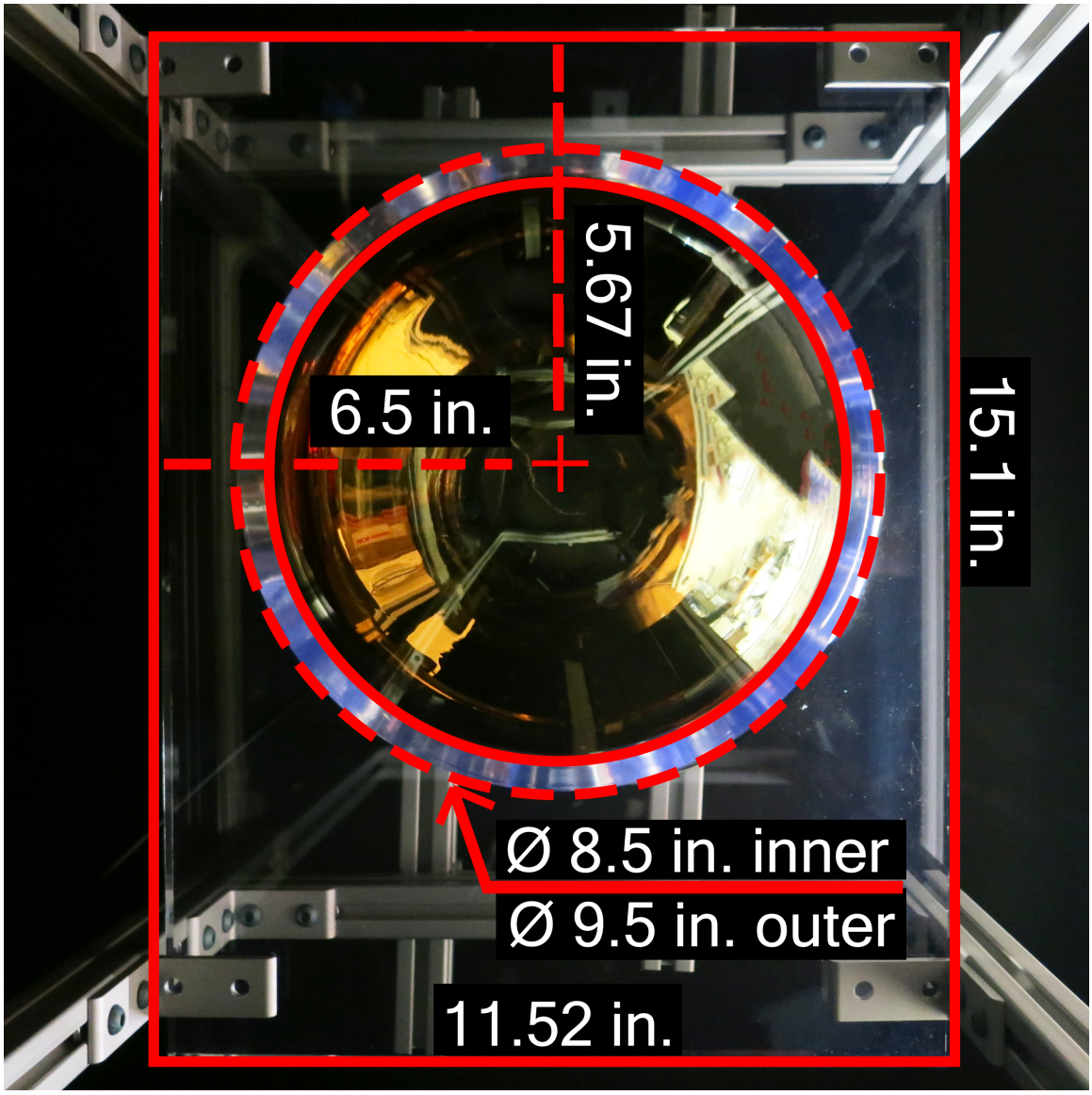

Figure 3.2 The light collection efficiency testing rig as seen from the bottom. The off-center hole in which the PMT is placed is clearly seen.

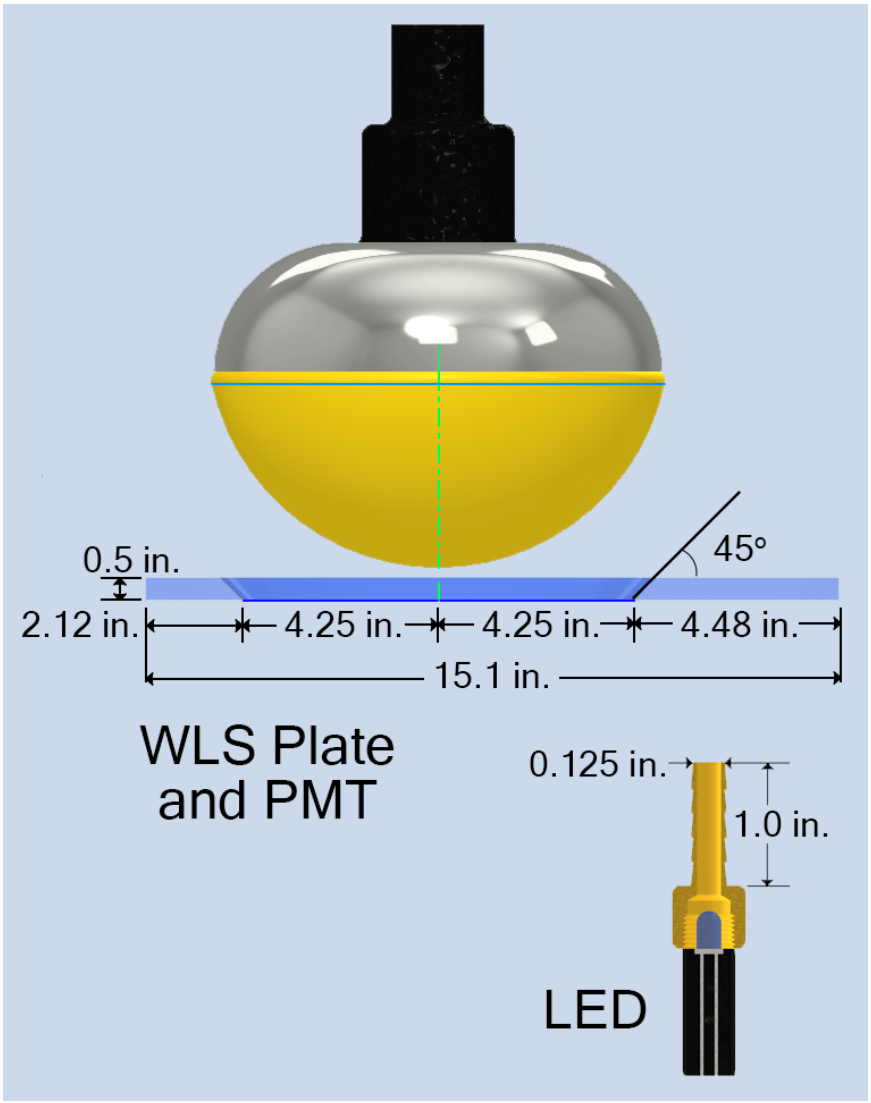

Figure 3.3 A computer aided drawing of the wavelength-shifting plate and LED collimator. The edges of the hole in the wavelength-shifting plate are beveled so that gravity will couple the PMT to the plate. The collimator produces a spot with a diameter of 10 mm on the plate's surface.

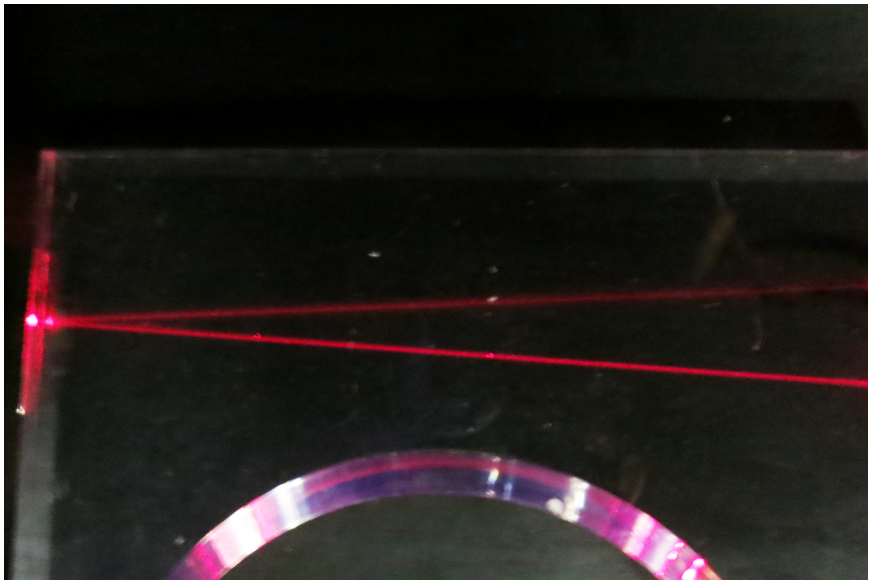

Figure 3.4 The reflectivity and specularity of the aluminized mylar tape reflector, demonstrated by reflecting the beam from a laser pointer off of the edge of a wavelength-shifting plate.

larger.

An asymmetry in the light collection efficiency between the two sides of the wavelength-shifting plate was observed; in Figure 3.5, the negative y direction produced a higher collection efficiency than those in the positive y direction. This asymmetry was likely driven by the shorter distance between the outer edge of the plate and the PMT in the negative y direction. This means that photons emitted on the narrower side of the plate have shorter average path lengths to reach the PMT than those emitted in the longer side of the plate. This, in turn, means that fewer photons are lost to re-absorption in the plastic. Once reabsorbed, photons can be either lost to non-radiative processes or re-emitted at a direction not amenable to capture in the plate by TIR. A similar, but smaller, asymmetry was observed in the simulation results. The plate was also simulated using very long photon attenuation lengths, which caused the asymmetric response to disappear. This indicates that re-absorption due to longer photon path lengths in the plastic is likely the driving cause of the asymmetric response. A symmetric plate was also simulated, and the asymmetry again disappeared.

A comparison of light collected with and without the wavelength-shifting plate is presented in Table 3.1, along with the results from the Monte Carlo simulations that will be discussed in the next section. The increase in light collection is defined here as the fractional increase (in percent) in the number of photoelectrons generated in an event between a PMT with a wavelength-shifting plate and a PMT without. This is given in Equation 3.1, where C is the light collection increase and L is the

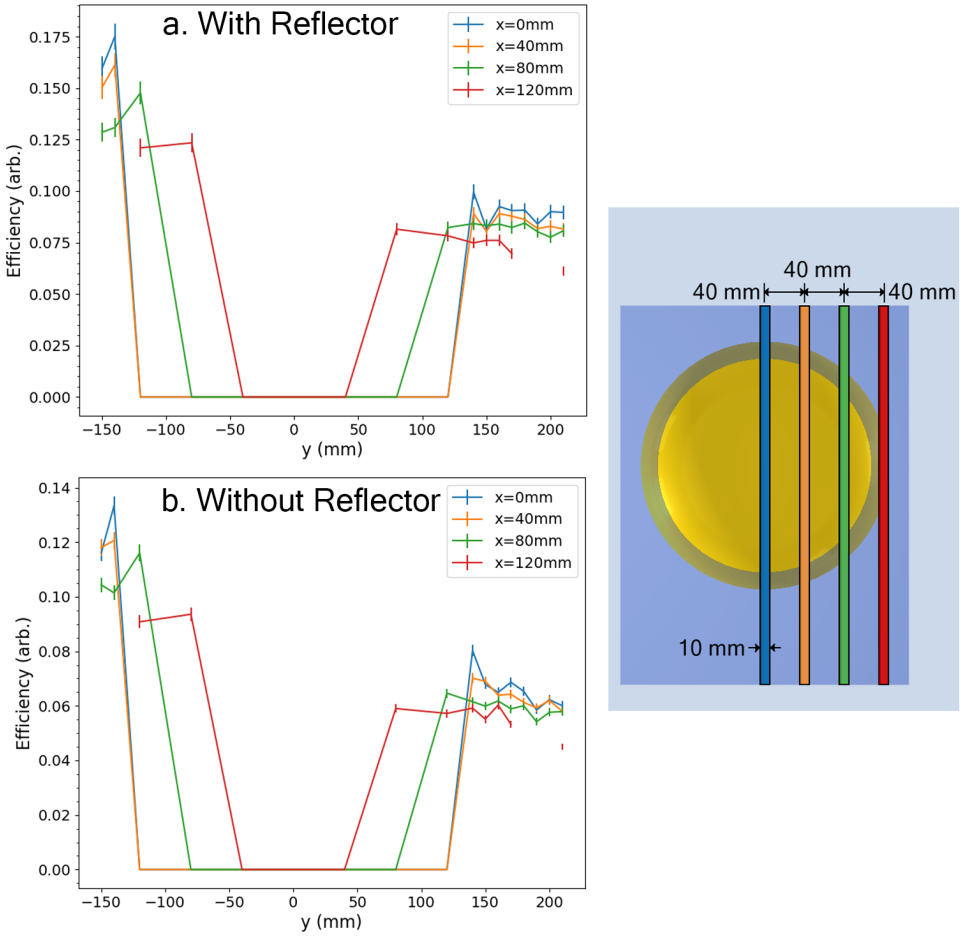

Figure 3.5 Various cuts lengthwise across the plate which show the variation in the light collection efficiency over the surface of a wavelength-shifting plate with (a.) and without (b.) an aluminized tape reflector. Measurements on the bulb of the PMT itself are excluded, along with measurements that were blocked by the structural brackets. The colors of each data set can be seen projected onto a bottom view of the PMT plate system in the image inset to the right. In both cases, there is a marked asymmetry between the positive and the negative points due to the asymmetric shape of the wavelength-shifting plate used. Additionally, both cases demonstrate that light collection is largely constant across a majority of the plate's surface, from approximately 150 to 220 mm.

Table 3.1 The light collection increase of a wavelength-shifting plate measured by the experimental setup and simulations. Experimental light increase is defined as the percent increase in the number of photons collected by the PMT when using a wavelength-shifting plate compared to a PMT not using a wavelength-shifting plate. The simulations are able to recreate the light collection increases seen by the experimental results. The calculated increases assume conditions of uniform irradiation of the plate and PMT.

Reflector	Light Increase	
	Experimental	Simulated
Yes	7.4 ± 0.7%	7.1 ± 0.2%
No	-0.08 ± 0.7%	-1.2 ± 0.2%
Yes & using Optical Grease	16.2 ± 0.7%	16.2 ± 0.2%

number of photoelectrons generated by the PMT. To calculate the light collection of the PMT without the wavelength-shifting plate, the green LED was used, as the plate is largely transparent to its light. This allows the green LED measurements to serve as a proxy for a measurement taken without the wavelength-shifting plate. The normalization to the response at the center of the PMT bulb corrects for the PMT's different quantum efficiencies at the two wavelengths.

$$C = \frac{L_{WLS} - L_{Bare}}{L_{Bare}} \tag{3.1}$$

It is notable in Table 3.1 that the wavelength-shifting plate without a reflector provides no statistically significant benefit over a bare PMT in this experimental setup. This is due to the lower overall light collection efficiency of a plate without a reflector, combined with a shadowing effect where light that would otherwise have struck the PMT surface is instead absorbed by the plate and directed away from the PMT. While this shadowing effect is present with a reflector as well, the overall light collection efficiency is much higher, reducing its impact. It is also notable that coupling the PMT to the wavelength-shifting plate with optical grease roughly doubles the light collection increase compared to air. This is consistent with the simple optics calculations performed in Chapter 2 that show that, in air, roughly half of the collected light will be rejected from the plate-PMT interface due to TIR.

3.4 Comparison to Simulations

The plate and PMT used were recreated in the RAT-PAC simulation framework according to manufacturer specifications. The properties of the plate, such as the roughness of the plate's surfaces, were then tuned to bring its behavior in the simulations into better agreement with its behavior in the experimental setup. A comparison

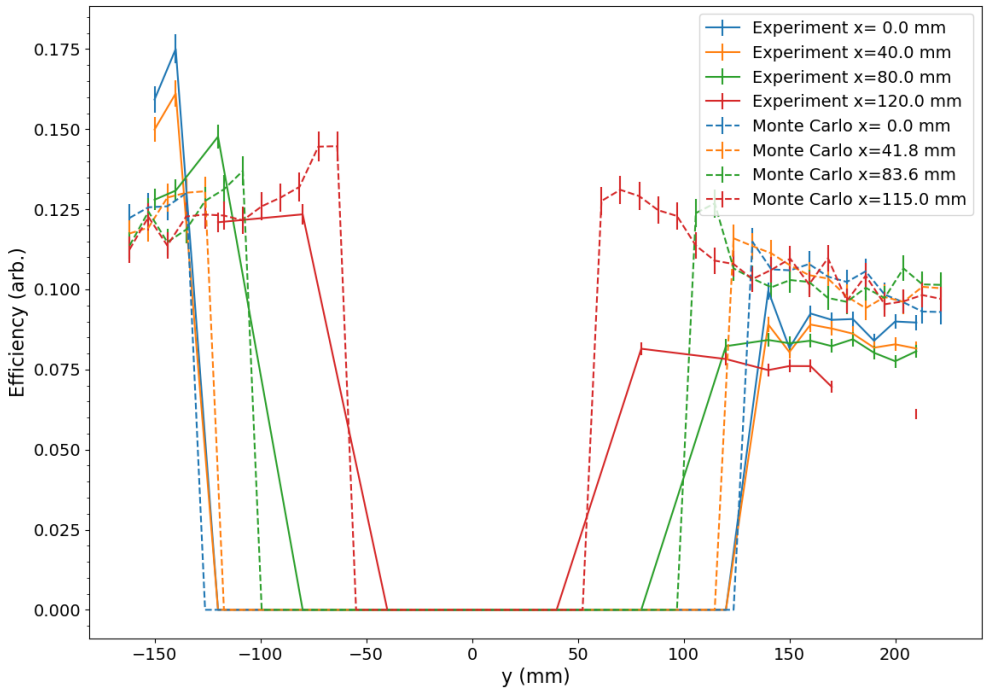

Figure 3.6 The light collection efficiency from both the experimental and simulation results across the plate's surface. Both the experimental and simulated results are largely consistent, though the simulations do not recreate the asymmetry to the extent seen in the experimental results.

between the experimentally measured light collection efficiency and a simulated efficiency across a plate's surface is given in Figure 3.6. It can be seen that the general behavior of the light across the wavelength-shifting plate is represented in the simulation, and some amount of asymmetry is also observed, though not to the same extent seen in the experimental results. The remaining difference between the experimental and simulated results likely lies in the behavior of light at the plate's surfaces, as it is governed by very complex processes that are difficult to recreate in the Monte Carlo simulation. A further discussion of this optical process and how it was handled in the Monte Carlo is given in the subsequent chapter. The overall increases in light collection can be calculated from simulation results, as shown in Table 3.1. The given uncertainties are statistical from the Monte Carlo simulation. The results are largely consistent between the experiment and the simulation for all three experiments.

The experimental and Monte Carlo results are also consistent with the analytical model presented in the previous chapter, as can be seen in Figure 3.7. As noted in the previous chapter, the analytical model contains a scaling parameter that was

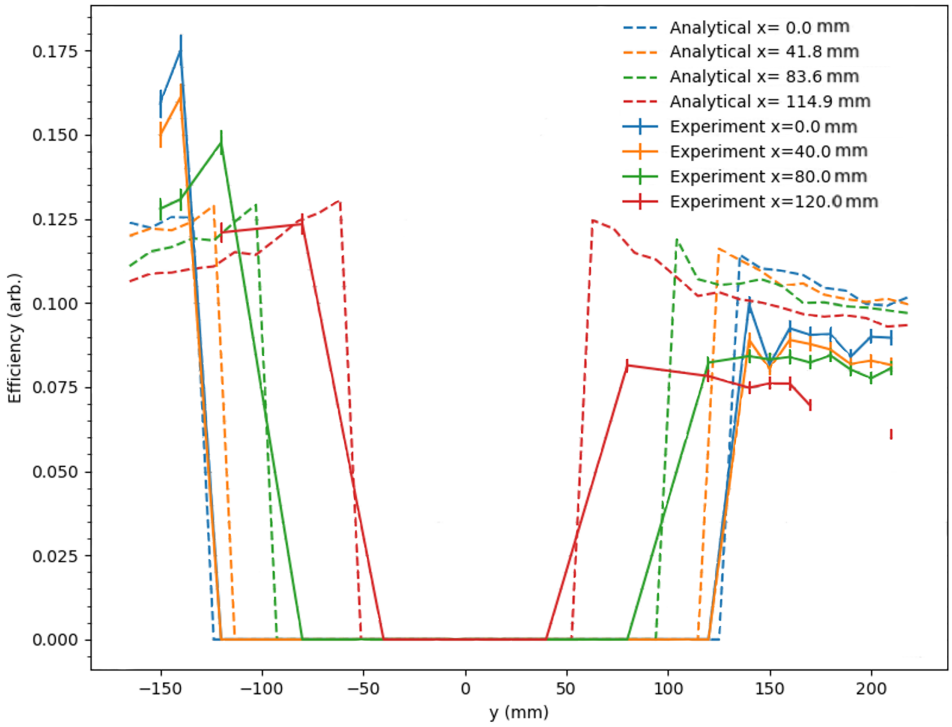

Figure 3.7 The light collection efficiency from both the experimental and analytical results from the previous chapter across the plate's surface. The analytical results agree well with the experimental data and Monte Carlo results..

set to allow for the best agreement with the experimental and Monte Carlo results. The shape of the analytical results compares favorably to both the experimental and Monte Carlo results, though, like the Monte Carlo results, it fails to recreate the extent of the asymmetry seen in the experimental results. The agreement of the analytical and experimental results indicates that photon re-absorption and loss at boundaries are likely the main drivers of the light collection behavior of the plates, as those two parameters determined the shape of the analytical results.

In a real detector the plates and PMTs will be submerged under water rather than suspended in air. The two media will behave differently due to their distinct indices of refraction leading to different reflection and refraction properties at the plate surfaces. Simulations of a 15.1 in. by 11.52 in. plate identical to the one tested experimentally here were conducted with the surrounding air changed to water. The simulations resulted in a light collection increase in water of $6.7 \pm 0.2\%$, a small reduction relative to the same plate in air.

Finally, it is of interest to test, via simulations, the increase in total light collection of a larger plate with a more regular, square geometry, such as one that may be included in a large-volume water-Cherenkov antineutrino detector. The simulations

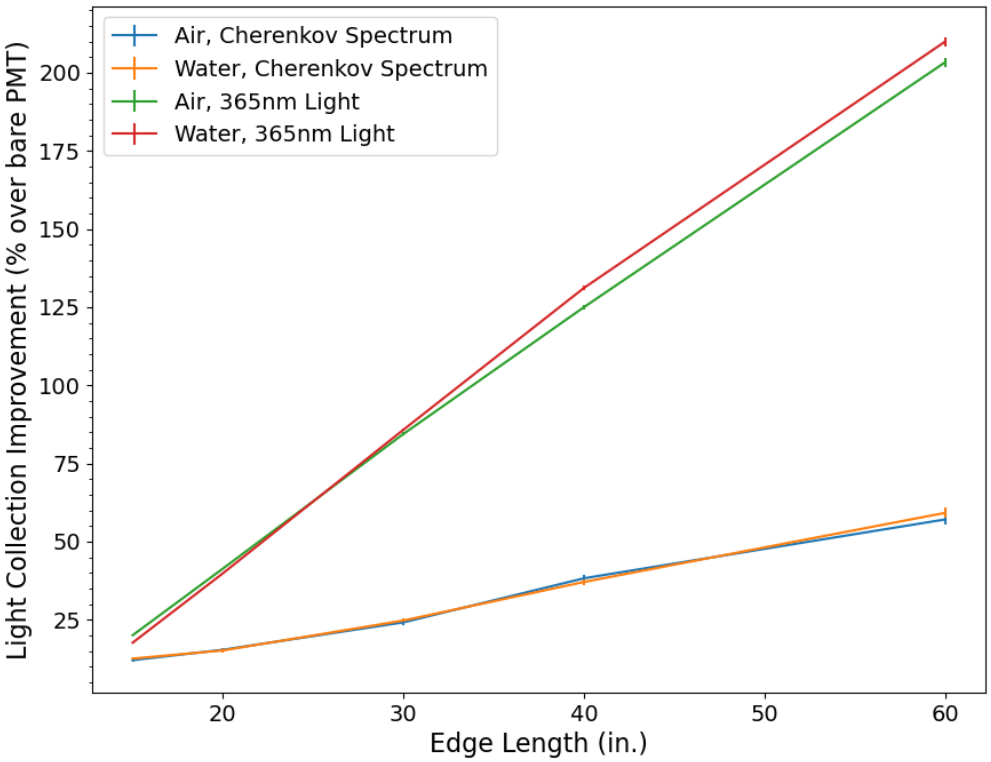

Figure 3.8 Simulation results for the light collection increases afforded by various square plate sizes in air and water. The relationship between edge size and light collection improvement is seen to be linear. The expected ability of the wavelength-shifting plate to collect Cherenkov spectrum light is seen to be significantly degraded compared to its ability to collect monochromatic 365 nm light.

were run using both uniform 365 nm light, such as that produced by the LED in the experimental setup, and the diffuse Cherenkov spectrum produced in a real detector. The results, for both plates in air and in water, are given in Figure 3.8. It can be seen that over a wide range of wavelength-shifting plate sizes, the light collection increase scales approximately linearly with plate edge length, and can be described empirically by Equations 3.2-3.5, where x is the side length of a square plate and C is the improvement in light collection afforded by the wavelength-shifting plate. The equations should only be taken to be valid under the limited range of plate sizes tested here and not extrapolated to radically different plate sizes, as they fail to accurately represent the behavior of very small plates where x approaches zero, or very large plates, which begin to behave non-linearly. The linear relationship observed can be interpreted in the following way - while the total light incident on the plate's surface increases as roughly x^2, the absolute collection efficiency of the plate falls off as $1/x$. These results are largely consistent with those found by the IMB-3 detector [28].

$$\text{For Air, Cherenkov Spectrum: } C = (1.00 \pm 0.03)x - (3.07 \pm 0.75) \tag{3.2}$$

$$\text{For Water, Cherenkov Spectrum: } C = (1.00 \pm 0.03)x - (3.56 \pm 0.73) \tag{3.3}$$

$$\text{For Air, 365 nm Light: } C = (4.18 \pm 0.02)x - (42.44 \pm 0.39) \tag{3.4}$$

$$\text{For Water, 365 nm Light: } C = (4.45 \pm 0.03)x - (48.91 \pm 0.73) \tag{3.5}$$

It should be noted that the overall improvement in light collection is poorer when considering Cherenkov spectrum light compared to monochromatic 365 nm light, with Cherenkov light resulting in a smaller improvement relative to the 365 nm source (16% versus 40% for a 20 inch plate in water, for example). This is because the wavelength-shifting plate is transparent to many of the longer wavelengths in the Cherenkov spectrum, rendering the plate ineffective at collecting this light. Additionally, the wavelength-shifting plate is most effective at collecting UV light with short wavelengths. However, this light (particularly light with a wavelength of less than 300 nm) is unlikely to reach the plate at all, as it has a very short attenuation length in water. This effect biases the spectrum to which the wavelength-shifting plate is exposed towards longer-wavelength light, which the plate is less effective at collecting. This further drives the relative reduction of efficiency of a plate exposed to Cherenkov spectrum light compared to one exposed to monochromatic light.

One can see broad consistency between the results for both the simulations performed in air and in water. It is possible that this consistency is due to two competing factors that change with the medium, as described in Chapter 2. First, more light will escape from the plate's surfaces because the indices of refraction between the plate and water are more similar than those of the plate and air, meaning that TIR is less effective at retaining light in the plate. Second, once light is captured by the plate, a greater fraction may be able to cross from the plate into the PMT itself, as, for the same reason, less light will be rejected from the boundary by TIR. The

results presented here indicate that these two countervailing effects roughly cancel each other.

The results presented in this work are partially consistent with previous results in the literature. In a similar test of a single plate and PMT system, Johnston calculates that a 20 inch circular wavelength-shifting plate of equivalent plastic exposed to a Cherenkov spectrum will produce a 13.1% increase in light collection compared to a bare PMT [67]. This is consistent with the expected light improvement of a square plate of equivalent surface area calculated here, which has an edge length of 17.8 inches and an expected light collection improvement of 14%. However, when simulating 27 inch square plates in a large water-Cherenkov detector, Johnston finds a higher light collection improvement of 31% for PMTs with wavelength-shifting plates compared to those without. This is less consistent with the findings here, which expects an improvement of only 23% for a 27 inch square plate exposed to a Cherenkov spectrum in water. Factors such as the degree of optical coupling between the plate and the PMT and the reflectivity of the reflector employed on the plate may drive this difference. The PMTs in Johnston's simulations were also assumed to have a uniform collection efficiency across the bulb, while the efficiency of the PMTs simulated in this work was reduced on the outer edges of the bulb to better match real PMT performance. This difference in simulated PMT behavior may also contribute to the observed difference in light collection.

With the RAT-PAC simulations now able to accurately model the behavior of a single wavelength-shifting plates in air, it was next of interest to validate the behavior of the wavelength-shifting plates in a real detector environment: implementing four wavelength-shifting plates into a one-ton water-Cherenkov detector and experimentally validating their response against Cherenkov-spectrum light generated by cosmogenic muons. The results of this experiment and matching simulations are presented in the next chapter.

Chapter Four

Performance of Wavelength-shifting Plates in a Small-Scale Detector

4.1 Overview

The previous chapter has explored the light collection of a wavelength-shifting plate in air using quasi-monochromatic light from an LED. As shown through the simulations, wavelength-shifting plate response to Cherenkov spectrum light in water is expected to differ, and it is these conditions that are most relevant for water-Cherenkov detectors. Additionally, light that is re-emitted in one wavelength-shifting plate may escape that plate and strike a different PMT in the detector. This may have a significant effect on one's ability to reconstruct events in a large-scale water-Cherenkov detector, and must be studied experimentally. To test both of these effects in a real detector environment, a one-ton water-Cherenkov detector test-bed was developed, the results of which were used to further validate the simulations.

4.2 Design of the Small-Scale Detector

A one-ton water Cherenkov detector previously used as a neutron well counter was used to measure the effects that wavelength-shifting plates have on the light collection of PMTs in water [68]. The experiment proceeded in two stages: first, as a control, with the one-ton detector in its default configuration (that is, without wavelength-shifting plates), and, second, with wavelength-shifting plates coupled to four of the detector's eight PMTs. The configuration of the detector with wavelength-shifting plates can be seen in Figures 4.1 and 4.2. The PMTs in "center" positions are affixed to wavelength-shifting plates, while those in "corner" positions remain bare. In the control detector configuration, all eight PMTs remain bare. The PMT response was tested both with the output of a 365 nm UV LED and Cherenkov light from cosmogenic muons passing through the detector, tagged by a muon hodoscope affixed to the detector's exterior.

The muon hodoscope consisted of two 5 inch by 5 inch by 0.5 inch EJ200 scin-

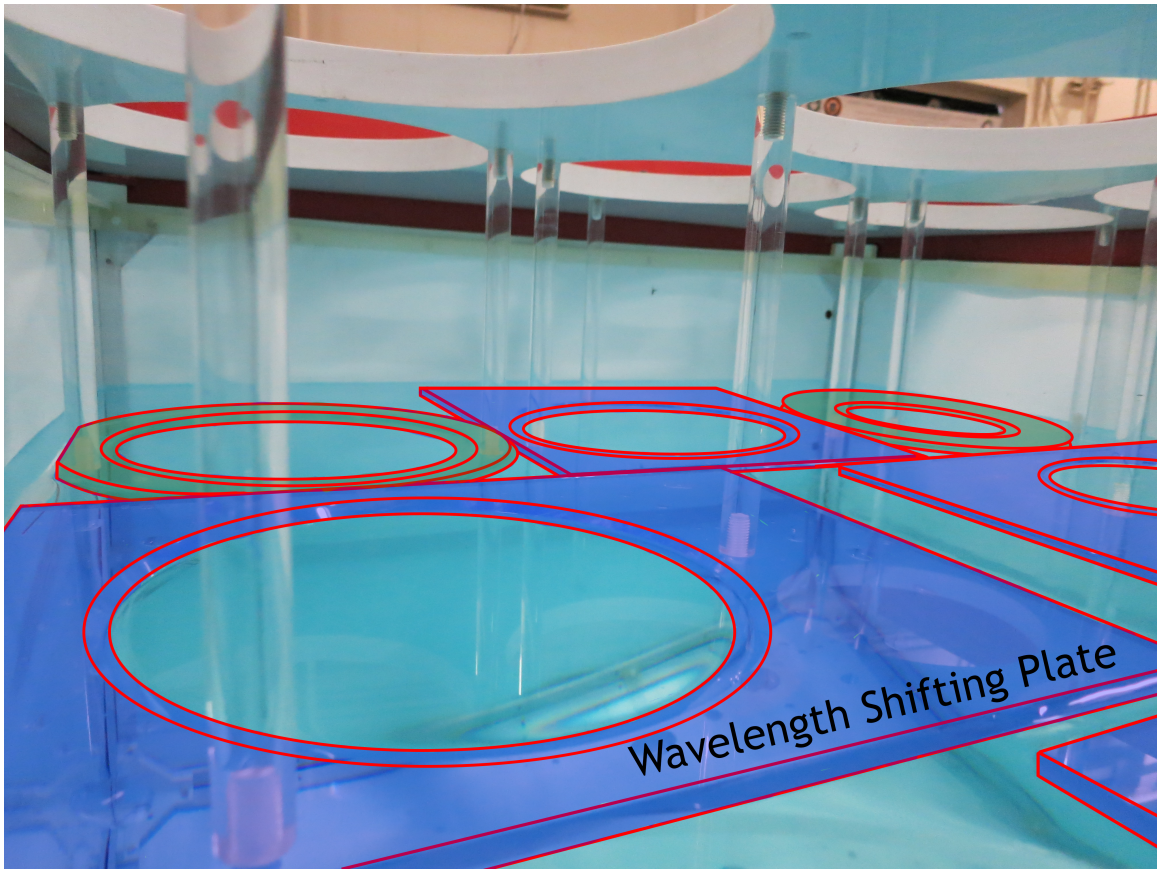

Figure 4.1 The inside of the one-ton detector with the wavelength-shifting plates (blue) and non-wavelength-shifting acrylic holders (green) falsely colored for emphasis. Not visible are two additional acrylic holders in the corners behind the camera.

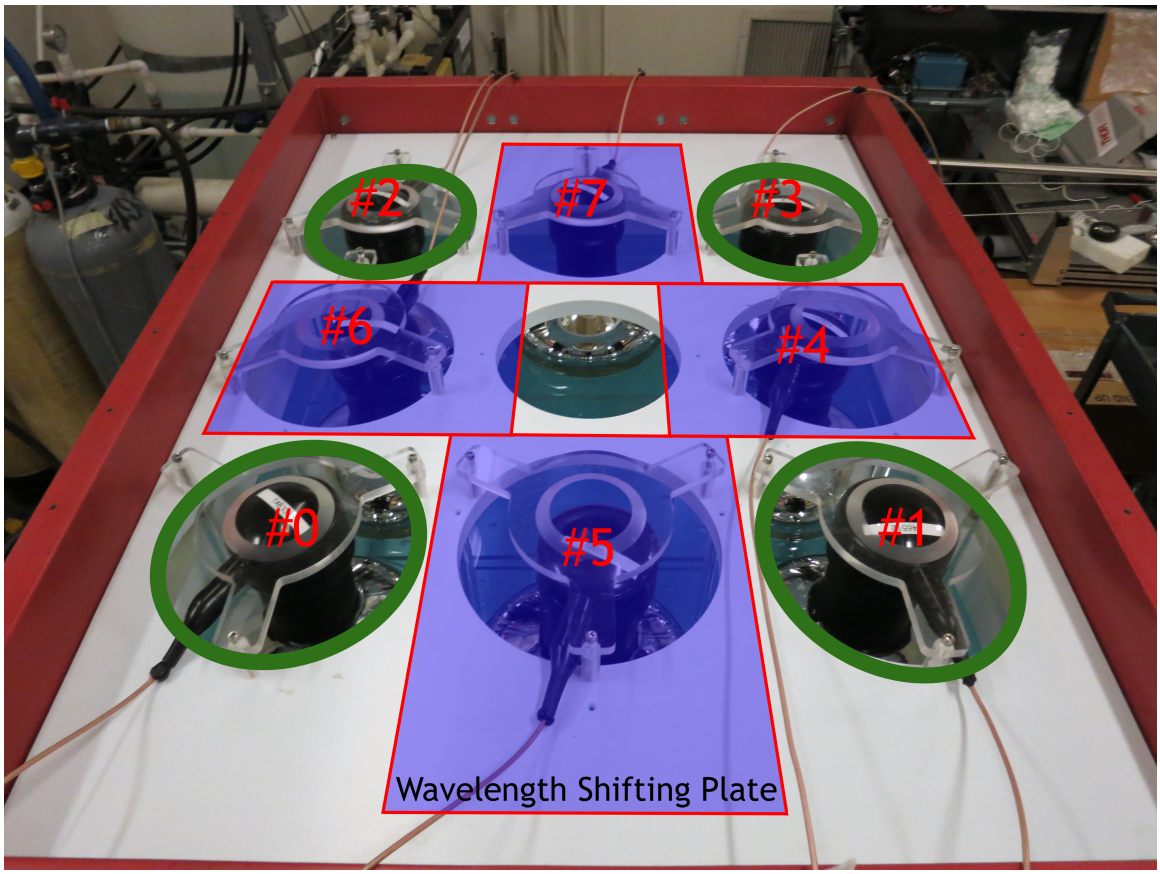

Figure 4.2 A top view of the one-ton detector with the locations of the wavelength-shifting plates highlighted in blue. Each PMT is labeled with its corresponding PMT number.

Figure 4.3 The two scintillator paddles that form the muon hodoscope affixed to the outside of the detector. Muons that pass through both hodoscopes have similar path lengths through the detector and thus create similar amounts of Cherenkov light.

tillator paddles coupled to Hamamatsu H6410, 60 mm diameter flat-faced PMTs. Both paddles were affixed to the side of the detector, one on each side of a corner. The higher paddle was placed so its center was 32.5 inches above the bottom of the detector and 6 inches horizontally from the corner. The second, lower paddle was positioned so its center is 20.5 inches above the bottom of the detector and 7 inches from the corner. A depiction of the detector system is given in Figure 4.3. The outputs of the two paddles were fed into a NIM coincidence circuit that output a logic pulse when both PMTs create a large enough analog signal pulse. In practice, this meant that the logical pulse was created when a muon passed through both paddles – and, by extension, through the detector volume between them. This logic signal was then used as a trigger for the data acquisition system so the detector's response to muons of a consistent path length passing through the detector's corner was recorded. Because the muons are largely minimally ionizing particles, the amount of light they create in the water depends on their path length rather than their energy, allowing a consistent amount of light to be created between experiments. A block diagram of the system is given in Figure 4.4.

The PMTs used in the detector were Hamamatsu R7081 253 mm diameter PMTs [65], similar to those used for the previous measurements in air. For the configuration with wavelength-shifting plates, four of the PMTs were coupled onto Eljen Technology

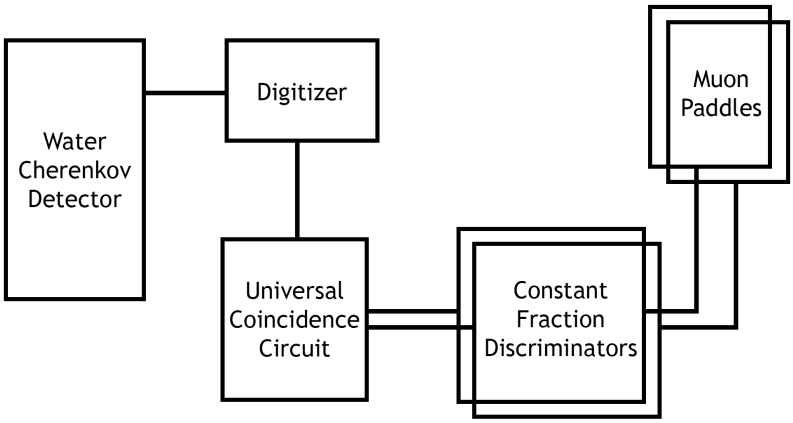

Figure 4.4 A block diagram of the coincidence circuit used to trigger the detector's data acquisition system. The system was designed to trigger when a cosmogenic muon passed through the corner of the detector, creating light in both muon paddles.

EJ-286 blue-emitting wavelength-shifting plastic plates, the same as those used for the previous measurements in the dark box. The high voltage of the PMTs were applied using a CAEN DT8033P series desktop high voltage unit. The output of the PMTs were sent to a CAEN V1720 series digitizer to be converted directly into a digital pulse. The PMTs were mechanically coupled to the plates with intimate points of contact along the interface and the water medium filling in interstitial points.

In order to interrogate the behavior of the PMTs under conditions of uniform irradiation, a 365 nm UV LED, identical to the one used for the dark box experiment, was used. The LED was diffused downwards by a thin layer of PTFE just below the water line in order to prevent stray reflections off of the water from striking the PMTs directly. The light was then reflected off of a diffuse Tyvek coating at the bottom of the tank, resulting in a nearly-uniform irradiation of the PMTs [69]. Each PMT, however, has a slightly different intrinsic light collection efficiency, as can be seen in Figure 4.5.

Because the LED output can vary considerably between tests based on factors like temperature and humidity, it is not suitable for a direct comparison of the light collection of the PMTs with and without wavelength-shifting plates. For this purpose, cosmogenic muons that pass through the detector, tagged by the previously described muon hodoscope, were used. As the light generated by minimum ionizing muons is dependant almost solely on the muons' path length through the water, these muons

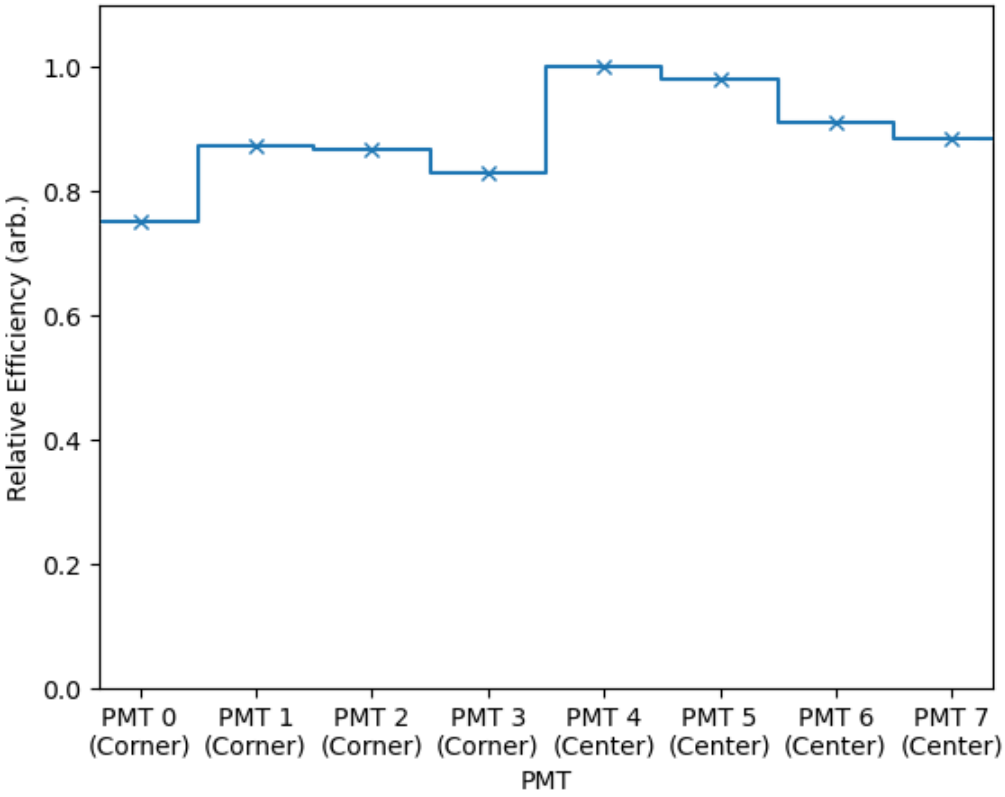

Figure 4.5 The normalized response of the eight PMTs in the one-ton detector when exposed to uniform 365 nm light. Note that despite the nominally uniform irradiation provded by the diffused LED, each PMT demonstrates a somewhat different efficiency.

Table 4.1 The relative light excess of the PMTs in center positions compared to those in corner positions, for both experimental results and simulations. Note that the light excess observed when wavelength-shifting plates are not present in the detector is largely driven by each PMT's relative light collection efficiency.

	Center PMT Light Excess	
	Without WLS Plates	With WLS Plates
Experimental	13.68 ± 0.06%	19.36 ± 0.02%
Simulated	14.65 ± 0.07%	15.49 ± 0.07%

produce consistent amounts of Cherenkov-spectrum light between experiments and allow for a comparison of PMTs with and without wavelength-shifting plates in real detector conditions.

4.3 Results

The outputs of PMTs with and without wavelength-shifting plates exposed to uniform irradiation by the 365nm LED indicates the relative improvement in light collection provided by the wavelength-shifting plates in a single experiment. This measurement was performed both when wavelength-shifting plates were absent and present in the detector, the results of which are recorded in Table 4.1. The values presented here are the number of photoelectrons collectively seen by the center PMTs, minus the number of photoelectrons seen by the corner PMTs, divided by the number of photoelectrons seen by the corner PMTs, as described by Equation 4.1. Since, in the configuration with wavelength-shifting plates, the "center" PMTs are coupled to the plates themselves while the "corner" PMTs are not, this is a measure of the efficiency of the plates to guide light to the PMTs they are coupled to. One observes a light excess in the center PMTs of the detector configuration without WLS plates because of the variation in efficiencies seen in Figure 4.5, where the corner PMTs are shown to have lower light collection efficiencies even when wavelength-shifting plates are not present in the detector.

$$\text{Light Excess} = \frac{N_{center} - N_{corner}}{N_{corner}} \tag{4.1}$$

By subtracting the measurements, it can be found that wavelength-shifting plates are responsible for guiding 5.68±0.06% more light to the PMTs to which they are coupled compared to those without wavelength-shifting plates in the same measurement.

This, however, is an incomplete view of the light collection behavior of the plates. First, light may leak from a plate and strike a different PMT, even one without a plate, which can be called "cross-talk". Thus, especially in a highly reflective environment like the one inside the one-ton detector, the inclusion of wavelength-shifting plates on

Table 4.2 The relative improvement in light collection in events tagged as cosmogenic muons passing through the detector in both the experiment and in simulations. PMTs in the "center" positions are coupled to wavelength-shifting plates when they are present in the detector. PMTs in the corner positions are always left bare but benefit from being adjacent to wavelength-shifting plates.

	PMT Position		
	Corner	Center	Total
Experimental	4.8 ± 0.8%	5.3 ± 0.7%	5.1 ± 0.6%
Simulated	2.7 ± 0.1%	6.5 ± 0.1%	4.7 ± 0.1%

only a few PMTs will still increase the light collection of all the PMTs. Second, as discussed in the previous chapter, wavelength-shifting plates are expected to be less effective at collecting Cherenkov light when compared to monochromatic light. This is because wavelength-shifting plates are less able to absorb the longer-wavelength components of the Cherenkov spectrum, and because the shortest-wavelength components of the spectrum are generally absorbed in the water before reaching the plates at all.

To investigate both the phenomenon of cross-talk and the behavior of the plates when exposed to Cherenkov light, muon interactions in the detector were used. A comparison of the light collection evidenced by PMTs in a detector with and without wavelength-shifting plates is given in Table 4.2. Due to a hardware failure in the data acquisition system, the experimental campaign was forced to conclude sooner than originally planned, resulting in the somewhat large uncertainties on the experimental data.

Comparing tests with and without wavelength-shifting plates in the detector finds a light collection improvement of 5.3±0.7% for the center-position PMTs that are coupled to wavelength-shifting plates in the experiment. As expected, this is somewhat reduced from the $7.4 \pm 0.7\%$ improvement measured using the 365 nm LED in a dark box. The comparison demonstrates a light collection improvement of $4.8 \pm 0.8\%$ for the corner-position PMTs that are never coupled to a wavelength-shifting plate. This indicates that a significant amount of light that is re-emitted in a wavelength-shifting plate will not be captured by TIR or will subsequently escape and will eventually strike a different PMT. This experiment indicates that the amount of light collected by these adjacent PMTs may even be the same order of magnitude to the amount of light seen by the PMT actually coupled to the wavelength-shifting plate.

4.4 Validation of Simulations

The experimental setup was created in the same Geant4-based Monte Carlo RAT-PAC framework as the previous experiment in air. The results of the simulation are also provided in Table 4.2 and a comparison of the experimental and the simulated results are shown in Figure 4.6. Good agreement can be seen between the experimental and simulated results. In the simulations, the performance of the PMTs directly coupled to the wavelength-shifting plates is slightly overestimated while the performance of the PMTs adjacent to, but not coupled to, the wavelength-shifting plates is slightly underestimated. A performance increase in those adjacent PMTs is still observed, however, indicating that the Monte Carlo model is successfully simulating the photons that escape the plate and strike a different PMT.

One source of the remaining disagreement between the simulations and the experiment is likely the behavior of light at the surfaces of the wavelength-shifting plates. The behavior of light at the wavelength-shifting plate surfaces, and specifically the surface roughness of the wavelength-shifting plates, is expected (and indeed, from the experimental results, is seen) to have a significant effect on the overall light collection behavior of the wavelength-shifting plates. There are two main optical models available in the Geant4 code: GLISUR, which is the original model carried over from Geant3, and Unified, which is based on the TRIUMF *DETECT* simulations [70]. In this case, the Unified model performs far better than the GLISUR model at accurately reproducing the behavior seen in the experiment, though photon behavior at interfaces is a very complex process and may still be driving some of the remaining difference between simulated and experimental results.

Because only a single wavelength-shifting plate and PMT were considered in the previous dark box experiment, light leakage from the plate's surfaces was not observed directly, and only the behavior of the light that was retained in the plate by total internal reflection was of interest. After the simulations were tuned to match the experimental results from the one-ton detector described above, they were also repeated for the dark box experiment and were found to still be consistent with those experimental results as well.

The cross-talk observed in the experimental results and now modeled by the simulation results is an important phenomenon when considering the inclusion of wavelength-shifting plates in a large-scale water-Cherenkov detector, as the locations of the PMTs that produce photoelectrons in an event, and the times at which they produce these photoelectrons, are used to reconstruct the vertex of that event. If a large portion of the light captured by a plate escapes and strikes a different PMT, potentially on on the opposite side of the detector, this may detriment an algorithm's ability to reconstruct accurately the original event vertex. This will likely partially balance the benefits of increased light collection by individual PMTs.

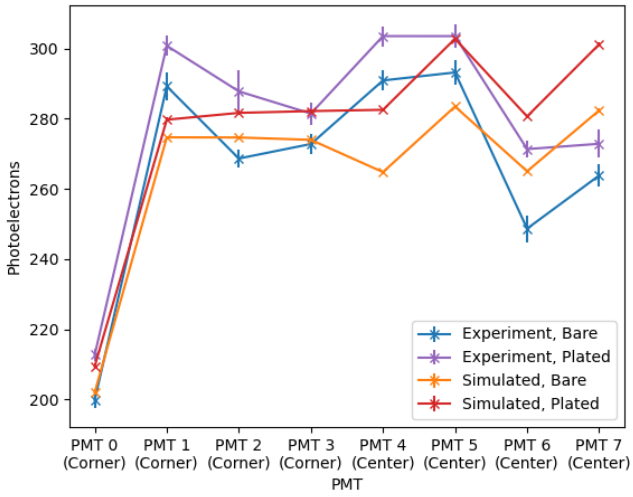

(a) Total Photoelectrons

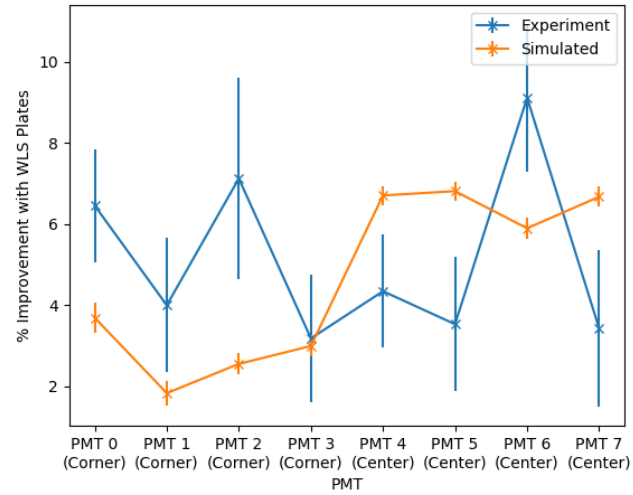

(b) Light Collection Improvement with WLS Plates

Figure 4.6 A comparison of the experimental and simulated results, represented by (a.) the total number of photoelectrons produced by the PMTs and (b.) the percentage improvement in light collection provided by the wavelength-shifting plates from the one-ton water-Cherenkov detector. The overall behavior of the wavelength-shifting plates are represented in the simulations, though the corner PMTs, which are never coupled to wavelength-shifting plates, see slightly poorer light collection improvement in the simulations compared to the experimental results, while the center PMTs see slightly better light collection in the simulations compared to the experimental results.

4.5 Conclusions

This experiment has demonstrated the ability of wavelength-shifting plates to increase the light collection efficiency of PMTs in a water-Cherenkov detector. With the inclusion of wavelength-shifting plates, PMTs collect $5.0 \pm 0.8\%\%$ more light when coupled to a wavelength-shifting plate, and still collect $5.1 \pm 0.9\%\%$ more light even if they are not coupled directly to a wavelength-shifting plate. This apparently significant cross-talk phenomenon of light escaping from a wavelength-shifting plate and striking a different PMT, however, may be detrimental in a large-scale water-Cherenkov detector, as it may interfere with event reconstruction.

Now that the behavior of the wavelength-shifting plates is validated in the simulation framework using data from comparable experimental conditions, it is of interest to use the simulations to predict the behavior of the wavelength-shifting plates in a large-volume water-Cherenkov antineutrino detector and the effects that these plates will have on the overall energy resolution, vertex position reconstruction, and signal-to-background of the detector. These simulations and analysis are described in the next chapter.

Chapter Five

Performance of Wavelength-Shifting Plates in a Large-Scale Detector Simulation

5.1 Overview

Utilizing a Monte Carlo code allows for wavelength-shifting plates to be tested in configurations that are not feasible in small-scale experimental conditions. While the performance of the wavelength-shifting plates in a one-ton water detector can be experimentally probed, their performance in a full-scale, kiloton-scale water-Cherenkov detector experiment cannot be directly predicted from those results. Instead, a Monte Carlo simulation of such a full-scale detector was performed to predict plate performance in those conditions and their overall effect on the performance of the detector system.

The goal of the detector system of interest is the detection or monitoring of one nuclear reactor facility (either a single core or multiple cores co-located in a single facility). In order to achieve this goal, the detector must be able to detect and identify antineutrinos coming from the nuclear reactor core of interest and compare the rate of these neutrinos to a hypothesis. For the case of reactor discovery, this hypothesis is that there is no nuclear reactor present, and thus the expected antineutrino rate from the reactor is zero. For the case of reactor monitoring, this hypothesis is that the nuclear reactor facility of interest is operating, and thus the expected antineutrino rate from the reactor is non-zero. The goal of the wavelength-shifting plates is to allow the detector to reject these hypotheses at a greater range from the reactor facility of interest or in less time. As the location at which a large-scale antineutrino detector is located is generally fixed, it is most useful to look at the time it takes for such a detector to reject the null hypothesis. If wavelength-shifting plates can reduce this time, it will be shown that they aid in the detector's operation.

5.2 Simulation Framework

To test the benefits and drawbacks of including wavelength-shifting plastics in a large-scale water-based detector, the simulation framework RAT-PAC was once again utilized to simulate a suite of candidate signal and background events. To simulate inverse beta decay events, positrons and neutrons were individually generated in the detector volume according to the energy spectrum of a nuclear power reactor positioned 25 kilometers away from the detector, as provided by the Geoneutrinos.org model [71].

After an antineutrino interaction event is simulated in RAT-PAC, it must undergo event reconstruction to determine the interaction location and energy of the event. This information is important for accurately identifying antineutrino events and discriminating against sources of background. To do this, the analysis code sets FRED (Functions to Reconstruct Events in the Detector) and BONSAI (Branch Optimization Navigating Successive Annealing Iterations) were used [72]. For brevity, these analysis codes will be referred to collectively as "FRED" for the remainder of this work. FRED analyzes the timing distribution of light reaching the PMTs and being converted into charge and compares it with an expected distribution. It then uses a maximum likelihood fit, a method first developed during the Super-Kamiokande experiment, on these timing residuals to identify the most probable vertex for an event in time and space. This is performed by trimming branches—which may center on local minima rather than global minima—until a result is found. The program then outputs the number PMTs triggered in an event, which is by default defined as a 1500 ns window, and the location at which the event likely occurred. It also returns other useful information about the reconstructed vertex, and passes information on the true Monte Carlo particle position and energy.

5.3 Simulation Geometry and Properties

A nominal design of a large-volume antineutrino detector, developed by the WATCHMAN Collaboration, was used as a test-bed for determining the behavior of wavelength-shifting plates in a kiloton scale detector. The detector configuration simulated, a 16 meter by 16 meter right cylindrical detector, can be seen in Figure 5.1a [59]. For this test, a detector with 15% photocathode coverage was considered. That is, 15% of the detector's inward-facing surface area was effectively covered by the photocathodes, or sensitive areas, of PMTs. The remaining 85% of the detector's surface area was covered in a black tarp to prevent the errant reflection of photons. This simulation includes all of the important geometric and physical features needed for a large-volume water-based detector, such as the detector volume itself, PMTs, and support structures, which are important to consider as potential sources of background radiation due to the natural caesium and cobalt content of steel. This baseline design was then modified to include wavelength-shifting plates. This detector configuration with

wavelength-shifting plates will be referred to here as a "plated detector".

An example of a kiloton-scale detector including wavelength-shifting plates is depicted in Figure 5.1b. The plate is positioned a short distance (37 mm) forward from the PMT position so that it sits on the PMT's glass bulb to match the experimental work performed in the preceding chapters. As with the wavelength-shifting plates in the experimental work, the radius of the center hole of the plate is defined such that it has points of intimate contact with the surface of the bulb, and the hole is beveled to match better with the shape of the bulb. The outer dimensions of the plate are defined to maximize utilized space between PMTs, with a small gap included so that adjacent plates do not touch, which results in square plates with an edge size of 20 inches. Besides introducing additional engineering challenges, having adjacent wavelength-shifting plates touch would optically couple them together, allowing light to more easily transfer between different plates. This is not desirable as it will further degrade the analysis' ability to accurately reconstruct events in the detector, which will be discussed later in this chapter. A close-up view of a single wavelength-shifting plate-PMT pair can be seen in Figure 5.2. The plates were lined on their outer edges with a reflective tape, representing specular aluminized tape, to prevent light from escaping in those directions.

5.4 Analysis Process

To test the wavelength-shifting plate behavior in a large-scale water-Cherenkov detector, a series of production runs were completed. The signals seen by the detector—namely positrons and neutrons from an IBD event—along with a series of the detector's dominant backgrounds were simulated. The backgrounds in the detector are primarily from gamma and beta rays from the PMT glass and the detector walls and support structure, along with impurities dissolved in the water itself. These backgrounds are expected to be one of the largest source of IBD spoofing events seen by the detector. As discussed in Chapter 1, muogenic false coincidences, or IBD-spoofing events generated by muons passing by the detector, will be largely precluded by the detector's active veto. Those muogenic sources of background that survive the detector's veto cut will be subdominant to the accidental and other antineutrino backgrounds considered here. Antineutrinos from other sources, such as global reactors and geoneutrinos, were simulated in the same way as the "signal" IBD events from the nuclear power reactor facility of interest. For a detector with no capability to reconstruct the direction of an antineutrino event and limited energy resolution, the antineutrinos from these sources are indistinguishable from the antineutrinos from the nuclear power reactor facility of interest, making them an irreducible background. A detector with the ability to reconstruct the direction of an incoming antineutrino may be able to reduce the global reactor background and the geoneutrino background by rejecting any event that does not originate from the direction of the nuclear reactor facility of interest. Similarly, a detector with sufficiently good energy resolution may

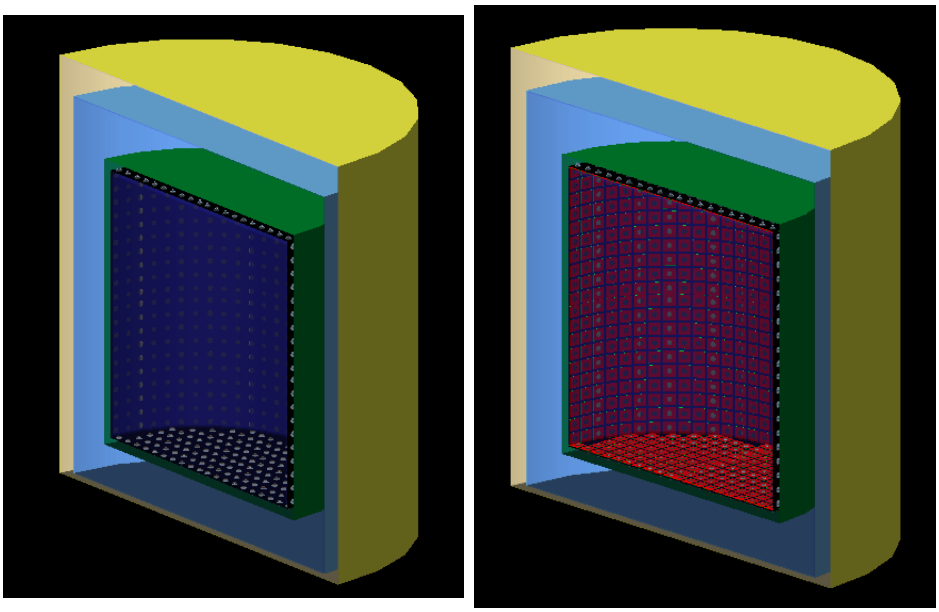

(a) Baseline **(b)** Plated

Figure 5.1 A kiloton-scale water-Cherenekov detector as implemented into RAT-PAC. A baseline, "bare" configuration not utilizing wavelength-shifting plates is depicted on the left, while a "plated" configuration with wavelength-shifting plates, in red, is depicted on the right. The PMTs are the small yellow and blue-grey circles lining the detector's edges. The detector's veto region is depicted in light blue around the inner detector.

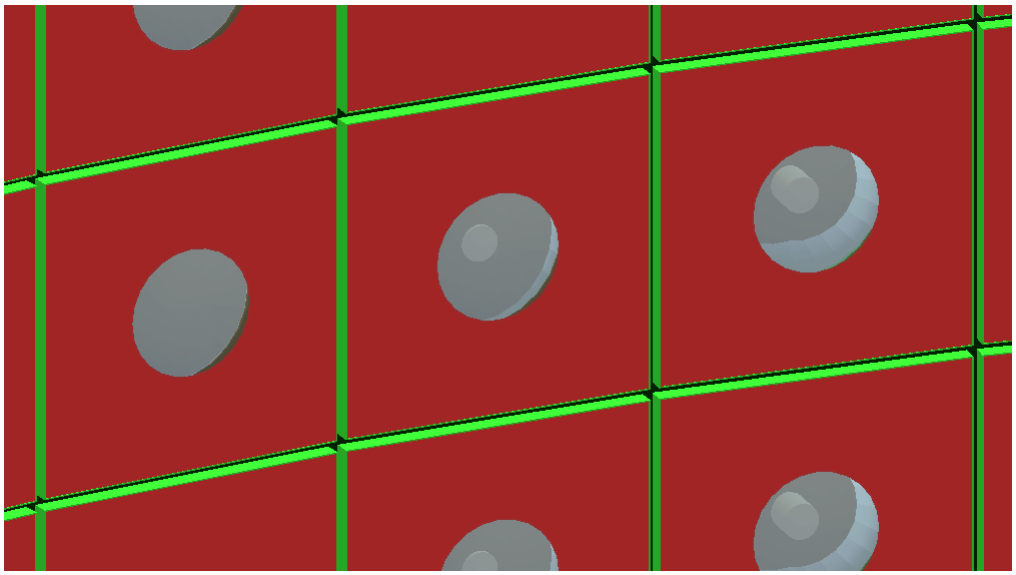

Figure 5.2 A closeup of a series of PMTs with wavelength-shifting plastic surrounding the bulb. The PMT is depicted in blue-gray, the wavelength-shifting plastic is depicted in red, and the aluminized tape reflector is depicted in green.

be able to reject some geoneutrinos as they generally have lower energies than reactor antineutrinos.

Once these simulations were performed, the singles rates from the background gamma and beta interactions were combined, with Poisson statistics, to find the number of false coincident events. These were defined as two events that fall within a 100 microsecond timing window and a 2 meter spatial coincidence window. To pass these cuts, two events' reconstructed event time and vertex position, as determined by FRED, must fall within 100 microseconds and 2 meters of each other, respectively. False coincidences that meet these requirements can appear the same to the detector and analysis codes as an IBD event, making them a source of background counts.

To reduce the number of these accidental background counts from beta and gamma interactions in the detector, two other cuts are applied. First, beta and gamma events are most likely to occur near the periphery of the detector, as many of the beta and gamma emitters of concern are found in the photomultiplier tubes themselves or their surrounding support structures. Because betas and gammas have relatively short ranges in water, these radioactive contaminants are most likely to create light around the outer edge of the detector. Because of this, only events that are reconstructed to the center volume of the detector, known as the fiducial volume, are considered as candidates for IBD events. The outer volume of the detector, generally a meter or so from the PMT wall, thus serves as a passive shield against these accidental background sources. This cut is known as the fiducial cut.

A second cut is applied on events reconstructed to the fiducial volume: each event must trigger a set number of PMTs, where "triggering" is defined as producing at least one photoelectron in an event. The number of PMTs that trigger in an event is a proxy for the total amount of light produced in the event, if you assume that each PMT produces few photoelectrons. This assumption is generally valid for events that occur in the fiducial volume, far from the PMT wall, where the light from the event will be spread out across a number of PMTs. This assumption will also punish events that occur closer to the PMT wall but are mistakenly reconstructed into the fiducial volume, as they are more likely to produce many photoelectrons in a smaller number of PMTs. Counting the number of PMTs triggered, rather than the number of photoelectrons produced, helps to penalize these background events that make it past the fiducial cut. Because the total amount of light produced in the detector is a function of the energy deposited in the detector volume, this cut is known as the energy cut. Because IBD events, and in particular the capture of the IBD neutron, deposit more energy in the detector than most sources of accidental backgrounds, this cut helps to further reduce the number of accidental background events counted.

A point of comparison is needed between the plated and bare detector configurations to test detector performance. A signal-to-background ratio is one measure well suited for this role, defined as:

$$S/B = \frac{s}{\sqrt{s+b}} \tag{5.1}$$

where s and b are the signal rate and background rate, per day, respectively.

The backgrounds of the detector encompass both accidental coincidences caused by background gamma and beta interactions in the detector that survive the fiducial and energy cuts and antineutrino interactions from other sources besides the nuclear reactor facility of interest, such as global reactors and geological sources. The signal is defined as the number of IBD events from the nuclear reactor facility of interest.

For wavelength-shifting plates to provide an overall benefit to the detector, they must improve its signal-to-background. The primary benefit they will confer to this end is to improve the overall energy resolution of the detector by more efficiently collecting the light from each event. This improved energy resolution will allow for a more accurate energy cut to be applied, reducing the number of accidental background events counted without penalizing true signal events. However, wavelength-shifting plates may degrade the position reconstruction of the detector by smearing the timing of light arriving at the PMTs in the detector. While this smearing can be accounted for in the reconstruction, using the Monte Carlo results to effectively predict the average amount of time light will reside in a plate before striking a PMT, the actual residence time of each photon in the plate will vary. Due to this distribution in timing, it is more difficult for the algorithm to successfully reconstruct the location of an event within the detector volume. This may cause more background events to reconstruct into the fiducial volume, or cause signal events to reconstruct outside of the fiducial

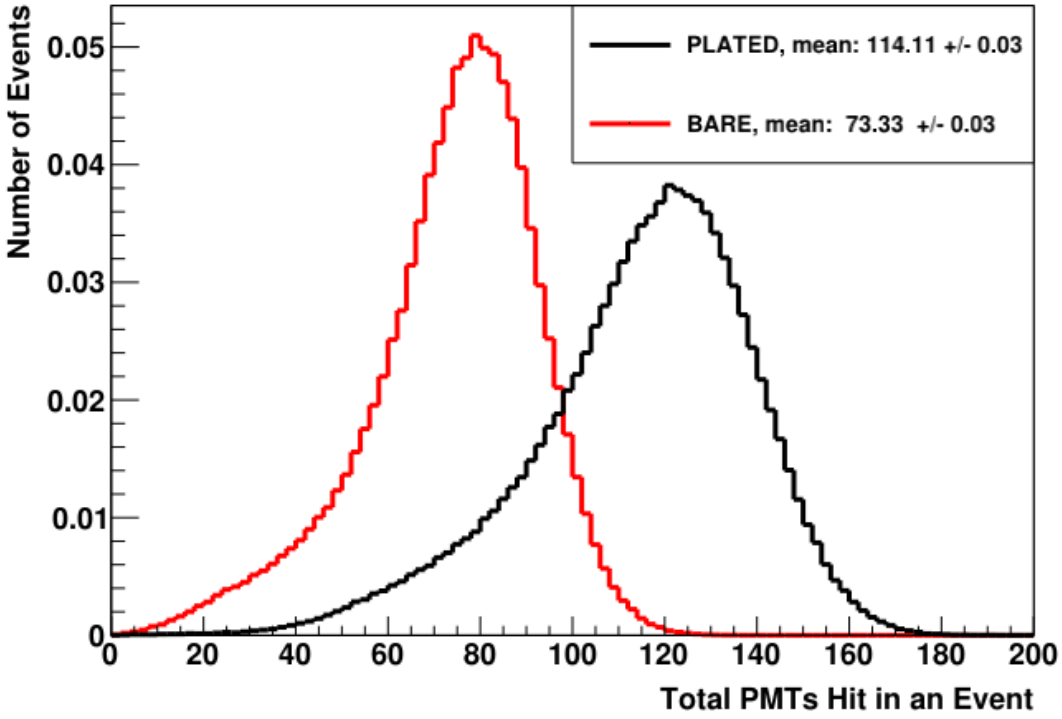

Figure 5.3 The total number of PMT hits in the detector, with and without wavelength-shifting plates, when 15 MeV positrons are simulated in the detector volume. The wavelength-shifting plates guide, on average, an additional 56% of light to the PMTs that would have otherwise been missed in the "bare" configuration.

volume. This detriment is expected to be in competition with the improvement in energy resolution provided by the wavelength-shifting plates when determining the overall effect the plates have on the signal-to-background of the detector. These two effects are considered in the subsequent sections.

5.5 Effects on Energy Resolution

To test the effect that the inclusion of wavelength-shifting plates has on the overall light collection of the detector, 15 MeV positrons were simulated in the detector's volume. These mono-energetic positrons were simulated first instead of IBD-spectrum positrons as they will produce a more consistent amount of light in the detector are thus well suited for a comparison of light collection between the bare and plated detector configurations. The improvement of light collection on IBD-spectrum positrons, and on neutrons and backgrounds, will be considered subsequently.

It can be seen from Figure 5.3 that the wavelength-shifting plates guide an additional 56% of light to the PMTs, increasing the amount of light collected in the detector from 73.3 PMTs triggered in the bare configuration to 114.1 PMTs triggered in the plated configuration. This is consistent with expectations set by the IMB-3 detector, which found that coupling 5 inch photomultiplier tubes to 24 inch wavelength-shifting plates doubles their light collection [28]. In this case, a 10 inch photomultiplier tube is coupled to a 20 inch wavelength-shifting plate, which is a 42% reduction in plate surface area compared to the IMB experiment, explaining the reduction to only 56% light collection improvement. This is overall still a substantial increase, though much of the excess light that is collected in this case is either delayed by the wavelength-shifting plates before arriving to the PMTs, or escapes the wavelength-shifting plate and strike a different PMT than originally intended. Both of these effects will degrade the reconstruction algorithm's ability to reconstruct the location of the event in the detector, as will be described in the subsequent section.

Similar results can be seen for IBD-spectrum positrons and neutrons simulated in the detector volume, which both evidence a 47% light collection improvement with wavelength-shifting plates, as seen in Figure 5.4. It is of interest, then, to investigate whether potential sources of background, such as beta and gamma emissions from potassium-40 in the PMT glass, likewise benefit from the inclusion of WLS plates in the detector. As can be seen in Figure 5.5, the wavelength-shifting plates create a less significant improvement in the amount of light collected from these potential background events. This is due to the fact that background events preferentially occur on the outer edge of the detector, close to the PMT wall. Therefore, light that is created in a background event is more likely to be concentrated in a small number of nearby PMTs. Because each PMT will generally be struck by multiple photons, the presence of WLS plates on those PMTs will not significantly affect the number of PMT's that produce at least one photoelectron in an event.

Attention can now be turned to how this increase in light collection translates to an increase in detector energy resolution. As can be seen in Figures 5.6 and 5.7, the wavelength-shifting plates serve to increase the number of PMTs triggered for a given energy deposited in the detector. The amount of light collected by the detector is more tightly correlated to the amount of energy deposited in an event when wavelength-shifting plates are present. This makes sense, as the statistical variation in light collection is expected to decrease as a greater amount of light is collected.

An overall energy resolution of the detector can then be calculated, the results of which are given in Table 5.1. The bare detector, without wavelength-shifting plates, has an energy resolution of 18.7 $\pm$ 0.1% at 3 MeV, where 3 MeV is chosen as a convenient sample value as it falls within the continuous energy spectrum from IBD events. The plated detector has an energy resolution of 17.8$\pm$0.1% at 3 MeV, a 5% relative improvement over the bare detector. The same analysis can be performed with higher energy, 15 MeV positrons. In this case, the bare detector has an energy resolution of 13.41 $\pm$ 0.02% while the plated detector has an energy resolution of 12.45 $\pm$ 0.01%, a

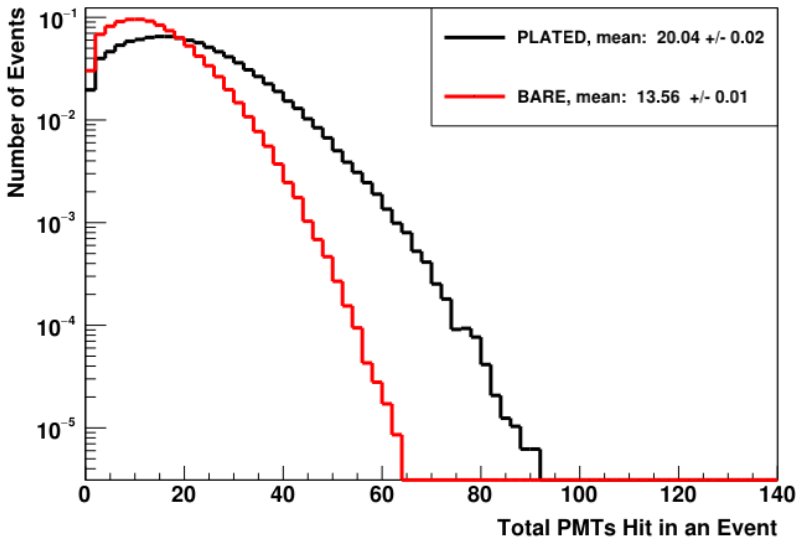

(a) Positrons

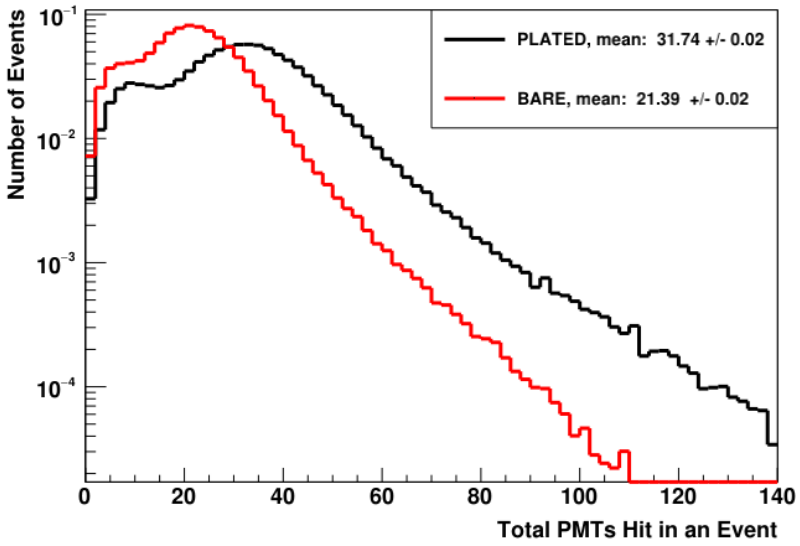

(b) Neutrons

Figure 5.4 The total number of PMTs triggered in the detector, with and without wavelength-shifting plates, when (a.) IBD-spectrum positrons and (b.) IBD-spectrum neutrons are simulated in the detector volume. Around 47% more PMTs produce signals when wavelength-shifting plates are present in the detector compared to when they are not.

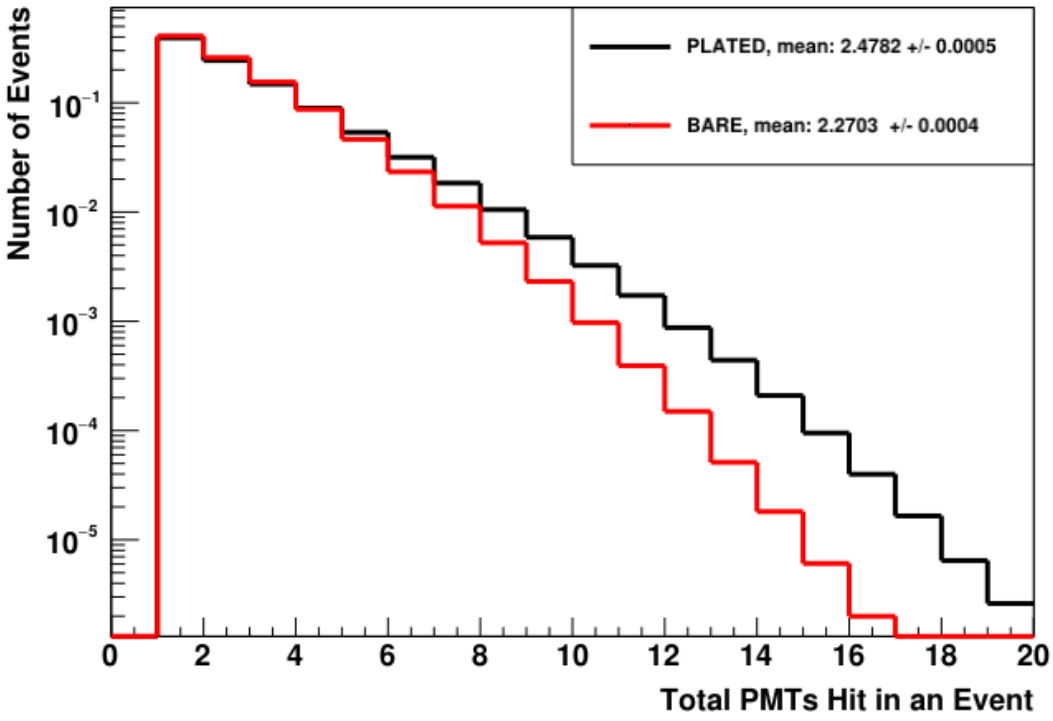

Figure 5.5 The total number of PMT hits in the detector, with and without wavelength-shifting plates, when potassium-40 beta emissions are simulated in the PMT glass. The amount of light produced by the PMTs is increased slightly by the presence of the plates.

Table 5.1 The improvement in energy resolution provided by wavelength-shifting plates for both 3 MeV and 15 MeV positrons. The increase in light collection afforded by the WLS plates allows a 5% to 7% improvement to energy resolution.

	Energy Resolution for	
	3 MeV Positrons	15 MeV Positrons
No WLS Plates	18.7 ± 0.1 %	13.41 ± 0.02%
With WLS Plates	17.8 ± 0.1 %	12.45 ± 0.01 %

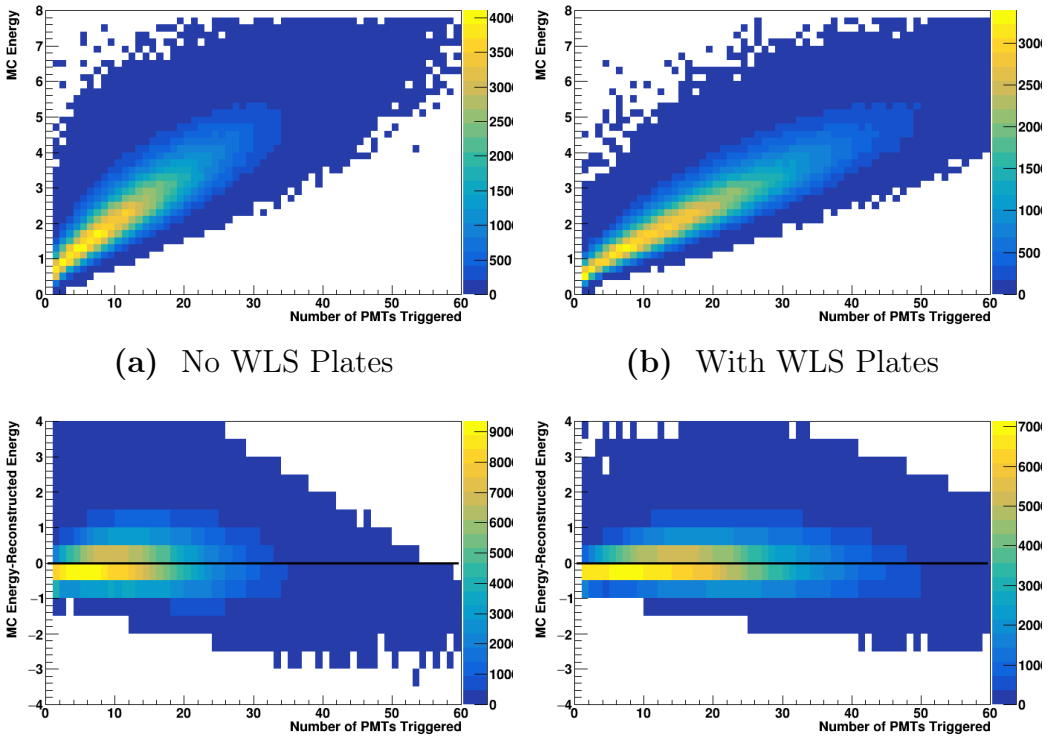

(a) No WLS Plates **(b)** With WLS Plates

(c) No WLS Plates **(d)** With WLS Plates

Figure 5.6 The amount of PMTs triggered in an event, on the x-axis, versus the energy deposited by the event in the detector, on the y-axis, for both a (a.) bare and (b.) plated detector configuration. The wavelength-shifting plates serve to reduce the variance of the points along the trendline, as can be seen in the residuals plots (c.) and (d.) at the bottom of the figure. Points are for IBD-spectrum positrons generated in the detector volume.

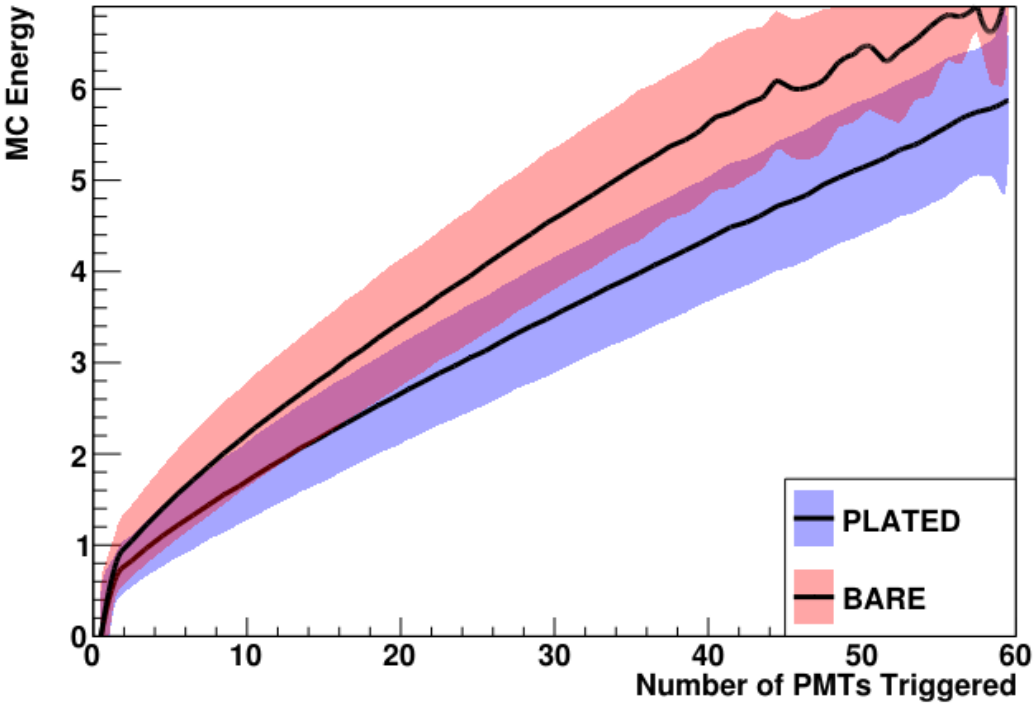

Figure 5.7 A comparison of the energy resolutions between a detector with and without wavelength-shifting plates. Note that the detector with wavelength-shifting plates sees more light from events of a given energy, giving it better statistics and thus better energy resolution.

relative improvement of 7%. This improved energy resolution allows for a better discrimination between IBD positrons and neutrons (which will generally deposit several MeVs of energy in the detector) and betas and gammas (which will generally deposit closer to 1 MeV of energy). This improvement in the energy resolution of the detector will allow for a more accurate energy cut that will better remove the accidental backgrounds from beta and gamma interactions in the detector while not removing true signal positron and neutron events.

5.6 Effects on Vertex Reconstruction

As previously described, the FRED analysis codes reconstruct the location an event occurs in a detector by analyzing the timing profile with which light arrives at the detector's PMTs. This profile is compared against a pre-generated timing profile for the detector and used to assign a location of maximum likelihood for the event to have taken place. This information is then, in turn, used to determine whether an event survives the analysis's fiducial cut.

When wavelength-shifting plates are present in the detector, light that is absorbed in the plate is delayed by an unknown amount of time (generally a nanosecond or two) before being re-emitted. After re-emission, the photon must travel through the plate to reach a PMT – the exact delay this causes depends on the photon's (unknown) path length. Along this path, the photon, depending on its wavelength, may be re-absorbed, introducing an additional delay if it is re-emitted. Finally, the photon may escape the plate and travel across the detector to strike a different PMT. This would serve to both change the time that the photon is detected and its location, which is undesirable from the standpoint of event vertex reconstruction. The result of all these delays are visible in Figure 5.8, where the inclusion of wavelength-shifting plates in the detector leads to a substantially elevated tail in the detector's timing residuals, defined here as the difference between the photon's expected arrival time (assuming straight-line travel from its point of origin to the PMT) and its actual arrival time. The positive values on the graph (i.e. light that seemingly arrives at the PMT faster than straight-line travel would allow) is from the timing jitter of the PMTs. The features at -50 ns and -30 ns are both artifacts of the PMT's electron transit times.

Only photons collected within a certain time window around the reconstructed event time are used by the reconstruction algorithm. In a detector without wavelength-shifting plates, this window is generous, usually 1.5 microseconds around the event. Adjusting the size of this window may be able to mitigate the negative effects of the wavelength-shifting plates on the performance of the reconstruction algorithm by excluding some of the more egregiously delayed light.

Making the time window smaller may allow for a large portion of the light collected by the wavelength-shifting plates to be excluded from the event's position reconstruction. In this case, the analysis could largely proceed as it does when wavelength-shifting plates are not present in the detector. Ideally, this would pre-

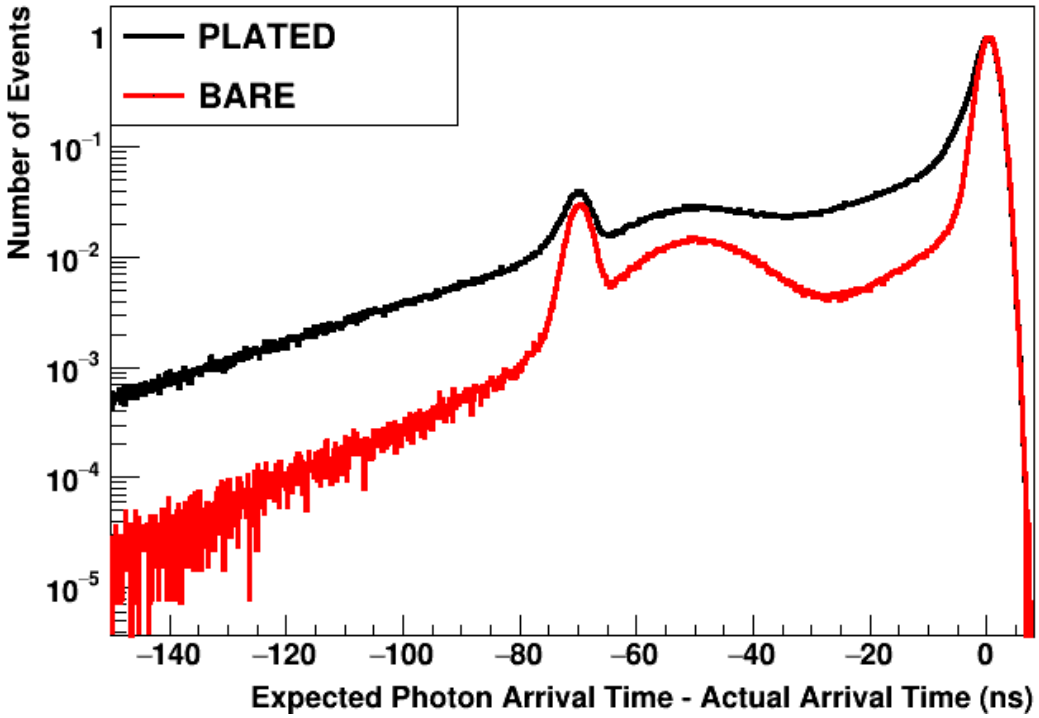

Figure 5.8 The expected arrival time of light to the PMTs in the detector minus when the light is actually detected, with and without wavelength-shifting plates, when IBD-spectrum positrons are simulated in the detector volume. The wavelength-shifting plates substantially delay some of the light arriving at the PMTs, leading to the "smearing" of the spectrum observed here. The features between -80ns and -20ns are artifacts from the electron transit times of the PMTs. The x-axis is negative by convention.

vent performance from being degraded at all. However, even with a more stringent timing window, it is not possible to exclude all light from the wavelength-shifting plates without also excluding some of the light that travels directly to a PMT. Therefore, while adjusting the timing window will not be able to fully compensate for the wavelength-shifting plates in the detector, decreasing it may serve to mitigate their negative effects.

The effects of adopting four different timing windows is shown in Figure 5.9. The x axis of the plot is the reconstructed distance from the event's vertex to the nearest PMT. Occasionally, events will fail to reconstruct and will be placed by the algorithm at a negative value, represented by the far left bin of the histogram. It can be seen that reducing the event's timing window to 50 ns (25 ns before and after the reconstructed event start) can decrease the number of events that fail to reconstruct and are placed at that negative value. Moving from a 500 ns window around the event start to a 100 ns window reduces the fraction of failed reconstructions from around 20% to 16%, though it can be seen by comparing the 100 ns window to the 50 ns window that further shrinking the timing window gives diminishing returns. Additionally, shrinking the timing window substantially increases the amount of time needed for the analysis to complete. Comparing the different timing windows, it is seen that the majority of these salvaged events occur within 1.5 meters of the PMT wall, as shown by the excess of events in those bins for the 200 and 100 ns timing windows. A 100 ns timing window is used for the subsequent analysis as it provides good reconstruction behavior in a reasonable amount of time.

Another indicator to measure the effect wavelength-shifting plates have on the analysis's ability to reconstruct events in the detector is the vertex reconstruction residual. This residual is defined as the straight-line distance between an event's true, Monte Carlo interaction vertex and its reconstructed interaction vertex (events that fail to reconstruct are excluded). The larger this value, the worse the reconstruction algorithm is performing. This value is plotted for a detector with and without wavelength-shifting plates, for both IBD-spectrum positrons in the detector and potassium-40 in the PMTs' glass, in Figure 5.10. In both cases the residual is found to be increased by the presence of wavelength-shifting plates. This can be seen primarily in the long tail of the distribution, which is noticeably elevated by the presence of wavelength-shifting plates in the detector, indicating a larger number of events being reconstructed very distantly from their actual vertex. This elevated tail is particularly noticeable in the case of potassium-40, which sees a dramatically increased number of events reconstructing 2.5 to 3 meters from where they actually occur.

The practical effects of degraded reconstruction capabilities are twofold. First, as seen in Figure 5.11a, signal events (represented here by IBD-spectrum positrons) originating from the detector's fiducial volume are more likely to fail to reconstruct when wavelength-shifting plates are present, resulting in a negative value being returned and the event being excluded from further analysis. This can cause legitimate signal

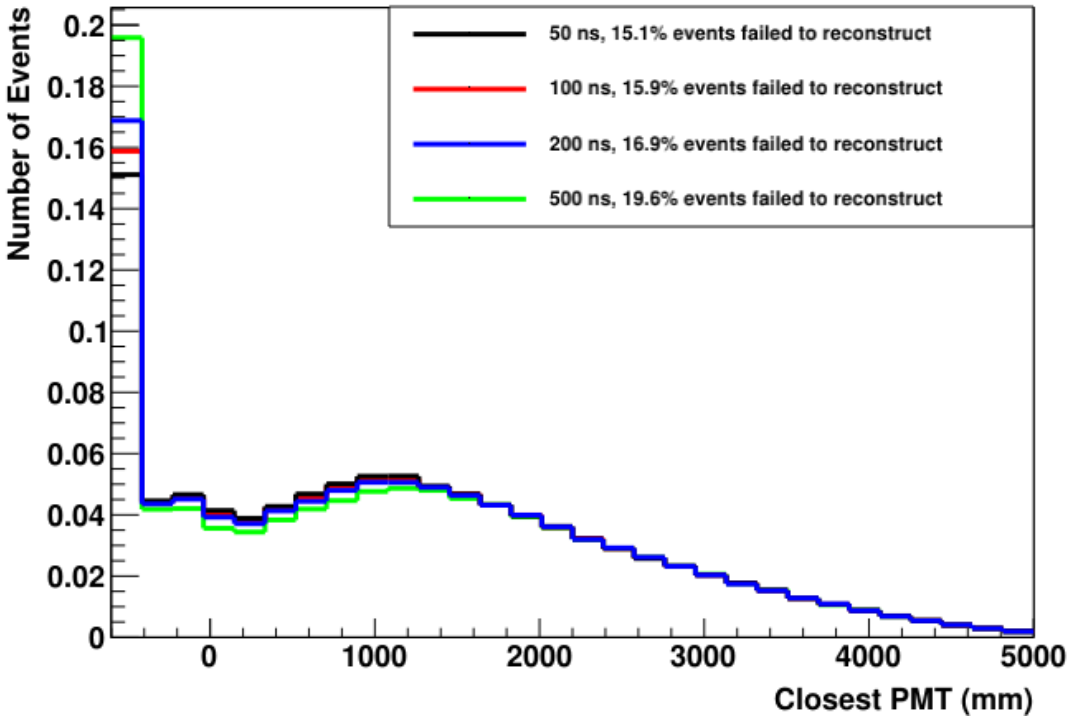

Figure 5.9 The reconstructed distance from the PMT wall of events originating from IBD-energy positrons for various timing window sizes when wavelength-shifting plates are present in the detector. Note that shrinking the timing window reduces the number of events that fail to reconstruct and are assigned a negative distance.

events to be eliminated, reducing the overall data rate and signal-to-background. Second, as can be seen in Figure 5.11b, background events originating from radioactive impurities in the PMTs' glass and support structure are more often reconstructed into the detector's center when wavelength-shifting plates are present. This is significant as it allows these events to pass the analysis's fiducial cut and can increase the number of accidental background events recorded by the detector. Beyond these two effects, the degradation of reconstruction capabilities would also worsen the ability of a detector to reconstruct an antineutrino's direction of travel, if it was desired for the detector to have this capability. The antineutrino's direction of travel is reconstructed by comparing the positions of the positron and neutron event vertices, and thus worsening the reconstruction of these positions worsens the reconstruction of the antineutrino's direction [6]. The following analysis, however, assumes that no directional information is reconstructed for the antineutrinos, and thus this effect is not considered further here.

Overall, it is clear that it is not possible to fully compensate for the uncertainties

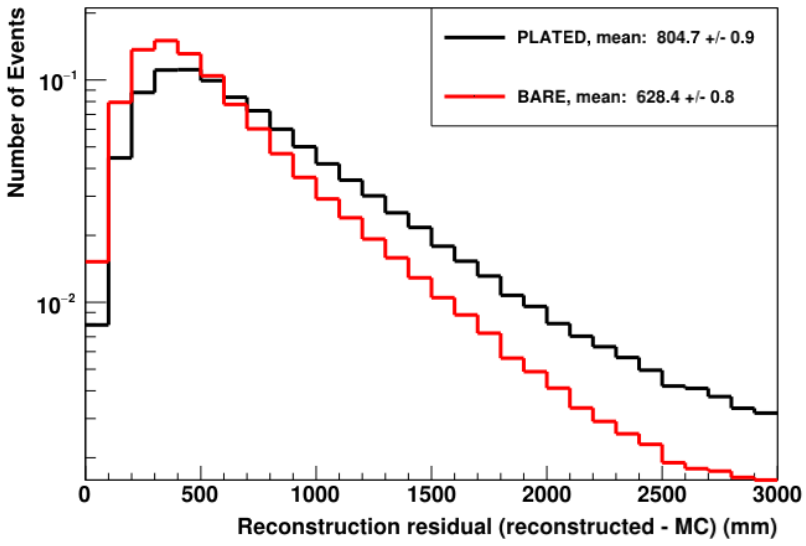

(a) Positrons

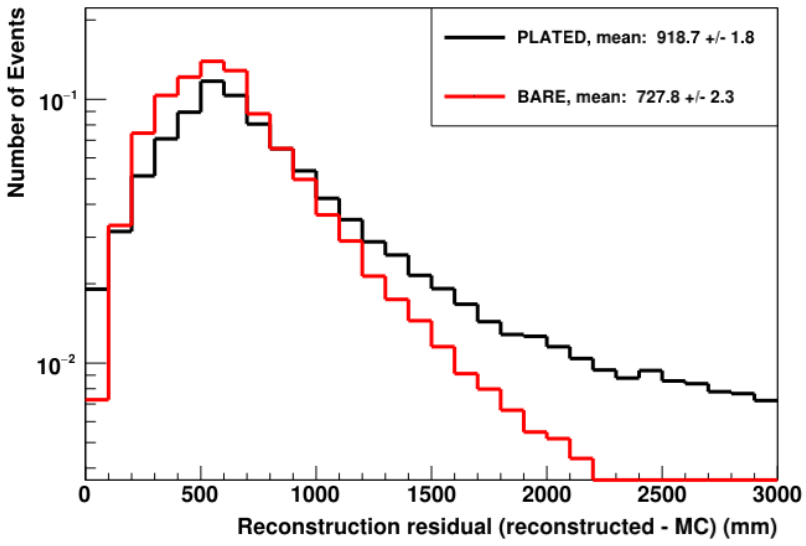

(b) Potassium-40

Figure 5.10 The reconstruction residual, defined as the straight-line distance between an event's true (Monte Carlo) interaction vertex and its reconstructed interaction vertex. Events are from (a.) IBD-energy positrons in the detector and (b.) potassium-40 emissions in the PMT glass. Note the elevated tail for the residuals when wavelength-shifting plates are present in the detector.

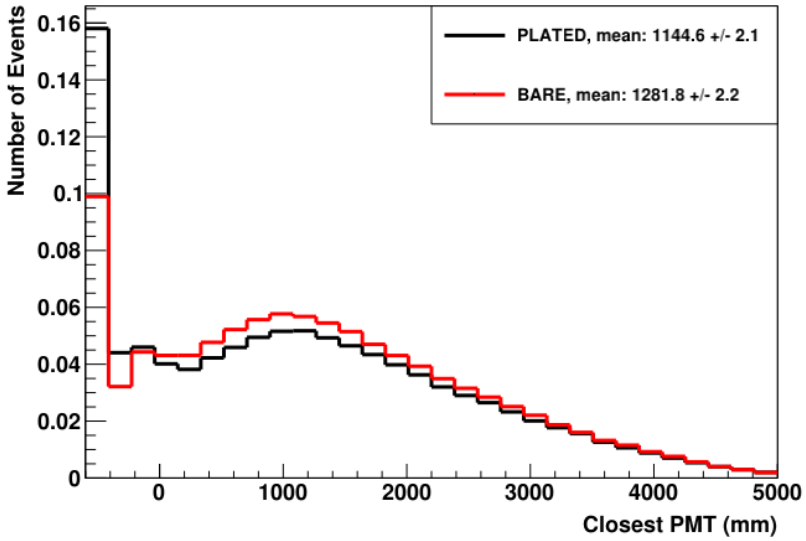

(a) Positrons

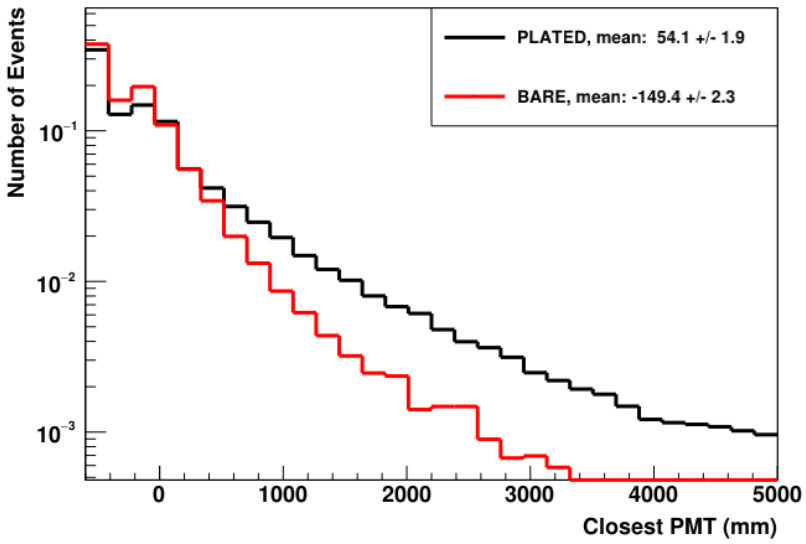

(b) Potassium-40

Figure 5.11 The distance from the center of the detector that events originating from (a.) IBD-energy positrons and (b.) potassium-40 decays are reconstructed at, with and without wavelength-shifting plates. Note how the plates increase the number of signal events that fail to reconstruct properly and are assigned a negative distance and increase the number of background events that are reconstructed towards the center of the detector.

introduced by wavelength-shifting plates when considering event vertex reconstruction. This effect, therefore, will likely partially counteract the improvement to detector energy resolution described in the previous section when considering the detector's overall signal-to-background ratio.

5.7 Overall Effects on Signal-to-Background Ratio

It is now of interest to calculate the overall effect that the wavelength-shifting plates have on the detector's signal-to-background and performance more broadly, taking into account both the improvements it offers in energy resolution and the challenges it introduces in position reconstruction. A suite of signal and background events were simulated in the detector, as described at the beginning of this chapter. To determine the signal rate, the results of these simulations were combined with the known antineutrino flux 25 kilometers away from the Hartlepool Nuclear Power Station in the United Kingdom, chosen as it was the original planned location for deployment of a detector by the WATCHMAN collaboration. The antineutrino background rate was determined by combining the known global reactor and geological antineutrino fluxes at that location, as provided by the Geoneutrinos.org model, with the same simulations used to determine the signal rate [71]. The total number of interactions per day from each of these sources is given in Table 5.2. The accidental background rate was determined by combining the simulation results of beta and gamma events in the PMTs, detector volume, and support structures with the known levels of radioactive contaminants of the different detector components. Poisson statistics were used to combine individual background events into IBD-candidate pairs. The antineutrino backgrounds were then added to the accidental background to arrive at the total background rate of the detector. This was then combined with the signal rate via Equation 5.1 to arrive at the overall signal-to-background of the detector.

These simulations were performed for a detector both with and without wavelength-shifting plates. In each case, the energy and fiducial cuts were optimized to maximize signal-to-background. Because of the relatively small parameter space, a straightforward optimization algorithm was used, which changed one of the cut values before testing if the new signal-to-background was better or worse. If it was worse, the change was reverted, while if it was better, the change was kept. One of the cuts was then changed again, and the process repeats itself until a maximum value was reached. The entire process was repeated several times with different starting parameters to ensure that the results were not focused on a local maximum.

The results of the optimized signal-to-background ratios can be seen in Table 5.3. The inclusion of wavelength-shifting plates in the detector is seen to increase the overall signal-to-background of the detector from 0.61 ± 0.01 to 0.69 ± 0.01, a relative improvement of 13.1%. An idealized detector can also be considered. This detector, shown in the rightmost column of Table 5.3, is considered to have a perfect detection efficiency (i.e. every antineutrino that interacts in the detector is seen and recorded

Table 5.2 The total number of antineutrinos from different sources expected to interact via inverse beta decay in a 16 meter by 16 meter right cylinder detector volume positioned 25 km away from the Hartlepool Nuclear Power Station, a 3 GWth nuclear reactor facility. Values are obtained from the Geoneutrinos.org model [71].

Source	Antineutrino Interactions per Day
Hartlepool Nuclear Power Station	4.37 events/day
Global Reactors	1.03 events/day
Geoneutrinos	0.21 events/day

Table 5.3 The overall improvement, in terms of signal-to-background and time to 3-sigma reactor discovery, provided by wavelength-shifting plates in a 16 meter by 16 meter right-cylinder detector measuring a 3 GWth nuclear reactor at a distance of 25 km. The values for an idealized detector, with a perfect detector efficiency and only geoneutrino and global reactor antineutrino backgrounds, is also included as an upper-limit comparison.

	Without WLS Plates	With WLS Plates	Idealized Detector
Total PMTs Hit Cut (Positron, Neutron)	9, 20	11, 32	N/a
Closest PMT Distance Cut	430	450	N/a
Signal Rate	0.585 ± 0.002 ev/day	0.702 ± 0.002 ev/day	4.37 ev/day
Background Rate	0.34 ± 0.01 ev/day	0.34 ± 0.01 ev/day	1.24 ev/day
Signal to Background	0.61 ± 0.01	0.69 ± 0.01	1.84
Time to 3σ	20.4 ± 0.1 days	16.0 ± 0.1 days	2.2 days

as a signal event) and no accidental sources of background. This detector can thus be seen as an absolute upper limit on detector performance.

The signal-to-background rate can now be applied to measurements of interest for the nuclear nonproliferation community. The time it takes for an antineutrino detector to reject the null hypothesis and identify an anomalous signal (for example, seeing an excess of antineutrinos due to the presence of an undeclared nuclear reactor) to a confidence of three sigma, or 99.7%, is important for the timely detection of illicit nuclear activities. Ideally, this time should be minimized. For the purposes of this analysis, assume the Hartlepool Nuclear Power Station was not declared or known when the antineutrino detector begins operations. The time to reject the null hypothesis (i.e. reject the scenario of no nuclear reactor being present) to three sigma, can be calculated using a t-test:

$$\begin{aligned} T &= \frac{S}{\sqrt{S+B}} \\ T &= \frac{s\sqrt{\tau}}{s+b} \\ \tau &= \frac{T^2}{s^2}(s+b) \end{aligned} \tag{5.2}$$

where T is the test parameter obtainable using a lookup table, S and B are the total number of signal and background events, respectively, s and b are the signal and background rates, per day, respectively, and τ is the time, in days, to reach the statistical significance specified by the T value. For three-sigma confidence, the test parameter T is 2.7478. For this equation, it is assumed that the expected background rate, b is exactly known.

For a detector without wavelength-shifting plates present, this time is 20.4 ± 0.1 days. After the introduction of wavelength-shifting plates, this time can be reduced to 16.0 ± 0.1 days. This means that, as part of a nuclear non-proliferation treaty, the inclusion of wavelength-shifting plates in the detector would decrease the time needed to detect a potential treaty violation (i.e. the operation of an undeclared nuclear reactor) by 4 days, or around 22%.

It is relatively unlikely, in a real-world scenario, for a State to use a 3 Gigawatt-thermal power nuclear reactor as simulated here to generate illicit nuclear material. It is of interest, then, to see how wavelength-shifting plates affect the time to detect the presence of a covert nuclear reactor at a lower power level. The time to detect such reactors, both with and without wavelength-shifting plates in the detector and, as a comparison, for the idealized detector described above, are given in Table 5.4. Due to the low interaction rate of antineutrinos in the detector, even an idealized detector with perfect detection efficiency and no accidental backgrounds would have difficulty discovering a nuclear reactor operating at less than 500 MWth in a useful time frame. A more realistic detector's performance is poorer, and even the time to discover a 1 GWth reactor is nearly 3.5 months. The presence of wavelength-

Table 5.4 The time to discover a reactor with different power outputs by a 16 meter by 16 meter right cylinder antineutrino detector with and without wavelength-shifting plates situated 25 km away from the reactor. The discovery times using an idealized detector with perfect detection efficiency and no accidental backgrounds are provided as comparisons. Note that reactors operating at or less than 500 MWth cannot be detected even by this idealized detector in a month, while reactors operating at 100 MWth or less are not detectable within a reasonable time frame.

Reactor Power	Time to 3σ confidence		
	Without WLS Plates	With WLS Plates	Idealized Detector
100 MWth	N/a	N/a	493.0 days
500 MWth	347 ± 2 days	252 ± 1 days	28.0 days
1000 MWth	106.2 ± 0.7 days	79.1 ± 0.4 days	9.6 days
3000 MWth	20.4 ± 0.1 days	16.0 ± 0.1 days	2.2 days

shifting plates does reduce this value by around 25% (to closer to 2.5 months for a 1 GWth reactor), though the overall time to detect such a reactor remains long. Larger detector volumes, such as moving from a 16 m by 16 m right cylinder detector to a 20 m by 20 m detector, would reduce these times at an additional cost of the detector itself. Wavelength-shifting plates can be expected to similarly benefit these larger detectors.

Alternatively, if a detector were positioned closer to the nuclear reactor, this time-to-discovery could be similarly reduced. Moving the detector to only 15 km from the reactor, instead of the present 25 km, would increase the signal rate by a factor of 3.5 without a substantial change in the background rate. At this distance, utilizing wavelength-shifting plates, a 3 GWth reactor would be discovered in only 3.5 days (versus 4.3 days without wavelength-shifting plates) and a 500 MWth reactor would even be discoverable in 34 days (versus 44 days without wavelength-shifting plates). To detect a lower-power reactor, the detector must be moved even closer: a 50 MWth reactor, for example, can be detected from 7 km away in 3.75 months (versus 5 months without wavelength-shifting plates). A comparison of the performance of a detector with and without wavelength-shifting plates across various standoff distances and reactor powers is given in Figures 5.12 and 5.13. If one chooses a required detection time, Figure 5.12 can also be used to predict the maximum allowable standoff distance to place the detector to discover an undeclared reactor in that time, and Figure 5.13 can be used to predict the minimum reactor power detectable in that time. Lastly, Figure 5.14 shows the time to detect an undeclared nuclear reactor across the parameter space of both stand-off distance and reactor power. The different contour lines are labeled with the time to detect a nuclear reactor to 3σ, which the wavelength-shifting plates reduce for a given range or power.

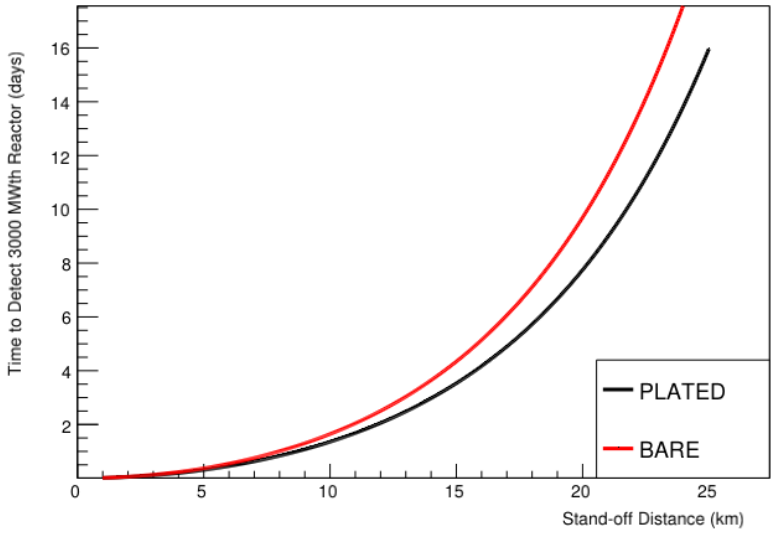

(a) 3000 MWth Reactor

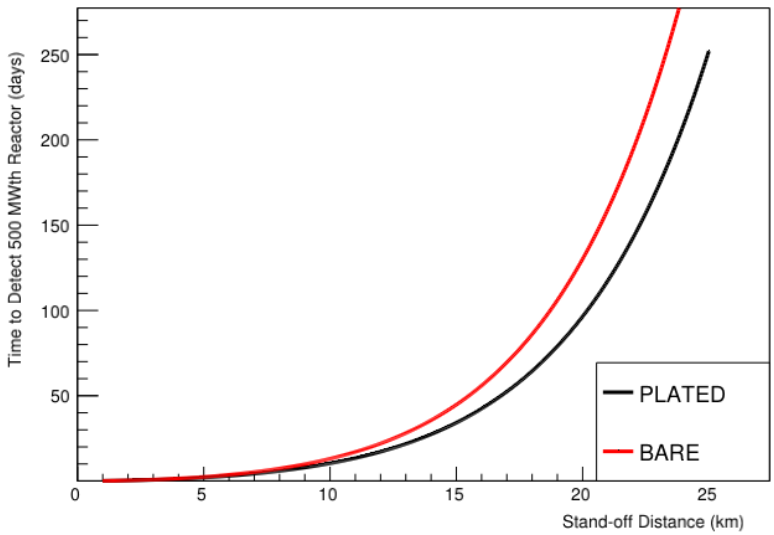

(b) 500 MWth Reactor

Figure 5.12 The time to discover (a.) a 3000 MWth reactor and (b.) a 500 MWth reactor by a detector with and without wavelength-shifting plates, across various stand-off distances. The inclusion of wavelength-shifting plates in the detector largely allow for a faster discovery of the reactor.

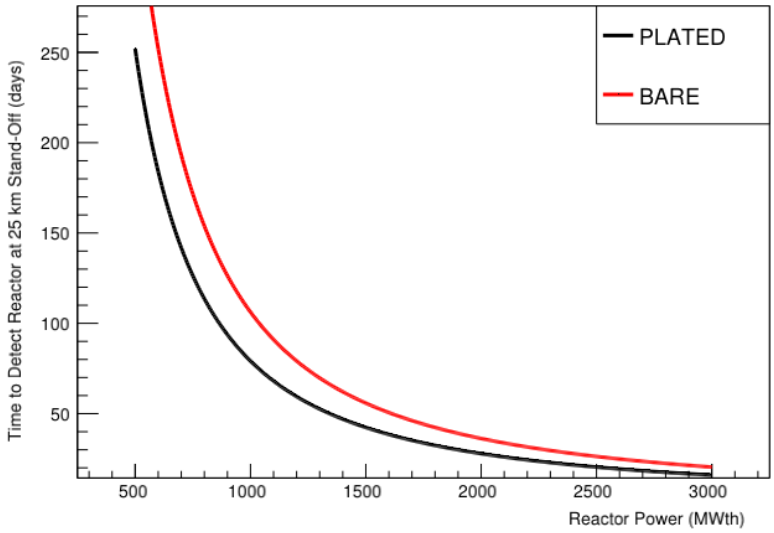

(a) 25 km Stand-Off

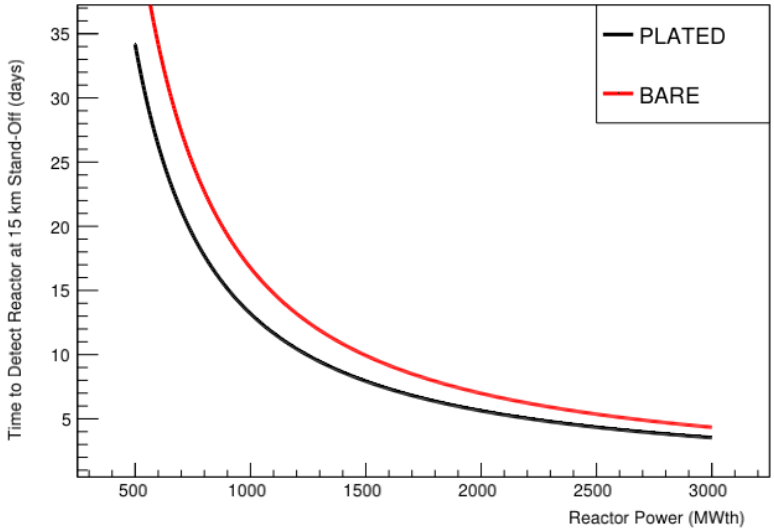

(b) 15 km Stand-Off

Figure 5.13 The time to discover a reactor of various power outputs with and without wavelength-shifting plates using a detector positioned (a.) 25 km and (b.) 15 km away from the reactor core. Wavelength-shifting plates decrease the time needed to detect the reactor to 3σ accuracy across all power levels.

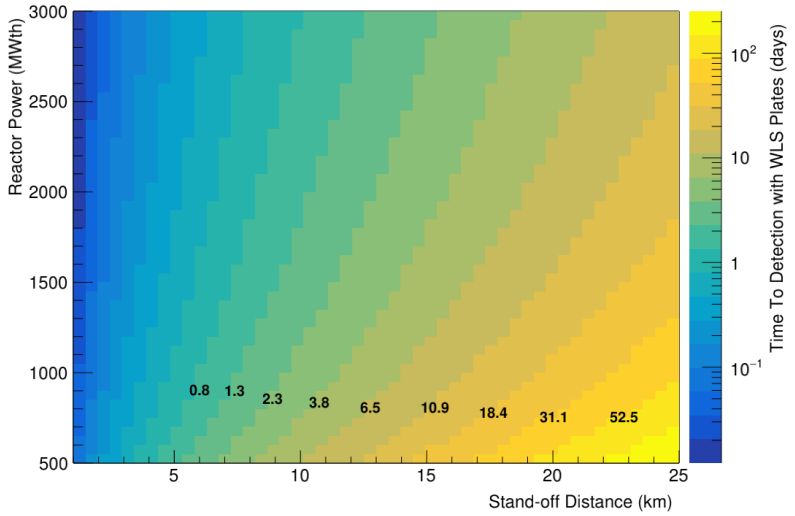

(a) With WLS Plates

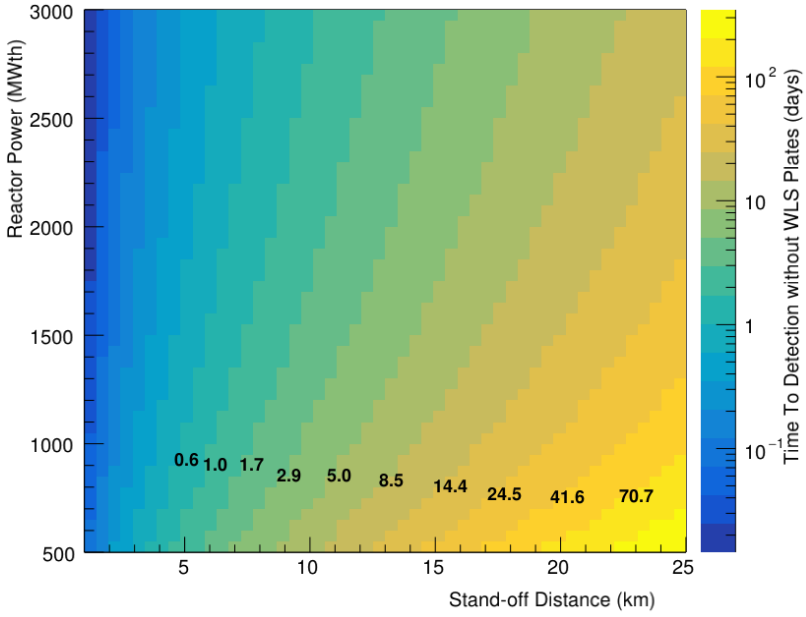

(b) Without WLS Plates

Figure 5.14 The time to discover a reactor of various power outputs at various standoff distances (a.) with and (b.) without wavelength-shifting plates. The time to detect a reactor at various contour lines are labeled and can be observed to be reduced at further stand-off distances and lower reactor powers when wavelength-shifting plates are present in the detector.

Wavelength-shifting plates have thus been shown to increase the ability of a large-scale water-Cherenkov antineutrino detector to fulfill its safeguards goals. At a given standoff distance, the wavelength-shifting plates allow the antineutrino detector to discover an undeclared nuclear reactor in a shorter measurement time. Alternatively, for a given detection time requirement, wavelength-shifting plates allow for the detector to achieve its goal from a greater stand-off distance or for a reactor of lower power output. Both of these effects increase the value of antineutrino detectors for the global nuclear nonproliferation regime.

Chapter Six
Conclusions

Wavelength-shifting plates have been demonstrated through this work to have a potential application in large-volume, water-Cherenkov antineutrino detectors. By coupling the large-surface area PMTs utilized in the detector to wavelength-shifting plastic plates, the light collection of individual PMTs can be improved proportionally to the size of the plate used. This improvement in light collection, in turn, allows for an increase in the overall signal-to-background of the detector, providing information useful for a nuclear nonproliferation agreement or confidence building measure in a shorter amount of time compared to a detector that does not utilize wavelength shifting plates. This increased signal-to-background indicates that, while the inclusion of wavelength-shifting plates in the detector degrades the ability of a post-processing algorithm to reconstruct the position of event vertices in the detector, the overall improvements to the energy resolution of the detector provided by the improved collection of light outweighs this effect.

In this work, the utility of wavelength-shifting plates for improving the performance of a large-scale water-Cherenkov detector has been explored. First, an analytical model of light transport in a wavelength-shifting plate was developed, which indicated that losses due to re-absorption in the plastic and losses at the boundary of the plate were likely to be the main factors driving the light collection behavior of the plates. This analytical model was later found to be in good agreement with Monte Carlo and experimental results. A two-dimensional scan of a single wavelength-shifting plate and PMT pair in a dark box was then performed in order to probe the light collection behavior across the plate's surface. The results of this experiment were then used to develop a Geant4-based Monte Carlo model of the wavelength-shifting plate in the RAT-PAC framework. This Monte Carlo model accurately reproduced the behavior of the wavelength-shifting plate and PMT pair.

The behavior of several wavelength-shifting plates together was then probed using a one-ton water-Cherenkov detector and cosmogenic muons. The number of photoelectrons collected from muons passing through the corner of the detector was recorded for eight PMTs before and after half of them were coupled to wavelength-shifting plates. By comparing the number of photoelectrons collected by those PMTs directly coupled to a wavelength-shifting plate and those PMTs left bare, it was

demonstrated that a large proportion of the light absorbed in the wavelength-shifting plate escapes from the plate itself before striking a different PMT in the detector. The results of this experiment were used to further refine and tune the Monte Carlo model, particularly by refining the behavior of light at the plates' surfaces.

Finally, simulations were performed to model the behavior of wavelength-shifting plates in a large-scale water-Cherenkov detector. A suite of detector signals and backgrounds were simulated for a 16 m by 16 m detector, both with and without wavelength-shifting plates coupled to its PMTs. It was found that the inclusion of wavelength-shifting plates substantially increased the overall light collection of the detector, by approximately 50%, while degrading the ability of an algorithm to successfully reconstruct the location at which an antineutrino interaction occurred in the detector, which caused some signal events to be reconstructed as background events and vice versa. Overall, the inclusion of wavelength-shifting plates in the detector served to increase its signal-to-background by 13.1% and reduce the time it takes to detect the presence of an operating, undeclared nuclear reactor by approximately 25%.

6.1 Applications to Nuclear Nonproliferation

Large-volume water-Cherenkov antineutrino detectors, aided by wavelength-shifting plates, could fulfill an important and novel role in the global nuclear non-proliferation regime. While large-volume antineutrino detectors are likely too novel of a technology and too expensive for the IAEA to implement into any standard safeguards regime, antineutrino detectors may be used to verify compliance with a future bilateral or multilateral nuclear non-proliferation treaty. Such a treaty could, for example, stipulate that one of a State's nuclear reactors, because it poses proliferation risks, must be deactivated, or that the state must not construct any new nuclear reactors which could be used for the production of special nuclear material outside of safeguards. Antineutrino detectors, in this case, could verify the absence of an operating nuclear reactor over some portion of the State's territory to verify compliance with a treaty.

Wavelength-shifting plates could help the antineutrino detector to achieve this goal in three ways. First, wavelength-shifting plates can reduce the cost of constructing the detector in the first place by reducing the number of PMTs required to achieve some desired detector performance. Because wavelength-shifting plastic plates are much cheaper than PMTs, significant cost savings could be possible. To illustrate the potential cost savings, consider PMT optical modules (i.e. PMTs plus supporting electronics) that cost approximately $5,000 per unit and wavelength-shifting plates that cost approximately $400 per unit (though this value would likely be decreased when ordering wavelength-shifting plates in large quantities). The 16 m by 16 m detector considered in Chapter 5 utilizes 1824 PMTs for a total cost of $9.12M. If the number of PMTs can be reduced by 13%, and this reduction compensated for by the inclusion of wavelength-shifting plates (which have been shown to improve

the signal-to-background by 13%), the total cost of the PMTs plus plates would be $8.58M, a cost-savings of approximately half a million dollars, or about 6%. This would further scale with increasing detector size, as the total number of PMTs that can be removed is increased. This reduction in implementation cost would increase the attractiveness of using an antineutrino detector to verify the treaty terms over some other technical means.

Second, wavelength-shifting plates may extend the area over which an antineutrino detector can detect or exclude the existence of an operating nuclear reactor in some specified amount of time. A detector with wavelength-shifting plates, because it has an improved signal-to-background compared to a detector without, is able to detect or exclude the existence of an operating nuclear reactor with fewer antineutrino events occurring in the detector, and thus at a potentially greater range. By the same logic, a detector with wavelength-shifting plates would also be able to detect a nuclear reactor operating at a lower power in the same amount of time compared to a detector without wavelength-shifting plates.

Finally, wavelength-shifting plates may decrease the time an antineutrino detector needs to detect or exclude the existence of a nuclear reactor in some specified range. By the same reasoning as above, the improved signal-to-background of the detector allows for anomalies in the antineutrino rate to be discovered more swiftly, thus allowing for a nuclear reactor to be discovered faster than if wavelength-shifting plates were not utilized in the detector.

Wavelength-shifting plates thus have the capability to make a large-scale water-Cherenkov antineutrino detector more feasibly deployable in a nuclear non-proliferation scenario, or to make such a detector more potent once deployed. Wavelength-shifting plates may thus help to provide the important capability of remote reactor discovery and monitoring to the nuclear non-proliferation regime in order to help detect and deter the illicit generation and diversion of special nuclear material.

6.2 Future Work

The next step to demonstrate the capability of wavelength-shifting plates to aid nuclear non-proliferation goals is to experimentally demonstrate their performance in a large-scale water-Cherenkov antineutrino detector. A future antineutrino detector deployment by the WATCHMAN collaboration would be an ideal candidate. With the potential decommissioning of the Hartlepool Nuclear Power Station, the WATCHMAN collaboration is currently investigating other potential locations where a detector may be deployed in order to demonstrate its ability to monitor an operating nuclear reactor at a distance. Wavelength-shifting plates can be implemented into the detector's construction, and their performance in the detector with respect to the energy resolution and the vertex position reconstruction can be experimentally verified. Alternatively, wavelength-shifting plates could be implemented in a future detector upgrade, and the upgraded detector's performance can be directly compared

to the original detector's performance in order to achieve a more accurate validation of the wavelength-shifting plates' behavior in such a detector.

REFERENCES

[1] Dwight D. Eisenhower. *Atoms for Peace.* Address by Mr. Dwight D. Eisenhower, President of the United States of America, to the 470th Plenary Meeting of the United Nations General Assembly. 1953.

[2] Laurie M Brown. "The idea of the neutrino". In: *Physics today* 31.9 (1978), p. 23.

[3] Jr. Clyde L. Cowan and Frederick Reines. "Detection of the Free Neutrino". In: *Phys. Rev.* 92 (830 1953), pp. 830–831.

[4] Jr. C.L. Cowan et al. "Detection of the Free Neutrino: a Confirmation". In: *Science* 24 (3212 1956), pp. 103–104.

[5] NS Bowden et al. "Experimental results from an antineutrino detector for cooperative monitoring of nuclear reactors". In: *Nuclear Instruments and Methods in Physics Research Section A: Accelerators, Spectrometers, Detectors and Associated Equipment* 572.2 (2007), pp. 985–998.

[6] CHOOZ collaboration et al. "Determination of neutrino incoming direction in the CHOOZ experiment and supernova explosion location by scintillator detectors". In: *Phys. Rev. D* 61 (2000), p. 012001.

[7] F Suekane, KamLAND Collaboration, et al. "KamLAND". In: *Progress in Particle and Nuclear Physics* 57.1 (2006), pp. 106–126.

[8] M Askins et al. "The physics and nuclear nonproliferation goals of watchman: a water cherenkov monitor for antineutrinos". In: *arXiv preprint arXiv:1502.01132* (2015).

[9] F Sutanto et al. "SANDD: A directional antineutrino detector with segmented 6Li-doped pulse-shape-sensitive plastic scintillator". In: *Nuclear Instruments and Methods in Physics Research Section A: Accelerators, Spectrometers, Detectors and Associated Equipment* 1006 (2021), p. 165409.

[10] Yasuhiro Kuroda et al. "A mobile antineutrino detector with plastic scintillators". In: *Nuclear Instruments and Methods in Physics Research Section A:*

Accelerators, Spectrometers, Detectors and Associated Equipment 690 (2012), pp. 41–47.

[11] Ryan Dorrill. "NuLat: A Compact, Segmented, Mobile Anti-neutrino Detector". In: *Journal of Physics: Conference Series*. Vol. 1216. 1. IOP Publishing. 2019, p. 012011.

[12] K Nakamura, ST Petcov, et al. "Neutrino masses, mixing, and oscillations". In: (2018).

[13] Kenneth S Krane. *Introductory nuclear physics*. John Wiley & Sons, 1991.

[14] Alessandro Strumia and Francesco Vissani. "Precise quasielastic neutrino/nucleon cross-section". In: *Physics Letters B* 564.1-2 (2003), pp. 42–54.

[15] P Vogel and John F Beacom. "Angular distribution of neutron inverse beta decay, ν e+ p→ e++ n". In: *Physical Review D* 60.5 (1999), p. 053003.

[16] P Adamson et al. "Measurement of neutrino and antineutrino oscillations using beam and atmospheric data in MINOS". In: *Physical Review Letters* 110.25 (2013), p. 251801.

[17] D Adey et al. "Measurement of the electron antineutrino oscillation with 1958 days of operation at Daya Bay". In: *Physical review letters* 121.24 (2018), p. 241805.

[18] FP An et al. "New measurement of antineutrino oscillation with the full detector configuration at Daya Bay". In: *Physical review letters* 115.11 (2015), p. 111802.

[19] G Bak et al. "Measurement of reactor antineutrino oscillation amplitude and frequency at RENO". In: *Physical Review Letters* 121.20 (2018), p. 201801.

[20] Fengpeng An et al. "Neutrino physics with JUNO". In: *Journal of Physics G: Nuclear and Particle Physics* 43.3 (2016), p. 030401.

[21] Y Abe et al. "Improved measurements of the neutrino mixing angle θ 13 with the Double Chooz detector". In: *Journal of High Energy Physics* 2014.10 (2014), pp. 1–44.

[22] Tzee-Ke Kuo and James Pantaleone. "Neutrino oscillations in matter". In: *Reviews of Modern Physics* 61.4 (1989), p. 937.

[23] M. Bergevin et.al. *Watchmakers (WATer CHerenkov Montecarlo and Analysis Kit for Reactor Sensitivity)*. https://github.com/AIT-WATCHMAN/watchmakers.

[24] Viacheslav A Li et al. "Scalability of gadolinium-doped-water Cherenkov detectors for nuclear nonproliferation". In: *arXiv preprint arXiv:2204.08618* (2022).

[25] M. Yeh et al. "A new water-based liquid scintillator and potential applications". In: *Nuclear Instruments and Methods in Physics Research Section A: Accelerators, Spectrometers, Detectors and Associated Equipment* 660.1 (2011), pp. 51–56. ISSN: 0168-9002. DOI: https://doi.org/10.1016/j.nima.2011.08.040. URL: http://www.sciencedirect.com/science/article/pii/S0168900211016615.

[26] William Johnston and Norm Buchanan. "A Wavelength-shifting Light Collector for the LBNE Far Detector". In: *APS Four Corners Section Meeting Abstracts*. 2011, pp. D5–004.

[27] R Becker-Szendy et al. "IMB-3: A Large water Cherenkov detector for nucleon decay and neutrino interactions". In: *Nuclear Instruments and Methods in Physics Research Section A: Accelerators, Spectrometers, Detectors and Associated Equipment* 324.1-2 (1993), pp. 363–382.

[28] R. Claus et al. "A waveshifter light collector for a water Cherenkov detector". In: *Nuclear Instruments and Methods in Physics Research Section A: Accelerators, Spectrometers, Detectors and Associated Equipment* 261.3 (1987), pp. 540–542. ISSN: 0168-9002. DOI: https://doi.org/10.1016/0168-9002(87)90366-4. URL: http://www.sciencedirect.com/science/article/pii/0168900287903664.

[29] FT Avignone III. "V- A Elastic Scattering of Electrons by Fission Antineutrinos". In: *Physical Review D* 2.11 (1970), p. 2609.

[30] Minfang Yeh, A Garnov, and Richard L Hahn. "Gadolinium-loaded liquid scintillator for high-precision measurements of antineutrino oscillations and the mixing angle, $\theta 13$". In: *Nuclear Instruments and Methods in Physics Research Section A: Accelerators, Spectrometers, Detectors and Associated Equipment* 578.1 (2007), pp. 329–339.

[31] The International Atomic Energy Agency. "Amid Global Crises, Nuclear Power Provides Energy Security with Increased Electricity Generation in 2021". In: (2022). URL: https://www.iaea.org/newscenter/news/amid-global-crises-nuclear-power-provides-energy-security-with-increased-electricity-generation-in-2021.

[32] K Abe et al. "Search for differences in oscillation parameters for atmospheric neutrinos and antineutrinos at Super-Kamiokande". In: *Physical Review Letters* 107.24 (2011), p. 241801.

[33] IE Tamm and IM Frank. "Coherent radiation of fast electrons in a medium". In: *Dokl. Akad. Nauk SSSR*. Vol. 14. 3. 1937, pp. 107–112.

[34] National Institute of Standards and Technology. *EStar: Stopping Power and Range Tables for Electrons*. data retrieved from EStar, https://physics.nist.gov/cgi-bin/Star/e_table.pl. 1995.

[35] Eljen Technology. *GENERAL PURPOSE EJ-200, EJ-204, EJ-208, EJ-212*. URL: https://eljentechnology.com/products/plastic-scintillators/ej-200-ej-204-ej-208-ej-212.

[36] Glenn F. Knoll. *Radiation Detection and Measurement*. John Wiley & Sons, Inc., 2000.

[37] Takako Kogure et al. "Fluorescence imaging using a fluorescent protein with a large Stokes shift". In: *Methods* 45.3 (2008), pp. 223–226.

[38] Hamamatsu. "Photomultiplier Tubes: Basics and Applications". In: (2007).

[39] *Treaty on the Non-Proliferation of Nuclear Weapons*. U.N.T.S I-10485, Signed July 1st, 1968.

[40] Daryl Kimball and Shannon Bugos. *Timeline of the Nuclear Nonproliferation Treaty (NPT)*. Arms Control Association, 2022.

[41] David Fischer. *HISTORY OF THE INTERNATIONAL ATOMIC ENERGY AGENCY: The First Forty Years*. International Atomic Energy Agency, 1997.

[42] *Nuclear Material Accounting Handbook*. International Atomic Energy Agency, 2008.

[43] *Surveillance and Containment Measures to Support IAEA Safeguards*. International Atomic Energy Agency, 1977.

[44] Patrick R.V. Horton and Ivan G. Waddoups. *Tamper-Indicating Devices and Safeguards Seals Evaluation Test Report*. Sandia National Laboratories, 1993.

[45] *Model Protocol Additional to the Agreement(s) Between State(s) and the International Atomic Energy Agency for the Application of Safeguards*. International Atomic Energy Agency, 1997.

[46] Jacques Baute. *Timeline IRAQ: Challenges & Lessons Learned from Nuclear Inspections*. International Atomic Energy Agency, 2004.

[47] *Agreed Framework between the United States of America and the Democratic People's Republic of Korea*. International Atomic Energy Agency INFCIRC/457, 21 October 1994.

[48] *Joint Comprehensive Plan of Action*. U.S. Department of State, 14 July 2015.

[49] Adam Bernstein et al. "Colloquium : Neutrino detectors as tools for nuclear security". In: *Reviews of Modern Physics* 92.1 (Mar. 2020). ISSN: 1539-0756. DOI: 10.1103/revmodphys.92.011003. URL: http://dx.doi.org/10.1103/RevModPhys.92.011003.

[50] Adam Bernstein et al. "Nuclear reactor safeguards and monitoring with antineutrino detectors". In: *Journal of Applied Physics* 91.7 (2002), pp. 4672–4676.

[51] Viacheslav A Li. "Far-Field Monitoring of Reactor Antineutrinos for Nonproliferation". In: *arXiv preprint arXiv:1907.08891* (2019).

[52] James Macintosh. "Confidence building in the arms control process: A transformation view". In: (1996).

[53] Igor Moric. "How commercial satellite imagery could soon make nuclear secrecy very difficult—if not impossible". In: (2022).

[54] *Environmental Monitoring for Nuclear Safeguards*. OTA-BP-ISS-168. U.S. Congress, Office of Technology Assessment, 1995.

[55] D-M Mei and A Hime. "Muon-induced background study for underground laboratories". In: *Physical Review D* 73.5 (2006), p. 053004.

[56] Tanner Kaptanoglu et al. "Spectral photon sorting for large-scale Cherenkov and scintillation detectors". In: *Physical Review D* 101.7 (2020), p. 072002.

[57] NO Myers. "Characterization of surface roughness". In: *Wear* 5.3 (1962), pp. 182–189.

[58] Eljen Technology. *WAVELENGTH SHIFTING PLASTICS*. URL: https://eljentechnology.com/products/wavelength-shifting-plastics/ej-280-ej-282-ej-284-ej-286.

[59] A Bernstein. *AIT-WATCHMAN Conceptual Design Review Report*. Tech. rep. Lawrence Livermore National Lab.(LLNL), Livermore, CA (United States), 2019.

[60] M. Bergevin et.al. *RAT-PAC: Reactor Analysis Tool Plus Additional Codes*. https://github.com/AIT-WATCHMAN/rat-pac.

[61] Sea Agostinelli et al. "GEANT4—a simulation toolkit". In: *Nuclear instruments and methods in physics research section A: Accelerators, Spectrometers, Detectors and Associated Equipment* 506.3 (2003), pp. 250–303.

[62] Rene Brun and Fons Rademakers. "ROOT—an object oriented data analysis framework". In: *Nuclear Instruments and Methods in Physics Research Section*

A: Accelerators, Spectrometers, Detectors and Associated Equipment 389.1-2 (1997), pp. 81–86.

[63] Chuck Hurlbut. *EJ286 Emiss and Lin Attn Coeff, and Refr.Index vs wavelength.* Personal communication. Dec. 18, 2019.

[64] Austin Mullen et al. "Improvement in light collection of a photomultiplier tube using a wavelength-shifting plate". In: *Nuclear Instruments and Methods in Physics Research Section A: Accelerators, Spectrometers, Detectors and Associated Equipment* 1040 (2022), p. 167207. ISSN: 0168-9002. DOI: https://doi.org/10.1016/j.nima.2022.167207. URL: https://www.sciencedirect.com/science/article/pii/S0168900222005642.

[65] Hamamatsu Photonics. *Large Photocathode Area Photomultiplier Tubes*. Tech. rep. 2019.

[66] Eljen Technology. *SILICONE GREASE*. URL: https://eljentechnology.com/products/accessories/ej-550-ej-552.

[67] William A. Johnston. "Design, Simulation, and Prototyping of Wavelength-Shifting Plate Light Collector For A Large Water Cherenkov Detector". PhD thesis. 2014.

[68] Alexandra Asghari. *The water neutron detector (WaND)*. University of California, Berkeley, 2016.

[69] DuPont. *Tyvek*. URL: https://www.dupont.com/brands/tyvek.html.

[70] Peter Gumplinger and John Apostolakis. "Optical Photon Processes in GEANT4". Users' Workshop at CERN. 2002. URL: https://geant4.web.cern.ch/sites/default/files/geant4/collaboration/workshops/users2002/talks/lectures/OpticalPhoton.pdf.

[71] A.M. Barna and S.T. Dye. *Web Application for Modeling Global Antineutrinos*. 2015. URL: arXiv:1510.05633.

[72] Michael Smy. "Low Energy Event Reconstruction and Selection in Super-Kamiokande-III". In: *International Cosmic Ray Conference*. Vol. 5. 2008, pp. 1279–1282.